TECHNISCHE UNIVERSITÄT WIEN

DIPLOMARBEIT

Spectral Correction for a Rhodium-Anode Transmission X-Ray Tube

Quantitative X-Ray Fluorescence Analysis and Comparison with a Side-Window Rhodium-Anode Tube

zur Erlangung des akademischen Grades
Diplomingenieurin

im Rahmen des Studiums
Technische Physik

eingereicht von
Mag. phil. Elisabeth Holub, BSc.
Matrikelnummer 00007396

ausgeführt am Atominstitut
der Fakultät für Physik der Technischen Universität Wien

Betreuung
Betreuer: Ao.Univ.Prof. Dipl.-Ing. Dr.techn. Peter Wobrauschek
Mitwirkung: Ao.Univ.Prof. Dipl.-Ing. Dr.techn. Christina Streli

Wien, 11.02.2020 (Unterschrift Verfasserin) (Unterschrift Betreuer)

Acknowledgements

First, I would like to thank my supervisor Peter Wobrauschek for his patience, for always having a sympathetic ear and for keeping my spirits high. Never have I seen a professor take so much time to help his students and listen to their ideas.

Second, this thesis would not have come to life without the persistence of Ekrem, my life partner, who encouraged me to study physics in the first place and without whom I would have given up midway. I am deeply thankful for his loving support during all my years of study and for listening to my dilettante explanations of quantum physics.

Last, I would like to dedicate this thesis to my mother and father, Gabriela and Hugo Holub, who have always been there for me. There are no words that can express my deep gratitude to them. I owe them everything.

Abstract

Energy-dispersive X-ray fluorescence analysis (EDXRF) is a fast, non-destructive technique for elemental analysis that relies on semiconductor detectors and X-ray tubes. While side-window tubes have been extensively studied for their application in EDXRF, research and literature on transmission tubes are rather scarce. Therefore, the present thesis provides important insights into the characteristics of transmission tubes.

The following research objectives were addressed: to analyze possible reasons for the incorrect calculation of elemental concentrations measured with a rhodium-anode transmission tube; to find a corrective function to better reflect the spectral distribution of the transmission tube; to test the corrected spectrum by means of reference standard materials; to extend the experimental setup in such a way as to correctly quantify light elements; and to compare two software packages for data evaluation.

By modifying the test setup and the calculated spectral distribution, the range of quantifiable elements was successfully extended to include light elements. The corrected transmission-tube spectrum provides excellent quantitative results, achieving an even better performance than a well-established side-window spectrometer.

Zusammenfassung

Die energiedispersive Röntgenfluoreszenzanalyse (EDXRF) ist ein schnelles, materialschonendes Verfahren zur Elementanalyse, das auf Halbleiterdetektoren und Röntgenröhren beruht. Während Seitenfensterröhren hinsichtlich ihrer Anwendung bei der EDXRF ausführlich untersucht wurden, sind Forschung und Literatur über Transmissionsröhren eher spärlich gesät. Daher gibt die vorliegende Arbeit wichtige Einblicke in die Charakteristika von Transmissionsröhren.

Folgende Forschungsziele wurden verfolgt: Analyse möglicher Ursachen für die fehlerhafte Berechnung von mittels einer Rhodiumanoden-Transmissionsröhre gemessenen Elementkonzentrationen; Bestimmung einer Korrekturfunktion, welche die Spektralverteilung der Transmissionsröhre besser widerspiegelt; Überprüfung des korrigierten Spektrums anhand von Referenzstandards; Erweiterung des experimentellen Aufbaus zur korrekten Quantifizierung leichter Elemente; und Vergleich zweier Softwarepakete zur Datenanalyse.

Durch eine Modifikation des Versuchsaufbaus und der berechneten Spektralverteilung wurde der Umfang der quantifizierbaren Elemente erfolgreich auf leichte Elemente erweitert. Das korrigierte Transmissionsröhrenspektrum liefert ausgezeichnete quantitative Resultate, die sogar die Ergebnisse eines bewährten Seitenfensterspektrometers übertreffen.

Contents

1 Introduction

X-ray fluorescence analysis (XRF) is a well-established technique for qualitative and quantitative elemental analysis. A sample of unknown composition is irradiated with X-rays to excite the sample atoms, which then emit characteristic radiation specific for the excited element (see Section 2). By collecting and counting the radiation for several energy levels or wavelengths, one can obtain the intensity of the emitted radiation. Peaks in this energy spectrum identify the elements contained in the sample under investigation, while the intensity of these peaks is proportional to the concentration of the corresponding element. (cf. [34], [20])

Basically, there are two methods of measuring X-ray fluorescence. In energy-dispersive X-ray fluorescence (EDXRF), semiconductor detectors are used to determine the energy levels of the emitted radiation and group them into bins or channels. In wavelength-dispersive X-ray fluorescence (WDXRF), the resulting fluorescence is analyzed with regard to the wavelength using a single crystal, which diffracts different wavelengths in different directions. In contrast to WDXRF, EDXRF is less accurate due to poor detector resolution, but it is also faster and does not require extensive sample preparation. EDXRF is therefore widely used in non-destructive testing and analysis. (cf. [22], [9])

Quantification in EDXRF is, however, not trivial. In thick samples, the primary fluorescence may again be absorbed within the sample and cause secondary or even tertiary fluorescence processes, making direct conclusions about sample concentrations impossible. Quantification is particularly tricky when the sample contains low-Z elements, whose fluorescence lines cannot be measured. This is due to the Auger process (see Section 2), which, at low excitation energies, is dominant over fluorescence and leads to poor signal intensity in the low-energy range.

At the same time, light elements may cause non-negligible absorption that needs to be corrected for (cf. [22], [8]). Apart from deviations caused by these so-called *matrix effects*, the theoretical models themselves are inaccurate in so far as they are usually valid for specific anode thicknesses only (cf. [19], [36]).

Another issue is the dependence of the excitation spectrum on the geometry of the X-ray tube and on the excitation voltage. Increasing voltage will cause the maximum of the continuous excitation spectrum to shift to the right, while anode self-absorption (and so the anode self-absorption edge) will increase. It has also been demonstrated that the characteristic lines of different anode materials behave differently with increasing excitation voltage. (cf. [8])

In addition, the excitation energy of laboratory X-ray sources is limited and therefore not strong enough to excite the K fluorescence lines of heavy elements like tungsten and lead. For this reason, one has to resort to the analysis of L lines of these elements, which lie in the low-energy region of the spectrum. Unfortunately, the K lines of many transitional metals also occur in this spectral region, and the spacing between the K lines of transitional metals and the L lines of heavy elements may be very narrow, thus exacerbating the problem of differentiation between and quantification of these elements. (cf. [16])

This situation is aggravated by the fact that the semiconductor detectors used in energy quantification only have a moderate resolution, which is generally in the range of 150-200 eV. Fluorescence lines that have similar energies may hence not be separated and misinterpreted as one single peak. Moreover, unwanted detector artifacts (escape peaks, sum peaks, see Section 2) will overlap with the fluorescence lines and therefore hamper quantification. (cf. [16], [20], [8])

Correction for the above-mentioned phenomena is usually achieved either by comparison of the radiation emitted by a specific sample to a set of standards with known composition or the use of fundamental parameter models (cf. [44], see Section 6). Given that empirical measurement strongly depends on environmental conditions and empirical results are inherently uncertain, it is desirable to obtain the spectrum solely from calculation, even more so when analyzing complex samples using varying geometries and settings. On the other hand, fundamental parameter models can never be exhaustive and require extensive calibration and computational effort.

The aim of this thesis is to refine an existing fundamental parameter software package and adjust it in such a way as to correctly predict quantitative values upon excitation of a specimen with a rhodium-anode transmission tube. While thick-anode tubes have been extensively described for use in EDXRF, literature on transmission tubes utilized for elemental quantification is rather sparse. One therefore has to resort to experimental approaches to test and improve the applicability of these tubes.

The structure of this thesis is as follows: The next Section, Section 2, introduces the Bohr model, which is the fundamental model used to describe atoms and electron energy states. The nomenclature used in X-ray fluorescence analysis is presented in Section 3. Section 4 illustrates the interaction processes relevant for the generation of X-rays and X-ray analysis. Drawing on the information provided in the previous sections, Section 5 outlines the origin and features of X-ray tube spectra as well as the influence of detector artifacts. Section 6 explains the fundamental parameters approach, while Section 7 summarizes the principles of micro X-ray fluorescence analysis (μXRF).

Sections 8 and 9 present the three setups employed to validate the theoretical results of this thesis: one confocal setup and two wide-field setups. Section 10 then gives an overview of the software used for simulation and data analysis, whereas Sections 11, 12 and 13 illustrate the results of the measurement and simulation of the tube spectrum.

The fitting process applied to correct the tube spectrum is explained in Section 14. The sample measurements carried out to verify that the corrective function renders accurate quantitative results are described in Section 15. Sections 16 and 17 provide a comparative evaluation of another rhodium-tube setup to verify the calculated concentrations. Last, Section 18 summarizes the conclusions of this thesis based on the quantitative results obtained and suggests directions for further research.

2 The Bohr Model

Although atoms and their constituents cannot be fully described by the Bohr model, it will be sufficient to understand the underlying processes of X-ray generation and absorption. The following derivation follows [13] very closely but is by no means exhaustive.

In an atom with only one electron, the electron will move around the common center of mass S of the electron and the nucleus. The electron's orbit is circular and can be characterized by the radius r. One can describe this motion by a single particle with mass μ that revolves around the center of the nucleus and has the energy $\frac{\mu v^2}{2}$. If one assumes that the orbit is stable, the centripetal force and the Coulomb force must cancel each other out, i.e.

$$\frac{\mu v^2}{r} \cdot e_r = \frac{1}{4\pi\epsilon_0} \cdot \frac{Ze^2}{r^2} \cdot e_r \tag{1}$$

where v is the velocity of the particle;
$Z \cdot e$ is the charge of the nucleus;
ϵ_0 is the dielectric constant and
e_r is the unit vector in radial direction.

When we describe the electron as a standing wave with wavelength λ, the number of wavelengths that fits into such an orbit with circumference $2\pi r$ must be a whole number:

$$2\pi r = n \cdot \lambda \tag{2}$$

with n = 1,2,3,...

Since material waves can be expressed by $\lambda = \frac{h}{\mu v}$, the velocity of the electron can be expressed as

$$v = n \cdot \frac{h}{2\pi\mu r}. \tag{3}$$

If one rearranges Equation (1) and replaces v with the velocity given in Equation (3), one obtains the orbits in which the electron moves:

$$r = \frac{n^2 h^2 \epsilon_0}{\pi\mu Z e^2}. \tag{4}$$

In a nutshell, the radius of the electron's orbital or *shell* is quantized and can take only specific values characterized by the quantum number n.

In fact, the energy state of every electron is characterized by several quantum numbers that are beyond the description by the Bohr model. For the purpose of illustration, one can imagine a shell as being organized into subshells that represent slightly different energy levels.

In X-ray analysis, capital letters are used to represent the orbitals according to their main quantum number. For n=1, the electrons are in the K shell, which is closest to the nucleus, while the second shell is called the L shell, the third shell is the M shell and so on.

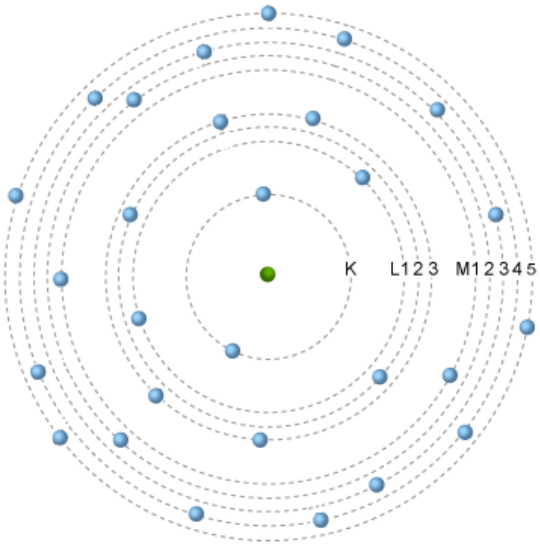

Figure 1: Atomic shells. Source: [38]

3 Nomenclature

Two naming conventions are used in X-ray spectroscopy: the *Siegbahn notation* and the *IUPAC notation*. As the energy of an X-ray depends on the specific transition of an electron from one shell to another, both systems use these electron transitions to characterize the resulting X-rays.

3.1 The Siegbahn Notation

In Siegbahn's notation, only the target shell is relevant for the identification of a transition. X-rays originating from a transition to the K shell are named K lines, while transitions to the L shell are named L lines. When the electron has jumped from the nearest shell, the corresponding X-rays form the Kα line; when the electron's origin is the second nearest shell, the resulting X-ray line is the Kβ line and so on. (cf. [45])

The subshells may contain several electrons, each of which produces a slightly different X-ray energy upon transitioning. Therefore, the exact transition is identified by adding a number, for example Kα_1, where 1 denotes the highest energy, 2 is the second highest energy and so on. (cf. [45])

3.2 The IUPAC Notation

In the IUPAC (International Union of Pure and Applied Chemistry) notation, both the shell of origin and the target shell are required to specify the electron transition ("two-electron description"). The first letter and number describe the target state, while the second letter and number refer to the the electron state of origin (cf. [29]). As an example, Siegbahn's Kα_1 transition would correspond to the KL3 IUPAC transition.

4 Interactions of Electrons and Photons with Matter

It is patently obvious that the elemental characterization of a specimen by characteristic X-rays is possible only if one knows the physical processes occurring within the sample upon impingement of the X-ray beam. However, it is not only the sample interactions that influence the measured signal. The measured intensity distribution strongly depends on the initial tube spectrum with which the sample is irradiated, which is why it is crucial to understand how electrons interact with the anode target to create the tube spectrum in the first place.

While electrons interact with the sample via the strong Coulomb (i.e. electrical) force, photons like X-rays may travel much longer distances in matter before they undergo an interaction because they are uncharged (cf. [12]). The two main types of interaction between X-rays and a sample are scattering and photoelectric absorption, with absorption being the dominant process (cf. [27]), whereas the most important processes triggered by electrons are bremsstrahlung, Auger electron and X-ray emission.

4.1 Interactions of Photons with Matter

4.2 Compton Scattering

When a photon undergoes inelastic or *Compton scattering* (see Figure 2), it transfers part of its energy to an outer shell electron of a sample atom and experiences a change in momentum. The angle by which the photon is deflected is proportional to its energy loss. (cf. [41], [43], [25])

The energy of the scattered photon E_{sc} (in MeV) can be derived from the laws of energy and momentum conservation (cf. [10]):

$$E_{sc} = E_0/[1 + (E_0/0.511)(1 - cos\theta)], \tag{5}$$

where E_0 is the energy in MeV of the incident photon and
θ is the scattering angle.

If the energy transferred to the electron is high enough, it may leave the atom. The energy of this *recoil electron* is then

$$E_{re} = E_0 - E_{sc}. \tag{6}$$

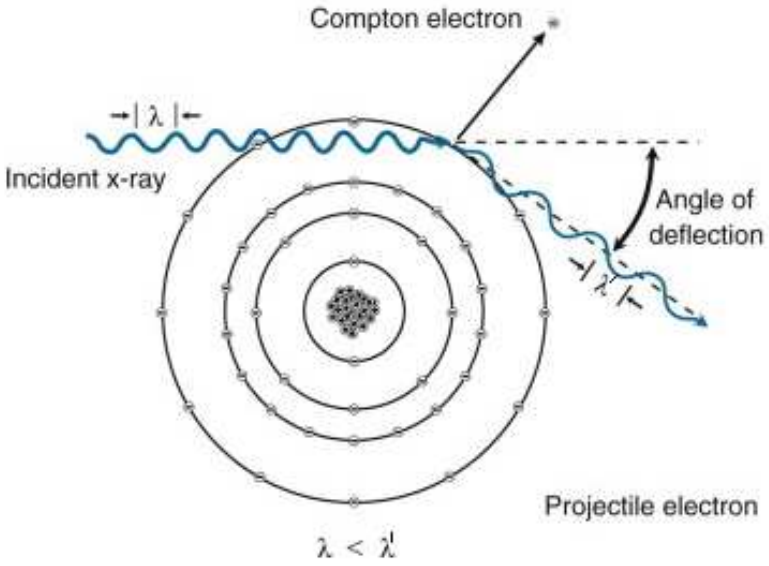

Figure 2: Compton effect. Source: [43]

The scattering process causes a change in the wavelength of the X-ray, which is outlined in Figure 2, where λ denotes the incident wave and λ' the scattered wave.

4.3 Photoelectric Effect

When an atom absorbs a high-energy photon, an electron from an inner shell (a so-called *photoelectron*) is discharged. In order for a photoelectron to be ejected, the photon's energy must be above the K absorption edge of the element. The photoelectron's energy is described by Equation (7).

$$E_{el} = h \cdot \nu - E_{bind}, \tag{7}$$

where $h \cdot \nu$ is the energy of the incident photon and
E_{bind} is the binding energy.

The atom is now in an excited, unstable state. To reach a stable state, the vacancy in the inner shell is filled by another electron from a higher shell. In turn, this process leaves an electron hole in the higher shell, which is again occupied by an electron from an even higher shell and so on. The excess energy of every electron engaging in this process is emitted in the form of a photon (i.e. an X-ray), leading to a cascade of X-rays. Precisely, the emitted excess energy is the difference between the energy shell the electron originates from and the vacant energy shell.

Accordingly, the energy of such an X-ray can be described as follows (cf. [36], [39]):

$$h\nu = E_2 - E_1, \tag{8}$$

where h is Planck's constant,
ν is the frequency of the emitted X-ray and
E_1 and E_2 are the energies of the involved shells.

As energy shells and the corresponding energy states are unique for every element, the energy and thus the frequency of the emitted X-rays solely depend on the material from which they are emitted. For this reason, they are called *characteristic X-rays*. (cf. [64], [12])

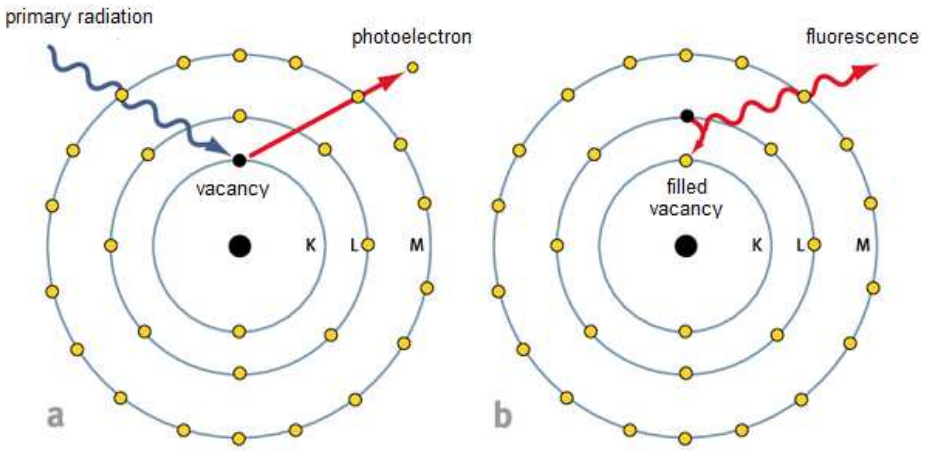

Figure 3: Photoelectric effect and x-ray fluorescence. Source: [1]

4.4 Pair Production

This interaction is not relevant for X-ray fluorescence and is mentioned merely for the sake of completeness. Photons may interact with the strong field of the nucleus of an atom, whereby the photon is converted into a pair of charged particles, an electron and a positron. The photon's energy must therefore be higher than the sum of the rest energies of the positron and the electron, i.e. higher than 1.022 MeV.

At this energy level, photons do not induce any noticeable fluorescence, as the photoelectric cross-section is highest just above the binding energy of the interacting electron and decreases with energy, while pair-production probability increases with the energy of the incident photon. (cf. [12])

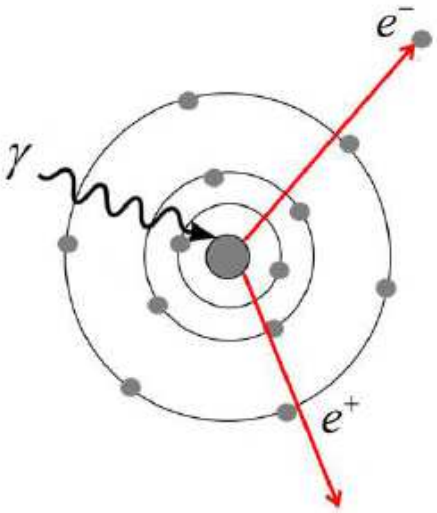

Figure 4: Pair production. Source: [59]

4.5 Auger Effect

As described in Section 4.3, the atom is in an excited energy state when it absorbs a high-energy photon and has to lose excess energy to reestablish a stable state. To this end, an electron may be emitted instead of X-ray fluorescence, i.e. X-ray photons.

This non-radiative process, the so-called *Auger effect*, competes with fluorescence and thus diminishes the fluorescence yield and signal intensity. The Auger effect is the dominant process for low-Z elements and the main reason why these elements cannot be analyzed by X-ray spectrometry. (cf. [20], [36], [1])

Figure 4 describes the yields of X-ray fluorescence and Auger electrons depending on the atomic number of the sample element, thereby illustrating the problem of low-Z element analysis.

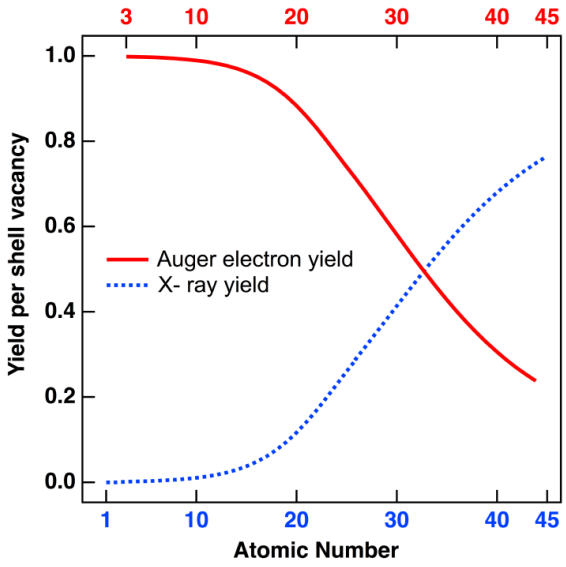

Figure 5: Fluorescence and Auger electron yield. Source: [62]

4.6 Interactions of Electrons with Matter

The most relevant electron-sample interaction processes for X-ray tubes are the excitement of atoms and the subsequent emission of characteristic X-rays or Auger electrons, backscattering and the emission of bremsstrahlung.

The volume in which these interactions take place depends on the energy of the incident beam, the atomic weight of the sample and the angle at which the beam hits the sample. Each process occurs within a certain sample depth, which is illustrated in Figure 6. (cf. [24])

In thick samples (or in our case, thick targets), high-energy electrons will emit bremsstrahlung and generate fluorescence in deep layers of the sample. Since this radiation is subject to absorption by the above layers, low-energy radiation cannot escape and reach the detector. Thin samples, on the other hand, will generate a smaller amount of fluorescence due to the smaller ionization volume, but a larger amount of bremsstrahlung, as absorption is much weaker. Sample thickness may therefore influence the shape and intensity of the resulting X-ray signal.

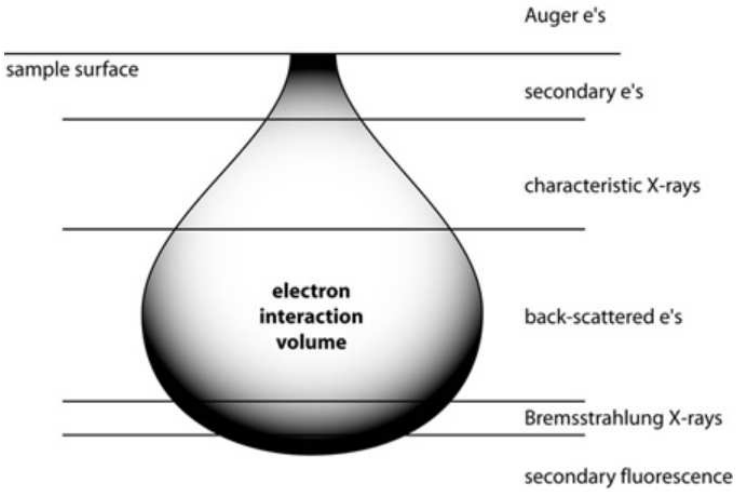

Figure 6: Electron-sample interaction volume. Source: [24]

4.6.1 Electron Backscattering

If an electron undergoes interaction with the nucleus of an atom, *elastic scattering* may take place. The electron does not lose energy in this process but is backscattered. (cf. [64])

4.6.2 Emission of Characteristic Radiation

When high-energy particles are *inelastically scattered* by an atom, they transfer some or all kinetic energy to the atom, thereby enabling electrons from inner shells to escape. Like in the photoelectric effect, electrons from higher shells (i.e. energy states) will fill the vacancies and get rid of excess energy by emitting characteristic X-rays. (cf. [64])

4.6.3 Auger Electrons

As established above, for an atom to go from an excited state back to the ground state, it has to lose energy. Instead of producing characteristic X-rays, an atom may also emit so-called *Auger electrons*. Since the energy of Auger electrons is merely a few keV, they are easily absorbed and escape the sample from the surface only. (cf. [64], [32])

4.6.4 Emission of Bremsstrahlung

This type of radiation is emitted by impinging high-energy electrons, which are slowed down in the Coulomb fields of the nuclei of the target material. According to the theory of electromagnetism, the deceleration of charged particles goes hand in hand with the

emission of radiation. As the attraction of the nucleus depends on the atomic number Z, the radiated energy is Z-dependent. Since the particles can lose various portions of their kinetic energy, which is then emitted in the form of X-rays, the distribution of this radiation is continuous. (cf. [36], [64], [24])

5 X-Ray Tube Spectra

5.1 Relation Between Energy, Frequency and Wavelength

As mentioned in the previous section, X-rays and electromagnetic waves in general can be distinguished by either their energy or their wavelength. These terms can be used almost interchangeably because they are connected by the following relation (cf. [17]):

$$E = h \cdot \nu = \frac{h \cdot c}{\lambda}, \tag{9}$$

where E is the X-ray energy,
ν is the X-ray frequency,
λ is the X-ray wavelength and
c is the velocity of light.

5.2 Intensity and Spectral Distribution

The intensity of an X-ray beam is defined as the total energy $dN \cdot E$ transmitted per unit time dt and unit area A:

$$I(E) = \frac{dN \cdot E}{A \cdot dt}. \tag{10}$$

The spectral distribution $I^*(E)$ is the distribution of the specific intensity, i.e. the intensity within a small energy range dE:

$$I^*(E) = dI(E)/dE \tag{11}$$

The area underneath this distribution is equal the total intensity I. (cf.[31])

5.3 Functioning Principle of an X-Ray Tube

X-ray tubes are evacuated glass containers including a cathode and an anode made of a material with a high atomic number. The cathode is heated to emit electrons, which are accelerated in a strong electric field until they hit the anode. The number of emitted electrons is proportional to the current at the cathode, while the potential difference and

thus the electric field between the cathode and the anode controls the energy of the electrons. (cf. [11])

The bombardment of a target material with electrons generates a considerable amount of *bremsstrahlung* of varying energy, with the maximum energy of the generated X-rays depending on the tube voltage. The relation between radiation output and tube voltage is, however, not linear, but proportional to U^2. (cf. [11])

Beside the bremsstrahlung emitted by the incoming electrons, the anode atoms emit characteristic X-rays of specific energies (see Section 4). The spectrum of X-rays leaving the tube is therefore composed of both characteristic and background radiation (i.e. bremsstrahlung), with the characteristic X-rays being superimposed on the continuous background. The characteristic emission lines of rhodium, the anode material of the test tube, are listed in Table 1 (cf. [60]).

Line	Energy [keV]
Kα_1	20.216
Kα_2	20.074
Kβ_1	20.724
Lα_1	2.697
Lα_2	2.692
Lβ_1	2.834
Lβ_2	3.001
Lγ_1	3.144

Table 1: Emission lines of rhodium

This primary spectrum is influenced by filters, collimators and the tube window, which is the thin plate or film through which the emitted X-rays leave the tube in a certain direction and at a certain angle (see Section 5.8).

In general, X-ray tubes are highly inefficient because most of the power is lost at the anode and converted to heat. This loss is due to the excitation of material waves, so-called phonons, in the lattice structure of the anode material. Less than 1 % of the electric energy used to operate the tube is converted into X-rays. (cf. [31])

5.4 Duane-Hunt Law

The Duane-Hunt law gives the minimum X-ray wavelength λ_{min} that can be excited by a given tube voltage V (cf. [36], [20]):

$$\lambda_{min} = \frac{h \cdot c}{e \cdot V}, \tag{12}$$

where λ(nm) = 1.239/E(keV),
h is Planck's constant,
e is the electron charge and
c is the velocity of light.

Since wavelength and energy are inversely proportional (see Equation 9), the minimum wavelength corresponds to the maximum energy of fluorescence radiation.

5.5 Beer-Lambert Law

The Beer-Lambert law describes the attenuation of X-ray beams in a material of a certain mass density and atomic number. Such attenuation occurs not only within the sample, but also within the anode, the window and possible air paths between the window and the sample or between the sample and the detector. The intensity of the beam at a depth x can be described as follows (cf. [14]):

$$I = I_0 \cdot exp(-\mu(\lambda_0, Z) \cdot \rho \cdot x \cdot csc(\alpha)), \tag{13}$$

where I_0 is the initial X-ray intensity,
$\mu(\lambda_0)$ is the mass attenuation coefficient for photons with wavelength λ_0 in a material of atomic number Z,
ρ is the mass density of the specimen and
α is the incidence angle.

One has to bear in mind that this law is based on several limiting assumptions: the beam should be parallel, and the specimen is assumed to be infinite in all three dimensions and of uniform composition.

As the mass attenuation coefficient depends on the atomic number, with attenuation increasing for higher atomic numbers, the intensity distribution allows us to identify the elements within a sample. (cf. [27], [56], [25])

The mass attenuation coefficient μ decreases strongly with increasing energy E (cf. [21]):

$$\mu \propto E^{-3}. \tag{14}$$

It rises sharply when a new atomic shell can be excited, but then drops again quickly. For this reason, the most efficient excitation region lies just above the absorption edge of the element in question.

5.6 Kramers' Law

Kramers was the first to describe the bremsstrahlung spectrum of thick-target tubes in his seminal thesis (cf. [5], p. 125). He found that

$$N(E) \propto Z \cdot (E_{max} - E) = Z \cdot E \cdot (\frac{E_{max}}{E} - 1), \tag{15}$$

where $N(E)$ is the number of counts,
E_{max} is the maximum photon energy and
Z is the atomic number of the target.

Kramer's Law does not include self-absorption within the anode or other factors like the window and possible electron backscatter. It therefore provides only a very rough estimate of the radiation reaching the sample. Yet, it is useful to get a general idea of the spectrum.

5.7 X-ray Generation in Thin and Thick Anodes

5.7.1 Thin Anodes

The spectrum differs for thin and thick anodes. For very thin anodes, every impinging electron is deflected only once by an anode atom, thereby emitting radiation. As these deflections are of a statistical nature, a continuum of energies up to a maximum energy will be created, with the maximum energy being equal to the kinetic energy of the electron. (cf. [31])

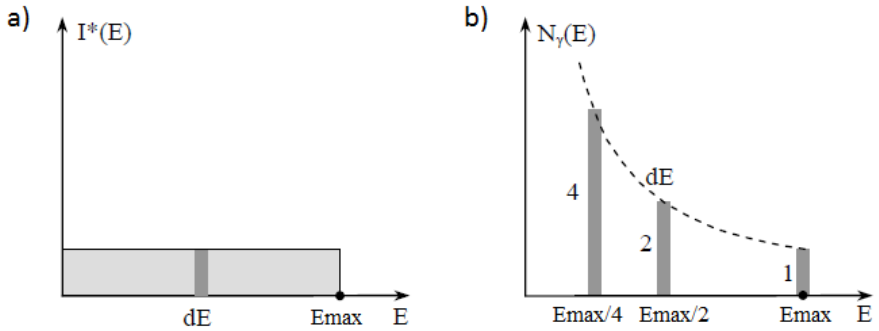

Figure 7: a) distribution of bremsstrahlung; b) photon number. Adapted from [31]

For thin anodes, the product of the number of photons produced (N_γ) and the energy of these photons (E_γ) is constant, i.e.

$$E_\gamma \cdot N_\gamma = const \tag{16}$$

This means that the number of photons of a certain energy decreases with increasing energy and that the spectral distribution is a rectangular function (see Figure 7).

As the maximum photon energy E_{max} decreases with decreasing tube voltage but the height of the distribution remains unchanged, the total intensity (i.e. the area underneath the distribution) is proportional to the maximum photon energy.

Conversely, according to Equation 16, the number of photons generated at a certain electron energy E increases with decreasing photon energy (and hence with decreasing energy loss by the electron). The explanation for this is that it is very unlikely for an electron to "hit" or get very near an atom and lose all its energy, so the number of interactions will be higher for lower energies. It is far more likely for an electron to be deflected and lose only a small fraction of its energy. (cf. [31], [64])

Matrix effects can be neglected for thin samples, and radiation intensity and mass per unit area are proportional. (cf. [56])

5.7.2 Thick Anodes

Thick anodes can be modeled as a series of thin anode layers. However, the energy of the electrons decreases with each layer, with energy loss increasing with increasing depth. One can calculate variable layer thicknesses dx so that the electrons lose the same amount of energy dE each layer. Then, the intensity for every layer depends on the corresponding maximum photon energy E_{max} for each layer, and total intensity is proportional to E_{max}^2.

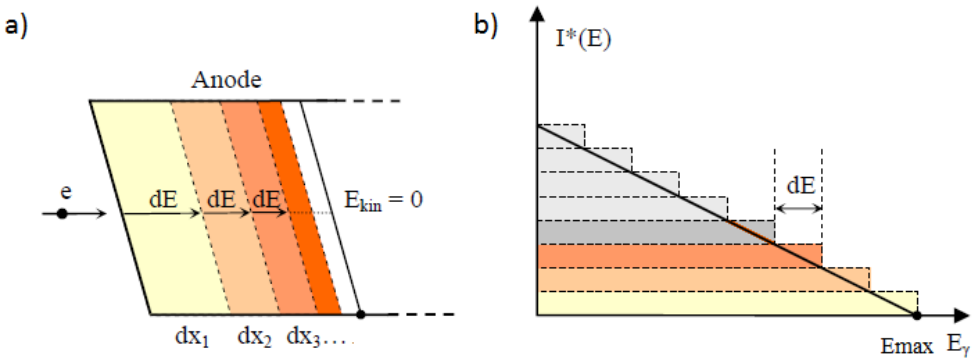

Figure 8: a) electron energy loss b) distribution of bremsstrahlung. Adapted from [31]

In thick samples, matrix effects cannot be neglected and will influence the signal. This said, mathematical description is simplified by the fact that the characteristic radiation intensity does not depend on actual sample thickness. (cf. [56]).

5.8 Tube Window and Air Paths

The window serves as a shield for the tube components and makes sure that X-rays leave the tube only at a certain angle, but also absorbs the X-rays to some extent, thereby weakening the beam. Therefore, the window material is chosen such as to avoid absorption as much as possible. In the wide-field setups, a beryllium (Be) window is used, which absorbs low-energy X-rays, especially those below 1 keV, making it impossible to detect elements below Na (cf. [49]).

The effect of the window on the tube spectrum can be derived from Figure 9, which shows the transmission of a Be window with a thickness of 125 μm as in the Maxi and Tracor setups (see Section 9 for the wide-field setups). As mentioned before, photon energies below 1 keV are blocked completely.

The window modifies the distribution of bremsstrahlung radiation in the low-energy range but has practically no effect on higher energies. These penetrate the window without notable loss, as the transmission function is 1 for energies above 10 keV.

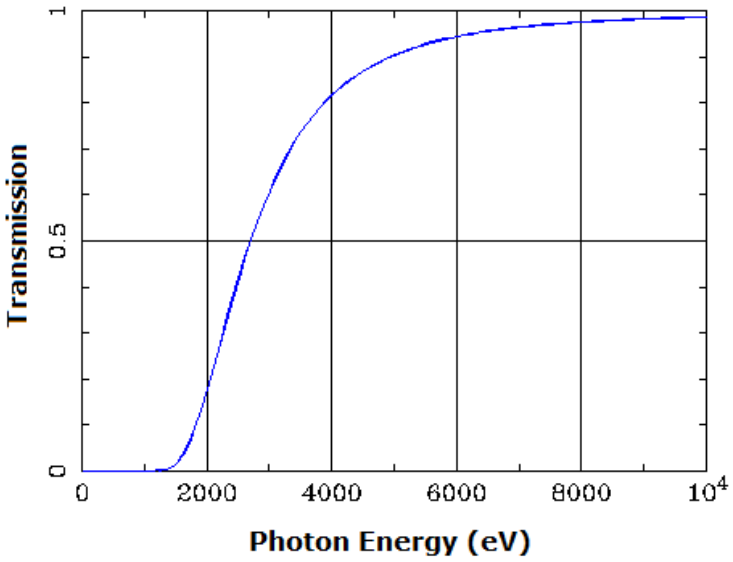

Figure 9: Transmission for a 125 μm Be window. Source: [23]

5.9 Artifacts Introduced by Si(Li) Detectors and SDDs

The working principle of semiconductor detectors is described in [58] and [30].

As a rule, the measured sample spectrum is compromised by detector artifacts, i.e. unwanted events that are caused by processes within the detector and may be misinterpreted as belonging to the characteristic line of a certain element. One can distinguish between *sum peaks*, *escape peaks* and *Compton edges*, which will now be described in greater detail.

5.9.1 Sum Peaks

When two X-rays arrive at the detector at the same time, the detector is unable to distinguish between them. Instead of two separate events, the detector records a single event with an energy equal to the sum of the energies of the two X-rays. *Sum peaks* are also called *pile-up peaks*. (cf. [9], [20])

5.9.2 Escape Peaks

Escape peaks can be detected if the atoms of the detector material are excited by the incoming radiation. For a silicon detector, the Kα line is emitted at approx. 1.7 keV. The energy of the original X-ray will therefore be diminished by these 1.7 keV and contribute to the so-called escape peak. (cf. [9], [20])

5.9.3 Compton Edge

Photons that are scattered by loosely bound detector electrons will transfer part of their energy to these electrons. The energy loss occurring due to this so-called *Compton effect* depends solely on the scattering angle (see Equation 5). The energy transfer will be recorded by the detector, with the *Compton edge* marking the highest possible energy transfer, which occurs at 180°, i.e. when the photon is backscattered from the detector.

Typically, Compton scattering occurs in light elements because they have many loosely bound electrons. The Compton edge will appear at an energy that is lower than the *full-energy peak*, which is caused by the photoeffect, in which the photon delivers its entire energy to the sample material. (cf. [20], [9])

5.10 Noise

In addition to detector artifacts, the measured signal is altered by two sources of noise: amplitude noise and energy noise. While the first noise type is of a statistical nature, the second noise type is provoked by poor signal resolution. (cf. [63])

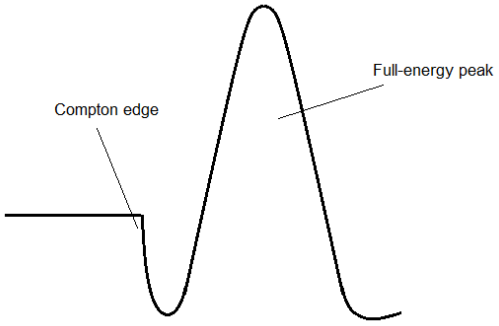

Figure 10: Compton edge and full-energy peak

5.10.1 Amplitude Noise

The first type of noise is due to statistical fluctuations. The photon counting process follows a Poisson distribution, which dictates that the probability $prob$ of finding N events within a specific energy range (for example, a detector channel) can be described by the following relation (cf. [55], [63]):

$$prob(N) = \frac{M^N \cdot e^{-M}}{N!}, \tag{17}$$

where M is the true number of events.

This equation applies if the count rate is constant and the events are assumed to be independent. Since the standard deviation σ is proportional to the square root of N, deviations will have a larger effect if the number of events is small, which means that the concentration of an element is low. For a large number of counts, the Poisson distribution can be approximated by the Gaussian distribution.

5.10.2 Energy Noise and Fano Factor

The second type of noise is caused by the limited resolution of the detector. Although X-rays have a natural line width of only a few electronvolts, the detected peaks are much wider due to poor detector resolution. The peaks of different elements may overlap, and small peaks may be "swallowed up" entirely by large peaks. This effect is more severe for high-Z elements, as they have a larger natural line width to begin with. (cf. [63])

The effect of energy noise on the measured spectrum is illustrated in Figure 11. A small peak that overlaps with a large peak will not be identified but will instead contribute to the intensity of the large peak.

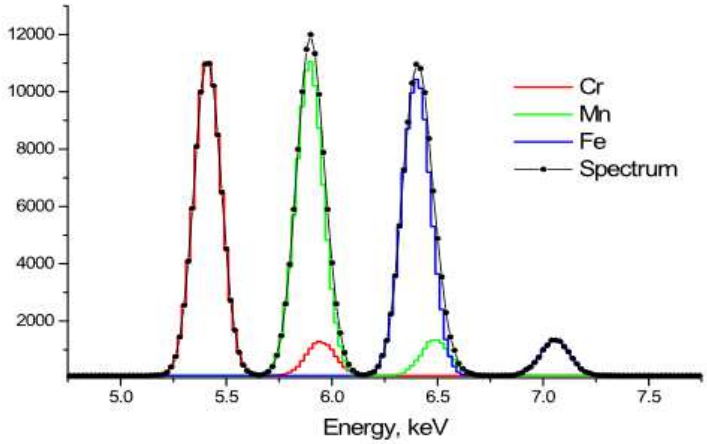

Figure 11: Peak overlap and resulting deviations. Source: [63]

Modern deconvolution routines are able to strip small peaks from larger ones if other peaks of the same element are available (for example, the Kα line can be estimated if the Kβ line is visible). (cf. [51])

Energy resolution is often described in terms of the FWHM (full peak width at half the maximum height). It has been found that the total FWHM resolution can be approximated by the following expression (cf. [28]):

$$FWHM = \sqrt{\Gamma^2 + (2.35 \cdot \sqrt{F \cdot E \cdot \epsilon})^2}, \tag{18}$$

with

$$F(E) = \frac{\sigma^2}{n}, \tag{19}$$

where Γ is electronic noise,
E is the X-ray energy,
ϵ is the pair creation energy,
F is the Fano factor,
n is the mean number of electron-hole pairs produced by an X-ray of energy E and
σ^2 is the variance of n.

Electronic detector noise Γ is usually in the range from 90 to 120 eV (cf. [28], p. 147). The Fanno factor for silicon detectors as used in the present thesis is approximated by 0.11 (cf. [28], p. 147, [6]), while it is only 0.08 for high-purity germanium (HP Ge) detectors (cf. [6], p. 221).

Convention dictates that detector resolution should be reported with respect to the Mn Kα line at 5.9 keV. For a germanium detector, ϵ is 2.8 eV; for silicon, it is 3.6 eV (cf. [47], p. 352). This leaves us with a minimum FWHM resolution of 124 eV for the germanium and 145 eV for the silicon detector.

5.11 Influence of the Tube Voltage on the Emitted Spectrum

According to the Duane-Hunt Law (see Section 5.4), the maximum energy observed in the tube spectrum – and, consequently, in the measured sample spectrum – corresponds to the set tube voltage. The energy range of the measured radiation will therefore become larger with higher tube voltages.

Apart from extending the range of X-ray energies, an increase in voltage causes a rise in intensity below 3 keV due to multiple scattering of electrons in the anode. This is crucial in the analysis of light elements, because the tube voltage does not only boost fluorescence intensity but also enhances the bremsstrahlung background. The signal-to-noise ratio will therefore be lower for light elements and high tube voltages. (cf. [21])

5.12 Influence of Dead Time on the Signal

The electronics involved in counting X-ray photons require a certain amount of time to process each signal. During that time, no other photon can be detected. Long dead times therefore weaken the signal.

What's more, low dead time trades off with energy resolution, as the latter depends on the exactness of the pulse shape. Reducing dead time means reducing pulse shaping time and thus diminishes resolution. (cf. [48])

5.13 Geometric Considerations

The measured spectrum strongly depends on the length of air paths between the tube and the sample and between the detector and the sample. Air paths will cause significant absorption as described by the Beer-Lambert Law (see Section 5.5). This also means that part of the signal is lost and less intensity will be available for sample irradiation and, subsequently, detection (see Section 5.8).

Further factors that will influence the measured intensity are the incidence angle of the electron beam and the detector angle. As the electron incidence angle increases, the bremsstrahlung spectrum will decrease.

For normal incidence angles (α = 0, see Figure 12), the electron beam will irradiate the smallest possible area and thus the smallest electron path length, which will in turn cause the smallest attenuation of the electron beam. By the same token, smaller take-off angles will increase the distance the generated radiation will have to travel within the sample and will lead to stronger attenuation within the sample. At large take-off angles of 20° or more, the photon flux (and thus intensity) is almost independent of the angle. (cf. [52])

The general case is illustrated in Figure 12, in which α is the electron incidence angle, β is the X-ray takeoff angle, γ is the X-ray incidence angle on the window, Ω is the solid angle of primary radiation and d is the sample thickness.

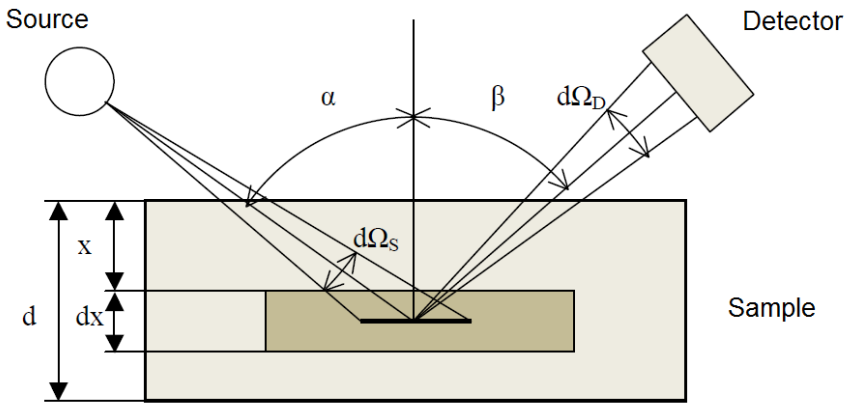

Figure 12: Arrangement of source and detector. Source: [20]

5.14 Relationship between Intensity and Concentration

Sherman (cf. [53]) was the fist to calculate fluorescence intensity for a known specimen composition. Later, his formula was corrected by Shiraiwa and Fujino (cf. [54]).

Starting from the Beer-Lambert Law (see Section 5.5), the primary fluorescence intensity for the j-k line of element i can be calculated by integrating the following expression (cf. [20], [18] and [52] for energy-dependent intensity and [61] for the calculation of wavelength-dependent intensity):

$$I_{ijk}(E) = \frac{d\Omega_s d\Omega_d}{4\pi cos\alpha} \cdot p_{ijk} \cdot \omega_{ij} \cdot \epsilon(E_{ijk}) \cdot c_i \cdot \rho_c \cdot \int_{E_{min}}^{E_{max}} dE \int_0^d dx \cdot I_0(E) \cdot exp(-[\frac{\mu_c(E)}{\rho_c} \cdot \frac{1}{cos\alpha} + \frac{\mu_c(E_{ijk})}{\rho_c} \cdot \frac{1}{cos\beta}] \cdot \rho_c \cdot x) \cdot \frac{\tau_i(E)}{\rho_i} \cdot S_{ij}(E), \quad (20)$$

where $I_0(E)$ is the emitted radiation intensity at an energy of E,
Ω_s is the solid angle of source emission (see Figure 12),
Ω_d is the solid angle of detection,
α is the angle of X-ray emission from the source (see Figure 12),
β is the angle of fluorescence emission from the sample,
p_{ijk} is the emission probability for the j-k line of element i,
ω_{ij} is the fluorescence yield for shell j,
$\epsilon(E)$ is the detector efficiency at an energy E,
E_{ijk} is the energy of the j-k line of element i,
μ_c is the linear absorption coefficient of the sample,
μ_i is the linear absorption coefficient of element i,
d is the thickness of the sample,
$S_{ij}(E)$ is the probability of ionization of shell j at an energy E,
ρ_i is the mass density of element i,
ρ_c is the mass density of the sample, and
$\frac{\tau_i(E)}{\rho_i}$ is the mass photoabsorption coefficient of element i at an energy of E.

The factor of 4π in the denominator of the first fraction is due to the fact that only part of the fluorescence radiation (which is emitted uniformly into all directions, cf. [61]) is collected by the detector.

The two exponential functions result from the attenuation of the source radiation on its way to the sample and of the fluorescence radiation from the sample to the detector. The minimum and maximum energies (E_{min} and E_{max}) are the energy of the j edge of element i and the maximum energy of the primary spectrum, respectively.

Integration over all depths x results in the following formula:

$$I_{ijk} = \frac{d\Omega_s d\Omega_d}{4\pi cos\alpha} \cdot \epsilon(E_{ijk}) \cdot c_i \cdot d \cdot \rho_c \cdot \int_{E_{min}}^{E_{max}} dE \cdot I_0(E) \cdot A(E) \cdot \sigma_{ijk}(E) \cdot S_{ij}(E), \quad (21)$$

with

$$A(E) = \frac{1 - exp(-[\frac{\mu_c(E)}{\rho_c} \cdot \frac{1}{cos\alpha} + \frac{\mu_c(E_{ijk})}{\rho_c} \cdot \frac{1}{cos\beta}] \cdot \rho_c \cdot d)}{[\frac{\mu_c(E)}{\rho_c} \cdot \frac{1}{cos\alpha} + \frac{\mu_c(E_{ijk})}{\rho_c} \cdot \frac{1}{cos\beta}] \cdot \rho_c \cdot d} \tag{22}$$

and

$$\sigma_{ijk} = p_{ijk} \cdot \omega_{ij} \cdot \frac{\tau_i(E)}{\rho_i}. \tag{23}$$

In the experiments presented in this thesis, only thick samples were used. For thick samples, one can assume that

$$d \to \infty, \tag{24}$$

whereby the exponential factor in the absorption term $A(E)$ approaches zero. $A(E)$ then simplifies to

$$A(E) = \frac{1}{[\frac{\mu_c(E)}{\rho_c} \cdot \frac{1}{cos\alpha} + \frac{\mu_c(E_{ijk})}{\rho_c} \cdot \frac{1}{cos\beta}] \cdot \rho_c \cdot d}, \tag{25}$$

and intensity for element i and line j-k becomes

$$I_{ijk} = \frac{d\Omega_s d\Omega_d}{4\pi cos\alpha} \cdot \epsilon(E_{ijk}) \cdot c_i \cdot \int_{E_{min}}^{E_{max}} dE \cdot \frac{I_0(E) \cdot \sigma_{ijk}(E) \cdot S_{ij}(E)}{[\frac{\mu_c(E)}{\rho_c} \cdot \frac{1}{cos\alpha} + \frac{\mu_c(E_{ijk})}{\rho_c} \cdot \frac{1}{cos\beta}]}. \tag{26}$$

The above description applies to primary fluorescence only. As explained in Section 1, secondary fluorescence and matrix effects have to be considered to provide a more complete picture of interaction processes within the sample.

In addition to primary fluorescence induced by tube radiation, XRF analysis software also accounts for excitation of low-Z elements by high-energy fluorescence photons emitted by other elements within the sample (inter-element effect, e.g. Ni on Fe and Cr).

6 Fundamental Parameters

In the fundamental parameters (FP) approach, the physical absorption and scattering processes occurring in the sample upon irradiation with X-rays are represented by a set of equations. These equations are based on the theoretical relationship between characteristic radiation, which is emitted by the sample upon excitation with X-rays, and the concentration of the corresponding elements within the sample. The fluorescence emitted by a specimen is calculated by correcting the incident X-ray tube spectrum for transition probabilities, scattering, absorption within the sample, absorption by filters, absorption in air or helium on the beam path before and after the sample, fluorescence yields, geometrical considerations as well as detector efficiency, artifacts and possible signal offsets. (cf. [50], [44], [52])

As elemental concentrations within the sample are based entirely on fundamental parameters and the (simulated) tube spectrum, errors resulting from approximation and simulation, empirical calibration of the tube spectrum or the mere choice of fundamental parameters are propagated when the concentration is calculated. Inaccurate measurements or calculations may thus give rise to non-negligible deviations from the true concentration values. For this reason, one has to know the incident beam intensity and characteristics as well as the tube geometry with high accuracy. (cf. [37])

This is even more true for empirically obtained fundamental parameters, for example the efficiency of the detector, which is determined by comparing the measured and the calculated tube spectra. Another example of a parameter that is affected by measurement errors is the self-absorption of characteristic lines by the sample and the anode. Self-absorption does not only depend on the anode and sample thicknesses, but also on the characteristic line under investigation, with absorption being particularly strong for low-energetic X-ray lines like Al and Si. (cf. [22])

The most important source of errors is probably the choice of fundamental parameter model itself, as it may have too many or too few parameters and may be valid for a specific geometry only. (cf. [61])

Several FP models were used in this thesis. First, the software BGXRF-Part, with which the quantification of elements was performed (see Section 10), allows the user to calculate the continuous tube spectrum according to either Wiederschwinger's or Love & Scott's model (cf. [20], see Section 10).

Second, the function simulating the absorption process in the window and sample may be considered a fundamental parameter model. It is based on the Beer-Lambert Law, Kramers' Law and the assumptions underlying these laws (see Section 5). Materials and behaviors for which these assumptions are not (fully) true can cause deviations that are not accounted for in these models.

The third model is the setup geometry. Although most distances and angles have been carefully measured, there are a few parameters like the exact anode thickness and the active detector layer that are known only approximately or are fraught with a high empirical variance.

7 Micro-X-Ray Fluorescence Analysis (μXRF)

7.1 Conventional μXRF

In X-ray microanalysis, X-ray optics installed on the source side are used to focus the X-ray beam onto a small spot in the micron range. The use of optics has the advantage of preserving most of the focal intensity and achieving small spot sizes at the same time. Since information is collected only from this small area, one can analyze the (1D or 2D) distribution of elements within the sample, with the resolution depending on the spot size. (cf. [4])

7.2 Confocal μXRF

The confocal geometry allows one to examine the spatial distribution of elements within a three-dimensional sample area. In contrast to conventional μXRF setups, an optical system is used on both the source side and the detector side. This way, the fluorescence signal is collected only from the region of the sample where the cones of the incident beam and the fluorescence beam intersect. This intersection is called the *confocal volume*. By scanning each xy layer of the sample within a certain depth z, a three-dimensional map of the composition of the sample can be obtained. (cf. [42], [65])

The functioning principle of confocal fluorescence spectrometry is illustrated in Figure 13. Focusing is achieved by two capillary lenses denoted L1 and L2.

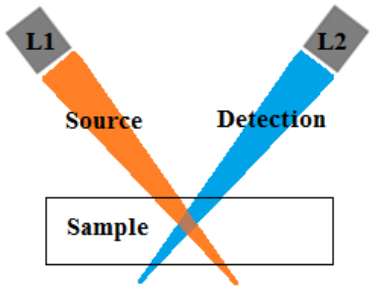

Figure 13: Confocal setup.

Similarly to conventional μXRF, where resolution is governed by the spot size, spatial resolution in confocal μXRF is limited by the size of the confocal volume. Although spot sizes as small as 10 μm can be achieved with confocal geometries, larger spot sizes may be desirable to reduce the scan time and increase signal intensity.

This brings us to the main disadvantage of confocal setups: as the fluorescence signal originates from a very small area, namely the confocal volume, signal intensity is much lower for confocal geometries than for conventional ones, and stronger input signals (i.e. higher currents) need to be provided. (cf. [42])

8 Confocal Setup

8.1 Coordinates

The monochromatic confocal setup described herein has 11 degrees of freedom, which means that 11 coordinates need to be adjusted. There are 5 coordinates for the entrance capillary (x,y,z and two angles) and 3 coordinates each for the detector and the sample. After calibration, the detector coordinates remain fixed, and only the sample coordinates need to be changed. These are presented in Figure 14.

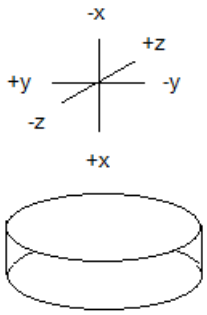

Figure 14: Sample coordinates

8.2 Tube and Detector Parameters

X-rays were produced by a Siemens Kristalloflex 760 generator, which can be operated via a control panel. This source generates a monochromatic molybdenum beam at an energy of approximately 17.4 keV, i.e. the Mo Kα line.

Monochromaticity is achieved by using a Zr foil filter with a thickness of 25 μm, which removes much of the Mo $K\beta$ line as well as the high-energy background radiation. As the absorption of X-rays is considerably weaker just above the absorption edge of the anode element than just below the edge, the filter material is chosen such as to have an absorption edge just between the $K\beta$ and the $K\alpha$ lines. Such a filter will considerably reduce the $K\beta$ line but will only have minor effects on the $K\alpha$ line. (cf. [7])

The detector is a Bruker SDD detector with an area of 30 mm². A 30 mm² detector collimator with 0.5 mm thin silver plates was installed to absorb scattered radiation and reduce the incoming flux for the detector and electronics.

The tube is cooled with water and has a maximum power of 2 kW. The tube and detector parameters are listed in Tables 2 and 3. Please note that the contact layer material and thickness are based on qualified assumptions.

Parameter	value
Anode material	Mo
α (°)	0
β (°)	84
γ (°)	0
Window material	Be
Window thickness (μm)	300
Ω (sr)	1

Table 2: Confocal tube parameters

Parameter	value
X-ray incidence angle (°)	0
Window material	Be
Window thickness (μm)	8
Distance window-detector (cm)	0.5
Detector area (mm^2)	30
Contact layer material	Al
Layer thickness (nm)	20
Detector material	Si
Inactive layer thickness (μm)	0.05
Active layer thickness (mm)	0.5

Table 3: Confocal detector parameters

8.3 Capillaries

Two helium-filled capillary lenses by Fischer (Polycapillary Semi-lenses 246mls26 and 236mls13) were used to focus the incident beam and the resulting fluorescence signal. Filling the tubes with helium eliminates the need for evacuation, as helium cannot be detected in EDXRF analysis and therefore does not interfere with the measured signal.

Semi-lens 246mls26 ("lens 1") was placed in the incident beam path and semi-lens 236mls13 ("lens 2") was placed in the outgoing beam path. The capillaries are shown in Figure 15.

The most important capillary parameters and dimensions are given in Table 4 and Figure 16, with D_{in} and D_{out} representing the entrance and exit diameters, respectively. All values are in mm.

	f	L	D_{in}	D_{out}
Lens 1	5.1	39.4	7.4	2.15
Lens 2	4.9	40.3	6.35	1.9

Table 4: Capillary parameters

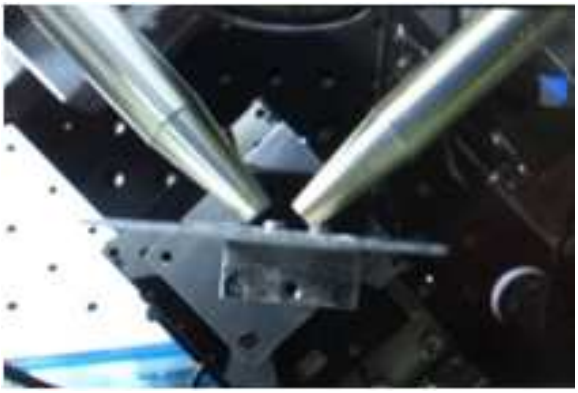

Figure 15: Confocal capillary setup.

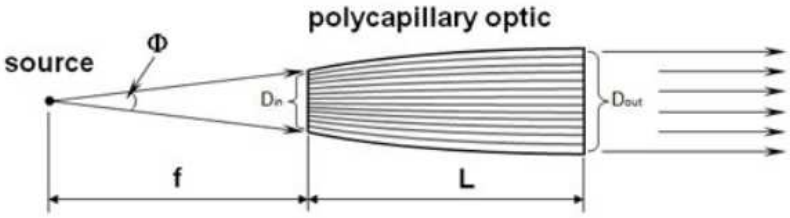

Figure 16: Capillary dimensions. Source: [15]

8.4 Sample Movement and Controls

Movement of the sample is achieved by piezoelectric motors and observed via a camera. The motors of the sample stage and the capillaries can be controlled via a command line. The most important commands are listed in Table 5.

Command	Meaning
mva	absolute movement
mvr	relative movement
set target current x	sets the tube current to x mA
set target voltage x	sets the tube voltage to x kV
scanprep	sets the parameters for the next scan
scanprep count	starts the scan as defined above

Table 5: Commands

9 Wide-Field Setups

9.1 Maxi Setup

The first wide-field setup, the "Maxi" setup (see Figure 17), is equipped with an Amptec Mini-X tube. The Amptec Mini-X has a rhodium anode, which is directly sputtered onto a 125 µm beryllium window, thereby reducing anode thickness to approximately 1 μm.

Transmission tubes are generally used due to their close anode-sample coupling, the higher flux beam and the reduced attenuation of the lower energy range of the primary spectrum. Their disadvantage lies in the inefficient dissipation of heat, which limits output power to a few Watts. (cf. [46])

The maximum output power of the Maxi tube is 4 W. A brass collimator with a pinhole diameter of 1 mm was placed at the end of the tube to decrease the flux and filter out possible impurities arising from the anode brazing process. The hole and the end face of the collimator were cladded with Al to obtain a clean blank spectrum.

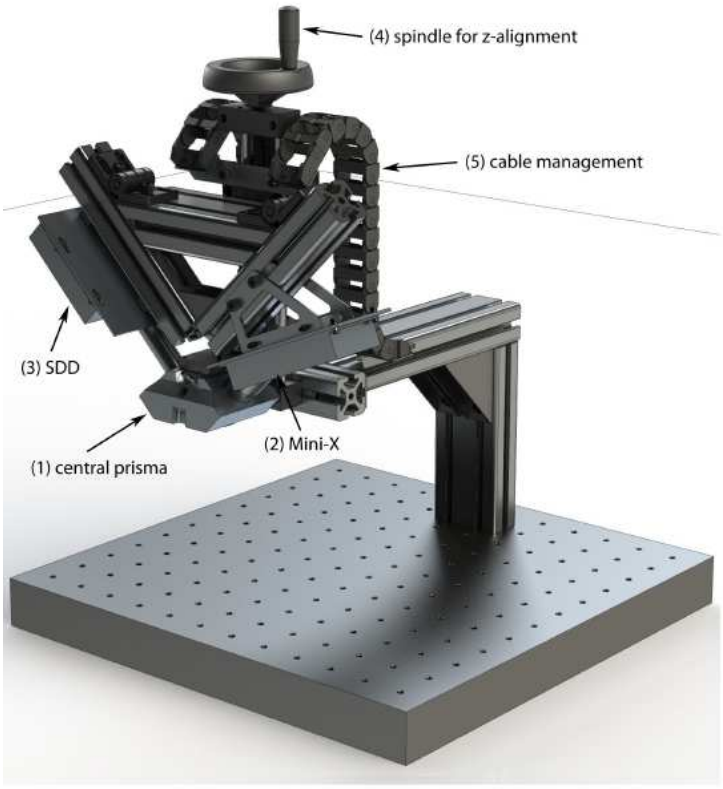

Figure 17: Maxi setup. Source: [2]

The detector is an air-cooled Si(Li) SDD detector with an area of 80 mm^2 and an inbuilt Zr collimator. The detector has a 12.5 μm Be window in front. The tube environment is air, which complicates the measurement of silver, because the argon peak will partly overlap with the silver peak. The air path before and after the sample has a length of 25 mm.

The tube window material is beryllium, although its thickness is higher than in the confocal setup, which can be explained by the higher radiation flux originating from the larger area of irradiation. The detector resolution is approximately 200 eV. The tube and detector parameters for the first wide-field setup are listed in Tables 6 and 7, respectively.

Parameter	value
Anode material	Be
α (°)	0
β (°)	0
γ (°)	0
Window material	Be
Window thickness (μm)	125
Ω (sr)	1

Table 6: Maxi tube parameters

Parameter	value
X-ray incidence angle (°)	0
Window material	Be
Window thickness (μm)	12.5
Distance window-detector (cm)	0.5
Detector area (mm^2)	80
Contact layer material	Al
Layer thickness (nm)	20
Detector material	Si
Inactive layer thickness (μm)	0.05
Active layer thickness (mm)	0.5

Table 7: Maxi detector parameters

9.2 Tracor Setup

In addition to the Maxi tube spectrum, the spectrum of the tube used for calibration of the analysis software package (BGXRF-Part) was recorded. This calibration setup is a Tracor Spectrace 5000 spectrometer, a side-window tube that has a thicker rhodium anode than the Maxi tube, while the beryllium window is of the same thickness as the Maxi window. Despite having the same anode material, the Tracor geometry, which is outlined in Figure 18, differs greatly from the Maxi setup not only in terms of anode thickness but also as regards incidence and take-off angles.

What may, however, be most important for the present thesis is that the Tracor setup is equipped with a different detector. Apart from the difference in the contact layer material, one should note that the active detector layer is 3 mm as compared to 0.5 mm for the Maxi tube, thus providing a much better detector efficiency.

The Tracor tube and detector parameters are presented below.

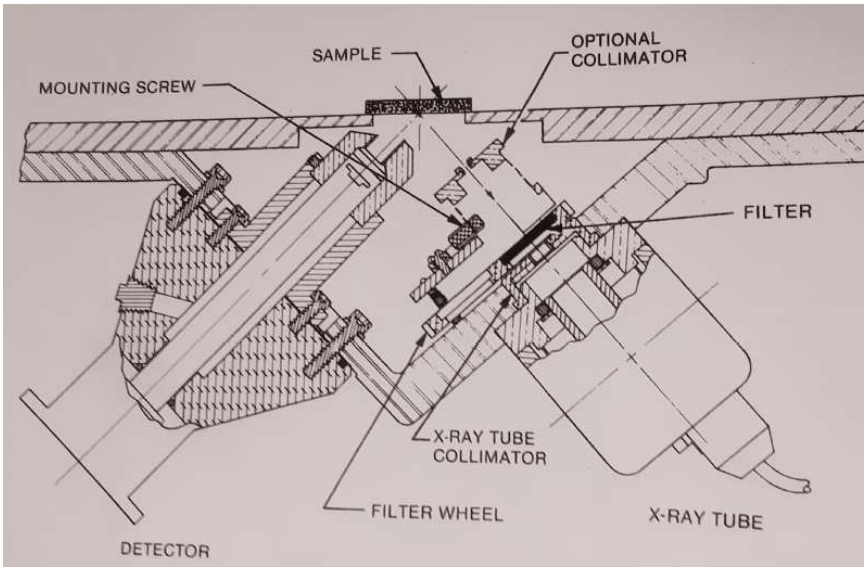

Figure 18: Tracor geometry. Source:[57]

Parameter	value
Anode material	Rh
α	20
β	70
γ (°)	0
Window material	Be
Window thickness (μm)	125
Ω (sr)	1

Table 8: Tracor tube parameters

Parameter	value
X-ray incidence angle (°)	0
Window material	Be
Window thickness (μm)	12.5
Distance window-detector (cm)	0.5
Detector area (mm^2)	30
Contact layer material	Au
Layer thickness (nm)	20
Detector material	Si
Inactive layer thickness (μm)	0.05
Active layer thickness (mm)	3

Table 9: Tracor detector parameters

9.3 Detector Efficiency

A key point to remember is that filters – mathematical or physical – will influence not only the spectrum, but also the detection efficiency, as they might lower or cut off part of the spectrum.

The efficiency of a detector is defined as the ratio of the number of photons emitted by the sample within a certain energy range and the number of detected events within this range. Efficiency is a measure of how well the detector converts X-rays into the signal to be processed and evaluated. It depends on the geometry of the setup and the energy of the radiation to be detected. Detector efficiency can change over time due to depositions on the window, which will compromise the detection efficiency of low-Z elements. (cf. [33])

For the purposes of this thesis, it is particularly important to point out that the detector efficiency differs considerably for the Maxi and the Tracor setups. This is illustrated in Figure 19, which shows that the efficiency of the Maxi detector starts to drop at approximately 10 keV, while the efficiency of the Tracor detector starts to decline at a much higher energy of approximately 20 keV. In conclusion, the Tracor detector is much more efficient in the high-energy range when compared to the Maxi detector, and it is very likely that the Maxi spectrum requires correction in this area to avoid quantification errors.

Apart from the lower sensitivity in the high-energy range, the efficiency of the Maxi detector as presented in Figures 19 and 20 exhibits a jump in the low-energy range, which is owed to the relatively long air path between the sample and the detector.

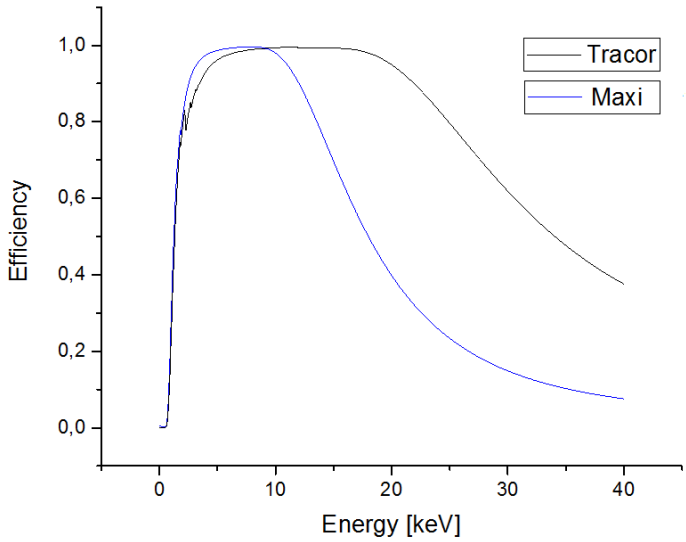

Figure 19: Comparison of detector efficiencies for the wide-field setups

Filters may also influence detector efficiency. Figure 20 compares the Maxi detector efficiency with and without a mathematical E^2 filter (see Section 14.1). One can see that the filter greatly reduces efficiency in the low-energy range.

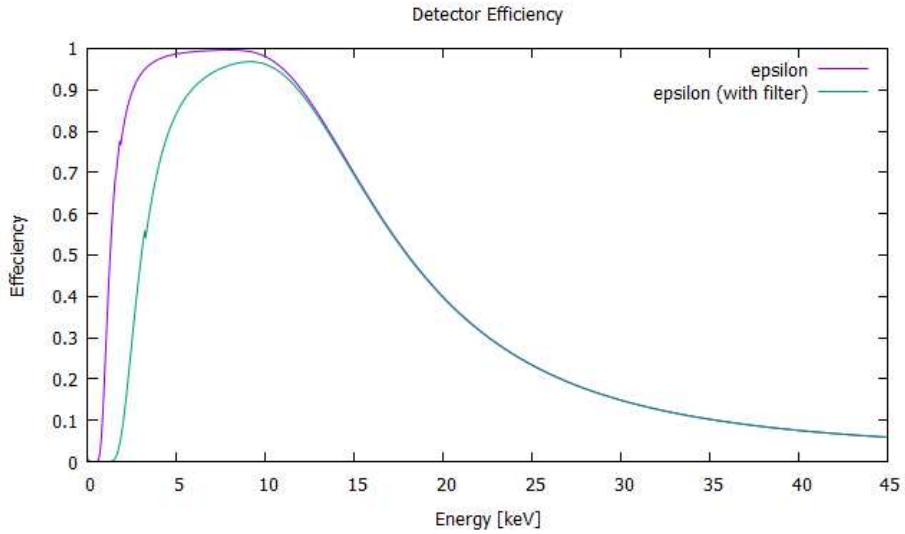

Figure 20: Maxi detector efficiency for measured (magenta) & E^2-corrected (green) spectra.

10 Software

10.1 Data Acquisition and Display

The Tracor Spectrace is equipped with its own recording software. The file format can be converted into .spe files using AXIL (see below). The Tracor user interface is shown in Figure 21.

Data acquisition for the confocal setup and the Maxi setup was performed with the XSPECT software package, which was originally developed by a Master student. Its user interface is shown in Figure 22.

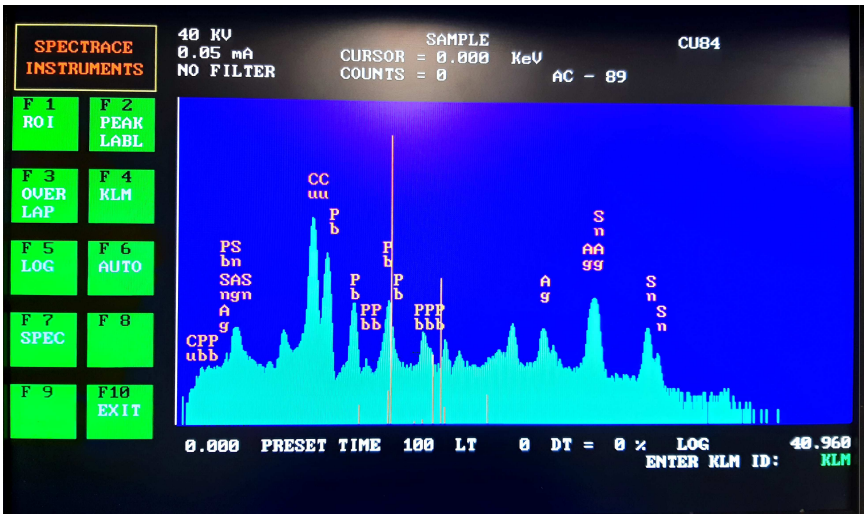

Figure 21: Tracor user interface.

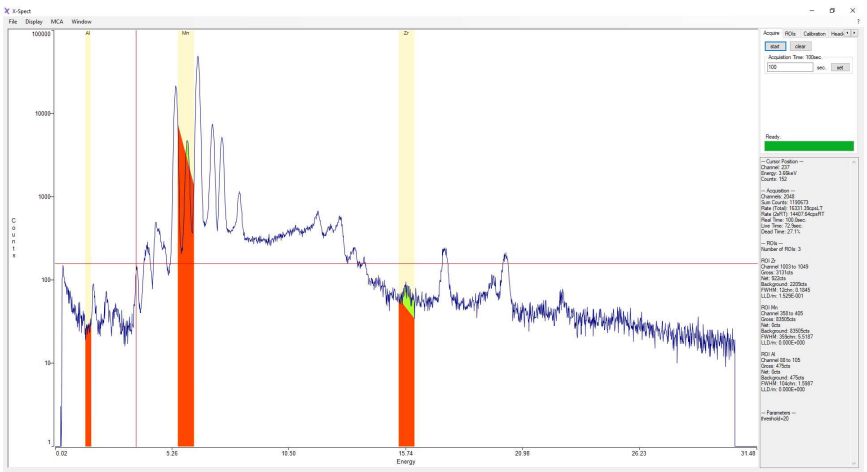

Figure 22: XSpect user interface.

10.2 Peak and Background Fitting

PyMCA, a freeware tool for X-ray fluorescence analysis provided by the European Synchrotron Radiation Facility (ESRF), and the spectrum-fitting tool AXIL (Analysis of X-ray spectra by Iterative Least squares) of QXAS (Quantitative X-ray Analysis System), a DOS-based software originally developed by the International Atomic Energy Agency (cf. [26]), were used to fit the measured spectra. Each program separates the peaks from the bremsstrahlung and noise background to determine the count numbers.

Both PyMCA and AXIL permit the user to choose from several background fit functions. In AXIL, one can select from a linear background, bremsstrahlung, orthogonal polynomials and mathematical functions. Moreover, the user can set a noise threshold. In PyMCA, the background options are linear polynomials, exponential polynomials and linear background. The order of the fit function can be set manually in both packages.

In PyMCA, the ratios between individual lines belonging to the same shell can be either fixed (by pressing "L" or "K", depending on the energy range to be evaluated), or one or several lines can be evaluated individually (by pressing "K1" and/or "K2", for example, where "K1" is the Kα and "K2" is the Kβ line). IN AXIL, only the Kα and Lα lines are evaluated.

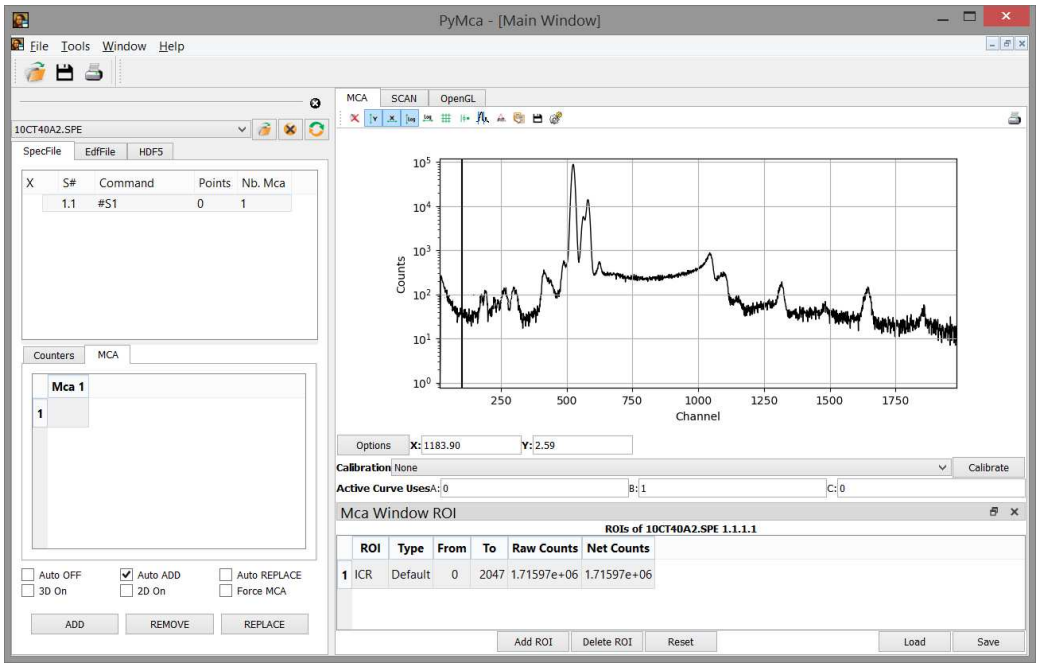

Figure 23: PyMCA User Interface.

It should be noted that in AXIL, X-ray lines are categorized according to the Siegbahn notation, while PyMCA uses the IUPAC notation.

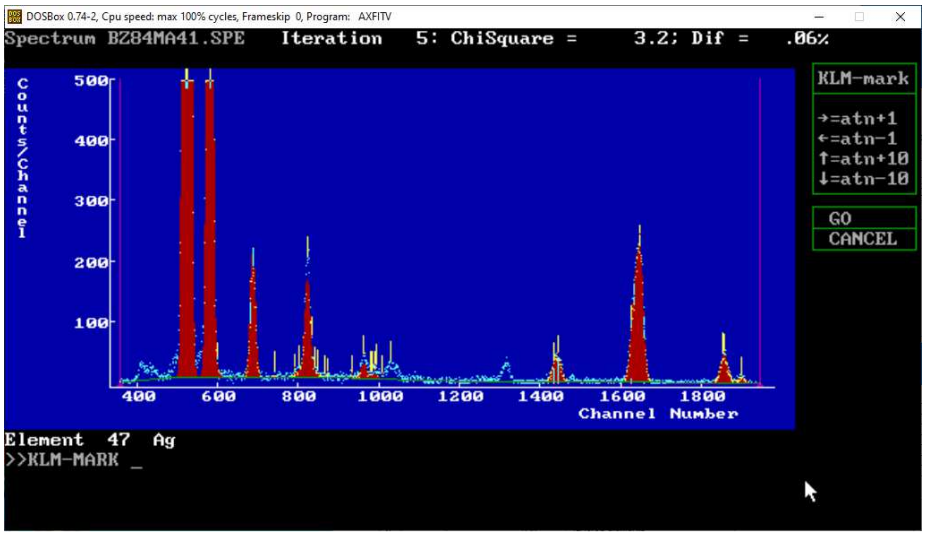

Figure 24: AXIL User Interface.

10.3 Quantitative Evaluation

After background fitting, BGXRF-Part (cf. [20], [39]) was used to calculate the concentrations of elements within the sample. BGXRF-Part was originally tailored to the Tracor setup and evaluates the raw data according to a fundamental parameter model including the tube geometry, the anode and window materials, the sample thickness, the tube voltage and current as well as air gaps and filters. All parameters can be saved in a *property file* that can be loaded upon the start of the program.

As mentioned in Section 6, the user can choose between two models, Wiederschwinger's and Love & Scott's models, to simulate the spectral distribution of X-rays impinging on the sample. In the analyses presented herein, Wiederschwinger's model was used exclusively.

Unwanted elements can be ignored in the calculation of sample concentrations to eliminate the influence of the anode material, collimators and filters on the measured intensity. In the present case, Zr (the collimator material) and Rh (the anode material) were excluded from the analysis. Furthermore, the calculation of concentrations differs for thin and thick samples, which is why the user can select this parameter.

Most importantly, BGXRF-Part supports mathematical filter functions. The calculated spectrum serves as an input parameter and is multiplied with one or more filter functions (cf. [39]):

$$Y(X) = enhancement factor * f(X), \tag{27}$$

where X is the energy in keV.

Figure 25 illustrates the tube settings tab in BGXRF-Part, while Figure 26 shows the user interface for the source filter settings.

For example, Y(X)=cos(X) would mean that the enhancement factor is 1 and f(X) = cos(X). Polynomials can be expressed by $Y(X)=A+BX+CX^2+DX^3$.

The idea of this thesis is to manipulate the spectral intensity with filters to simulate the effect of different tube setups and detectors and thereby improve quantitative analysis (see Section 14).

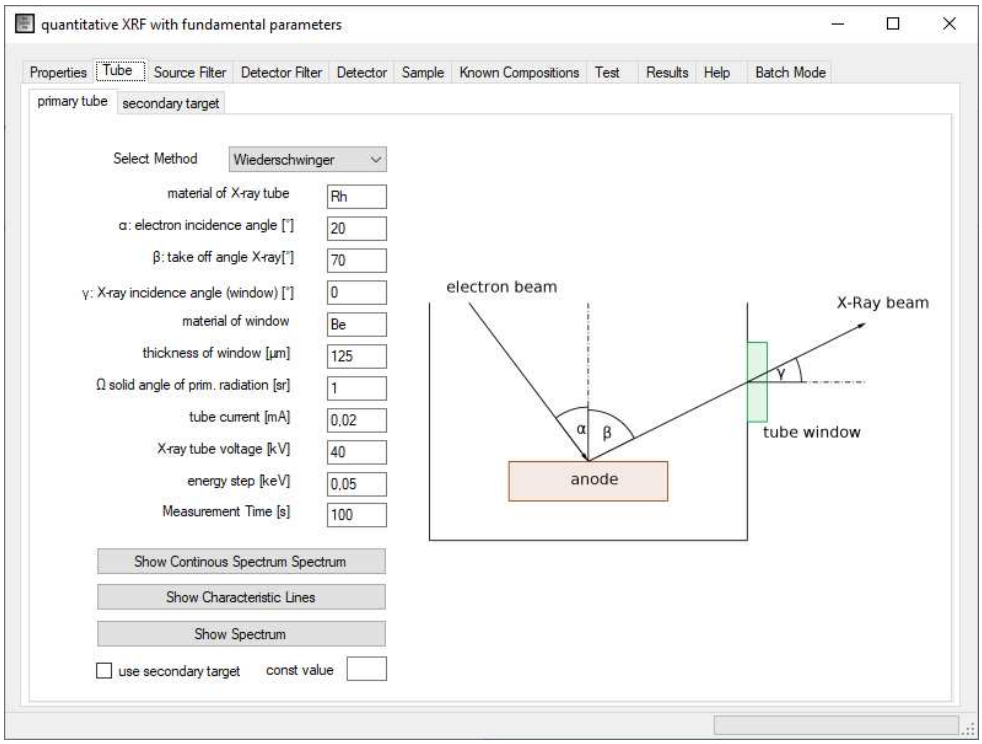

Figure 25: BGXRF-Part Tube Settings Interface.

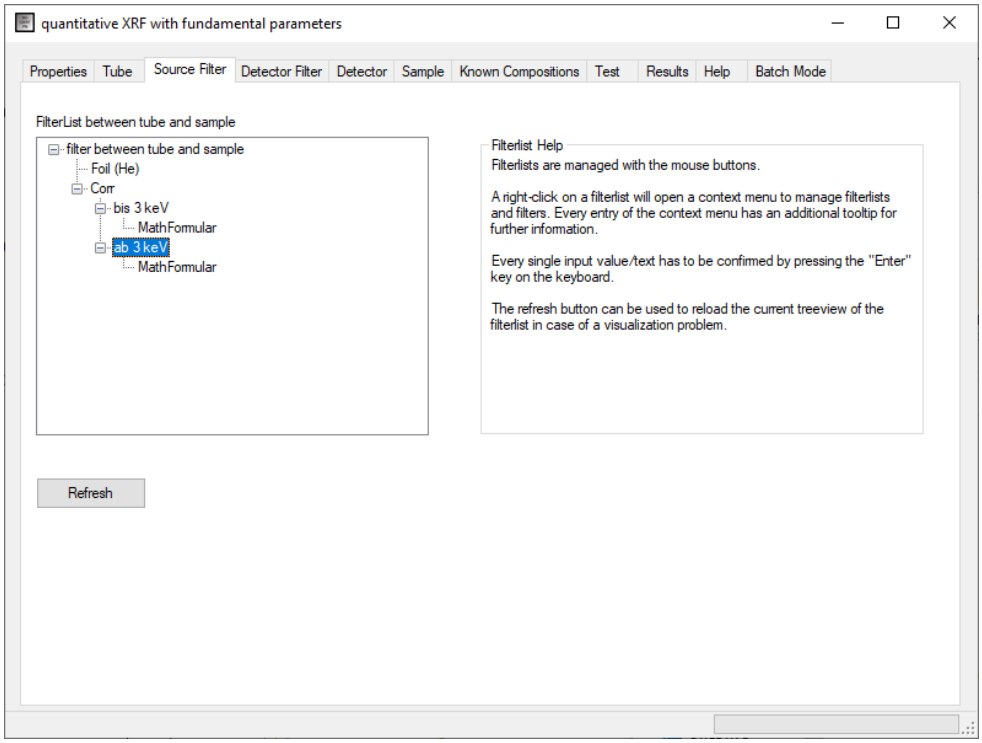

Figure 26: BGXRF-Part Source Filter Settings Interface.

11 Confocal Measurements

To find out whether inaccurate sample quantification was attributable to the incorrect calculation of the primary spectrum or to an inherent flaw of the analysis software BGXRF-Part, the measurements made with the two wide-field setups (Tracor and Maxi) were compared to the results obtained with a confocal geometry (see Section 8).

11.1 Calibration

After installing the detector capillary, its position had to be adjusted such as to optimize the overlap of the incoming and detected beams and thus maximize the intensity of the signal. To this aim, a copper wire was irradiated, and intensity maps were produced in the xz plane of the detector capillary at varying heights y. The smallest spot size that could be achieved with the given setup was 30 x 30 μm. According to the manufacturer, the ideal focus size in the copper energy range is 25 μm, so this result is acceptable.

By the same token, the x coordinate of the sample motor has to be adjusted each time a new sample is mounted. This way one can make sure that the focal region is within the sample. An exemplary intensity map is shown in Figure 27.

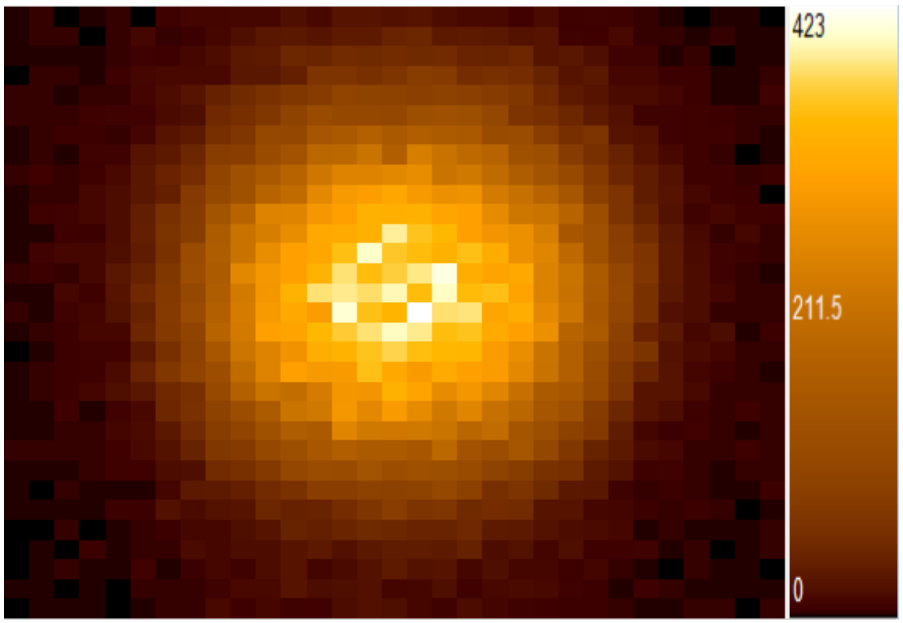

Figure 27: Intensity map in the xz plane of the detector.

11.2 Measurements

3D scans were performed for samples A, B and C. The x coordinates were chosen such as to maximize intensity to compensate for a possible tilt of the sample. Each measurement is defined by three points: the start point, the via point and the end point. Fluorescence was excited with a monochromatic Mo-Kα beam using multilayer optics and confocal polycapillary optics.

The total area of measurement (300 μm x 300 μm) was divided into 15 μm x 15 μm sub-areas, resulting in a total of 421 measurement points and a voxel size of 15x15x25 μm^3. The measurement time was 150 seconds per point, resulting in a measurement duration of 18 hours, 22 minutes and 30 seconds.

The current and voltage settings were 37 mA and 50 kV, respectively. Assuming that the samples are sufficiently homogeneous, using the sum spectrum of all points is feasible, and individual outliers should not distort the results. The following x-ray lines were chosen for quantitative analysis: Cu-Kα, Ag-Lα, Sn-Lα and Pb-Lα.

Figure 28 shows an exemplary sum spectrum (Sample C) recorded with the confocal setup.

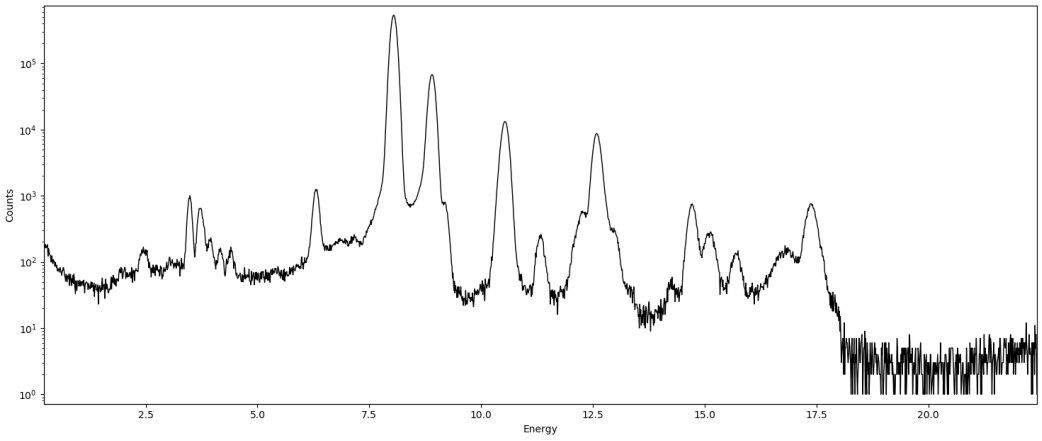

Figure 28: Confocal spectrum of Sample C.

Quantitative analysis was performed in both AXIL and PyMCA. In AXIL, orthogonal polynomials of ninth order were used to calculate the background, while linear polynomials were chosen in PyMCA. In AXIL, The noise level was set to a value of 70 counts to be able to evaluate low-energy lines. Background subtraction then gives the intensities of the characteristic elements.

		Before polishing				After polishing			
		AXIL		PyMCA		AXIL		PyMCA	
Element	Expected	Mean	E_{rel}	Mean	E_{rel}	Mean	E_{rel}	Mean	E_{rel}
Cu	90	91.61	2	92.01	2	92.28	2.5	92.06	2
Ag	2	1.97	2	1.79	11	1.92	4	2.31	16
Sn	4	3.86	4	3.60	10	3.57	11	3.65	9
Pb	4	2.56	36	2.59	35	2.24	44	1.99	50

Table 10: Analysis of sample A

		Before polishing				After polishing			
		AXIL		PyMCA		AXIL		PyMCA	
Element	Expected	Mean	E_{rel}	Mean	E_{rel}	Mean	E_{rel}	Mean	E_{rel}
Cu	84	85.7	2	86.6	3	86.04	2	86.81	3
Ag	1	1.4	40	1.45	45	1.16	16	1.51	51
Sn	10	9.8	2	9.9	1	9.65	3.5	8.91	11
Pb	5	3.0	40	2.9	42	3.15	37	2.77	45

Table 11: Analysis of sample B

Element	Expected	AXIL	E_{rel} AXIL	PyMCA	E_{rel} PyMCA
Cu	79.5	84.96	7	82.42	4
Ag	0.5	0.77	54	0.99	98
Sn	8	8.6	7.5	10.51	0.31
Pb	12	5.68	53	5.89	51

Table 12: Analysis of sample C

Finally, the resulting counts were evaluated using BGXRF-Part with the input parameters as applicable to the confocal setup (see Section 8). To improve their surface quality, samples A and B were polished and the spectral measurements were repeated. Despite polishing, scratches in the μm range could still be observed. The quantitative results of both measurements, with and without polishing, are displayed in Tables 10 to 12. In addition to the calculated and expected weight concentrations, the relative error E_{rel} is given in per cent.

These results show that the Pb and Sn concentrations are systematically too low, especially the Pb values, while the Cu and Ag concentrations are too high. One reason for this could lie in the unresolved issue of low surface quality, which may have led to a variety of incidence angles and could have distorted the results. An additional difficulty is that

the Ag-Lα line overlaps with the Ar- Kα line originating from the air path between the capillaries and the sample.

Furthermore, the sensitivity of the detector capillary is energy-dependent. Capillary optics only transmit X-rays whose angle of incidence is below a critical angle. For larger angles, the X-ray will be absorbed or refracted. X-rays may be cut off and will not be available for the excitation of sample atoms (cf. [35]). This could have affected the value of Pb, whose L line is highest among the evaluated X-ray lines.

Another possible reason for errors could be that the samples are not homogeneous. Homogeneity was therefore analyzed by calculating the mean intensity and the standard deviation. As table 13 indicates, the three sigma rule (and therefore normal distribution) is fulfilled, justifying the assumption of homogeneity and thus quantitative evaluation of the sum spectrum. The number and percentage of values outside the 3σ range is denoted as *no. out* and $\%$ *out*, respectively.

Sample	min	max	mean	3σ	mean-3σ	mean+3σ	no. out	$\%$ out
A	20872	22796	21686	1014	20672	22700	2	0.45
B	18444	20490	19573	1011	18562	20584	3	0.68
C	14958	19653	17341	2457	14884	19798	2	0.45

Table 13: Maximum, minimum and mean intensity for samples A, B and C

Although sample homogeneity is fulfilled from a statistical point of view, one should bear in mind that the confocal setup illuminates a very small spot, and sample concentrations may still differ considerably from one spot to another.

Moreover, the evaluation of L-lines is generally less reliable than the evaluation of K-lines. L-lines are weaker, i.e. there is a lower number of photons to evaluate, and consequently the error related to random fluctuations, which is inversely dependent on the square root of the number of measurement points, is higher (see Section 5.10).

In addition, the occurrence of peak overlaps is high in the low-energy region of the spectrum, where most L lines are located (see Section 1).

The root cause of the incorrect calculation of concentrations could not be derived from the sole analysis of the data obtained with the confocal setup. Consequently, further investigations were carried out using the wide-field setups.

12 Comparison of Measured Wide-Field Spectra

In a first attempt to evaluate the spectrum of the Maxi tube, a perspex disc with a diameter of 30 mm and a thickness of 3 mm was used to measure the Tracor and Maxi tube spectra. The tube radiation was scattered towards the detector at an angle of 90°, i.e. an incidence angle of 45° and an emission angle of 45°. All experimental spectra were measured with a 1 mm tube collimator. The detector of the Maxi setup was a Si drift SDD KETEK with an area of 80 mm², collimated to 30 mm², while the Tracor detector was a Si(Li) detector with an area of 30 mm². All measurements of the primary spectrum were done in air.

The aim was to compare the primary spectra from a qualitative point of view, bearing in mind that both tubes are equipped with a rhodium anode but have a very different anode thickness, geometry and detector efficiency.

To eliminate the effect of the individual detectors, the spectra were divided by the respective detector efficiency. Figures 29 and 30 display both the uncorrected spectrum (black line) and the spectrum divided by the detector efficiency (grey line) for each of the widefield setups. A slight energy shift was introduced in Figure 30 for better visibility.

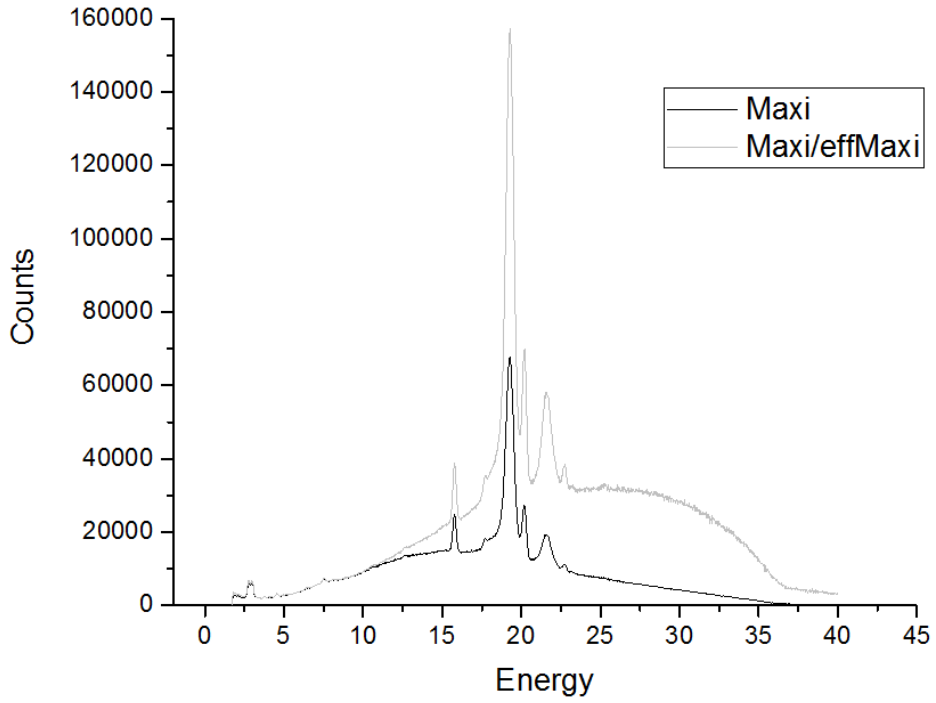

Figure 29: Measured Maxi spectrum (black) & detector-neutral Maxi spectrum (grey).

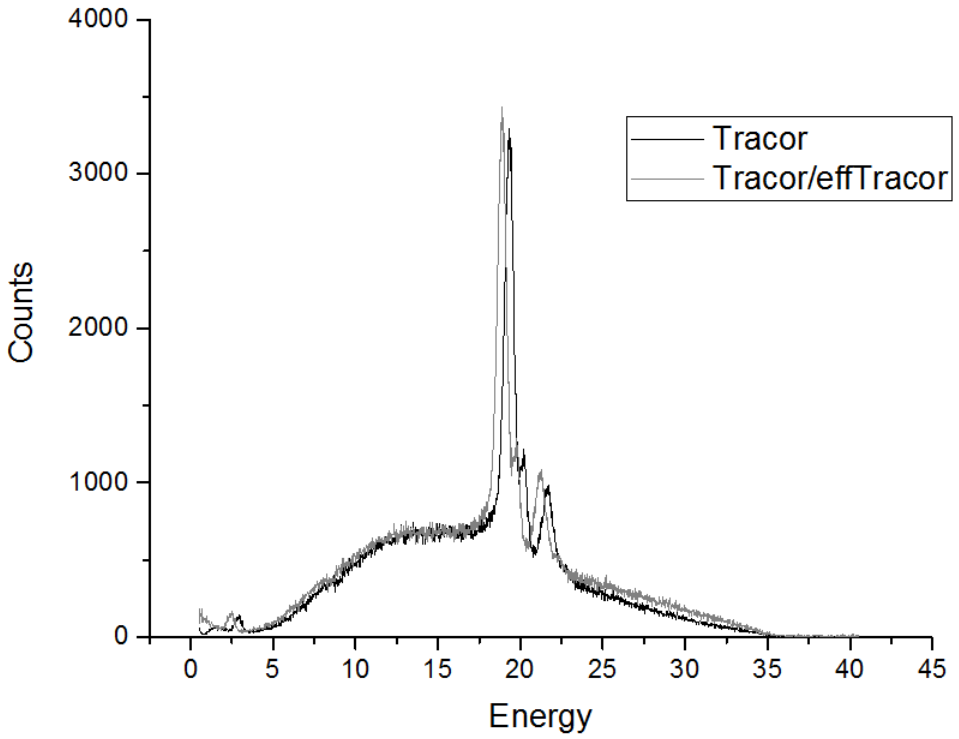

Figure 30: Measured Tracor spectrum (black) & detector-neutral Tracor spectrum (grey).

Beside the differences in maximum intensity, the above figures show that the Tracor detector has only little influence on the shape and intensity of the spectrum, with the original and the detector-neutral curves being nearly identical.

In contrast thereto, the Maxi detector efficiency starts decreasing much earlier than the Tracor detector efficiency and weakens the signal in the high-energy range as evident from Figure 19. Also, the Maxi spectrum shows a Zr-Kα peak at 15.8 keV, which originates from the Zr collimator. Therefore, Zr has to be excluded from the list of detectable elements for analyses with the transmission tube.

To correctly calculate the concentration of elements within a sample after measurement with the transmission-anode setup, one has to enhance the intensity values from 10 keV onward to make up for the drastic intensity drop caused by the detector.

13 Comparison of Simulated Tube Spectra

13.1 Spectral Distribution and Depth of Generation

According to [20] and [39], the continuous spectral distribution ΔN can be calculated based on the following equations. An extensive derivation and explanation of the spectral distribution is also provided by [61] and [52]. This distribution is the basis on which BGXRF-Part calculates the tube spectrum (see Section 10.2).

$$\Delta N(E) = \sigma \cdot f \cdot \Omega \cdot i \cdot t \cdot \Delta E \cdot D(E), \tag{28}$$

where

$$\sigma = const \cdot Z \cdot ((U_0 - 1)^x); \tag{29}$$

$$x = 1.0314 - 0.0032 \cdot Z + 0.0047 \cdot E_0; \tag{30}$$

$$U_0 = \frac{E_0}{E}; \tag{31}$$

$$f = (1 - exp(-2\chi \cdot \rho \cdot z))/(2\chi \cdot \rho \cdot z); \tag{32}$$

$$z = z_m \cdot ln(U_0) \cdot \frac{(0.49269 - 1.0987 \cdot \eta + 0.78557 \cdot \eta^2)}{(0.70256 - 1.09865 \cdot \eta + 1.0046 \cdot (\eta^2) + ln(U_0))}; \tag{33}$$

$$z_m = A \cdot \frac{(0.787 \cdot 10^{-5} \cdot \sqrt{J} \cdot E_0^{3/2} + 0.735 \cdot 10^{-6} \cdot E_0^2)}{\rho \cdot Z}; \tag{34}$$

$$\eta = c \cdot (E_0^{0.1382 - (0.9211/\sqrt{Z})}); \tag{35}$$

$$c = 0.1904 - 0.2236 \cdot log(Z) + 0.1292 \cdot log(Z)^2 - 0.01491 \cdot log(Z)^3; \tag{36}$$

$$J = 0.0135 \cdot Z; \tag{37}$$

$$\chi = \tau(E) \cdot \frac{cos(\alpha)}{cos(\beta)}; \tag{38}$$

f describes the self-absorption of X-rays by the anode material;
E is the energy of interest in keV;
E_0 is the maximum electron energy as defined by the tube voltage;
ρ is the density of the anode material in g/cm³;
Ω is the solid angle of primary radiation in sr;
z is the mean depth of fluorescence generation in cm according to Love and Scott;
z_m is the maximum depth of fluorescence generation in cm;
J is the ionization potential of the anode material in kV;
η is the backscattering coefficient of the anode material;

α is the electron incidence angle;
β is the X-ray takeoff angle;
D is the detector efficiency;
$\tau(E)$ is the mass attenuation coefficient of the anode material (see [40]);
ΔE is the sensitivity of the detector at energy E;
Z is the atomic number of the anode material;
i is the tube current in mA and
t is the duration of measurement in s.

Figure 31 shows the mean depth of fluorescence generation z for rhodium, while Figure 32 presents the maximum depth of generation z_m. Since z and z_m depend solely on the anode material but not on the tube geometry, these illustrations are applicable to both the Maxi and the Tracor tube.

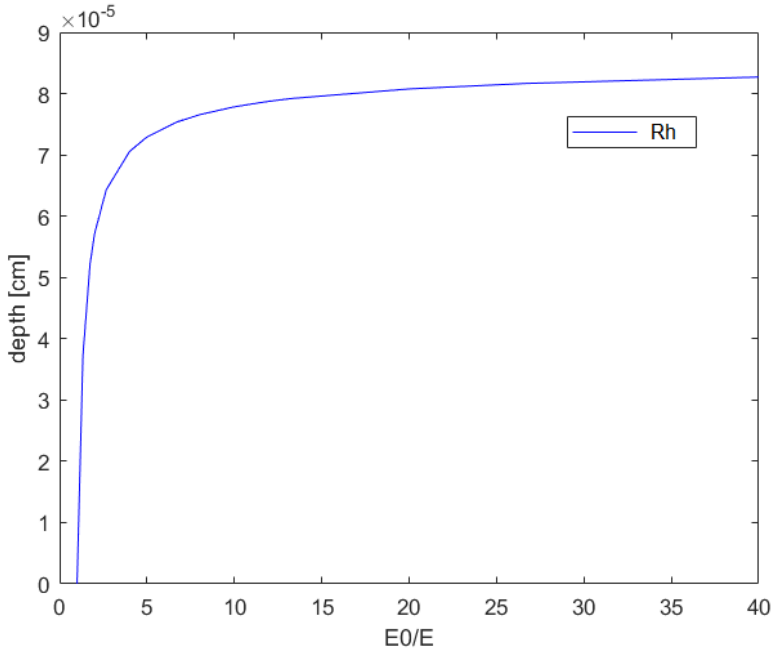

Figure 31: Mean depth of fluorescence generation in Rh.

When one compares the transmission anode thickness of 1 μm to the calculated mean generation depth of approximately 0.8 μm, one can see that the anode thickness is still sufficient to make sure that most X-ray fluorescence is generated within the rhodium target. However, one should consider that the thickness of such thin-film anodes is hard to measure and may differ from the manufacturer's specifications.

Besides, in the Maxi tube, the maximum depth of generation (see Figure 32) is equal to the thickness of the anode, reducing it to 1 μm, which leads to an increase in spectral intensity in the low-energy region due to reduced self-absorption within the anode (see Section 13.2 below).

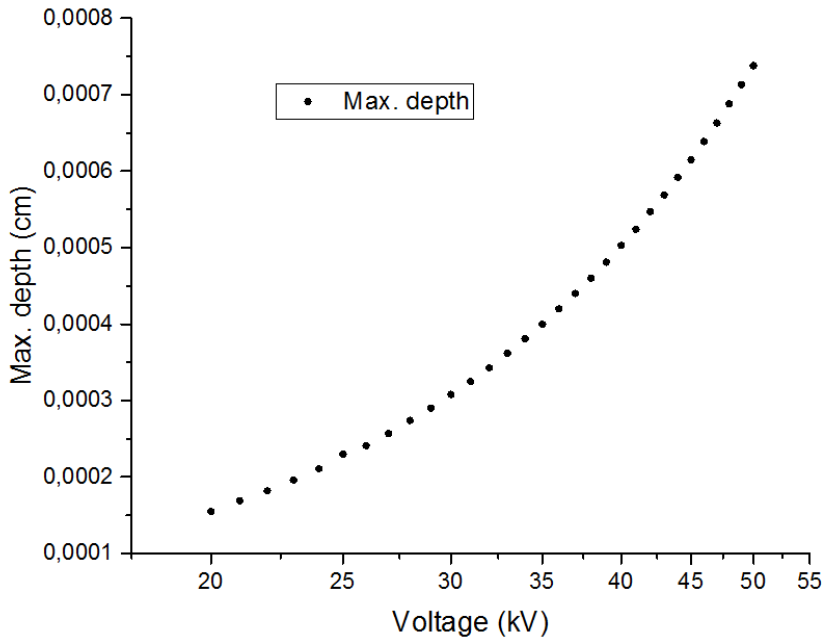

Figure 32: Maximum depth of fluorescence generation in Rh.

13.2 Anode Thickness

Based on the spectral distribution described by Equation 28, thin anodes can be simulated only in so far as the maximum depth of generation will be equal to the thickness of the anode in that case. Since the anode of the Maxi setup is only 1 μm, but the maximum depth of fluorescence generation in rhodium is more than 3 μm as evident from Figure 32, there is reason to believe that the primary spectrum of the transmission tube will differ from a conventional tube.

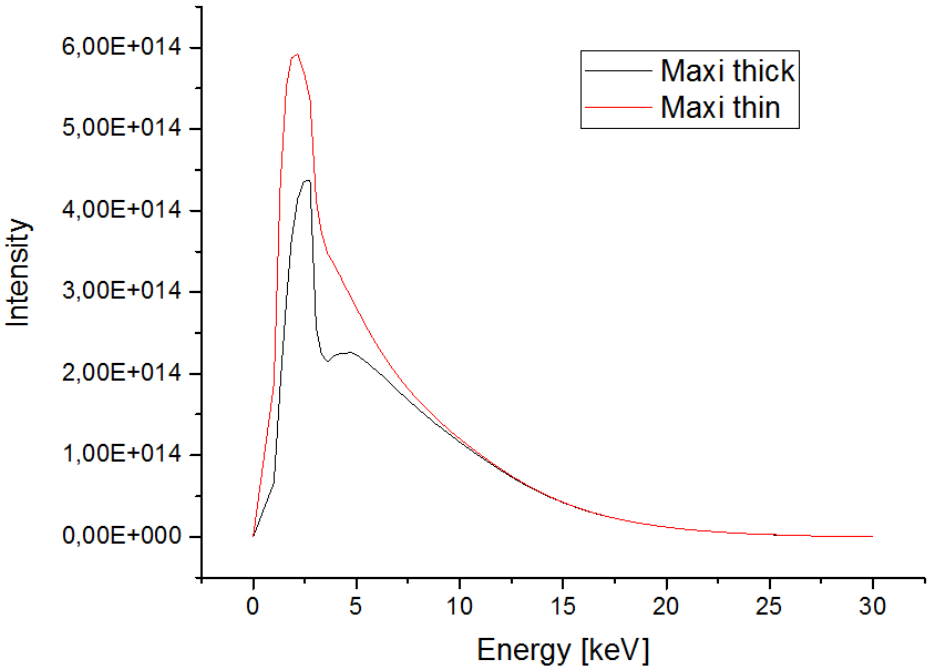

Figure 33: Thin vs. thick anode behavior.

Against this background, the continuous spectral distribution according to Equation 28 was calculated for the full and the reduced depth of fluorescence generation. The simulation was carried out for a tube voltage of 30 kV due to a lack of data for higher energies. Indeed, Figure 33 suggests that in the low-energy range, the continuum is much higher for the thin anode as compared to an anode whose thickness is greater than the maximum depth of fluorescence generation.

The thin-anode behavior can be approximated by changing the incidence and detection angles, which is demonstrated in Figure 34. A comparison of the thin-anode simulation and several geometries (0/0, 20/70, 29/61 and 26/64, where the first number represents the incidence angle α and the second number denotes the take-off angle β), revealed that the thin-anode correction can be most closely simulated with an angle setting of α = 17 and β = 73.

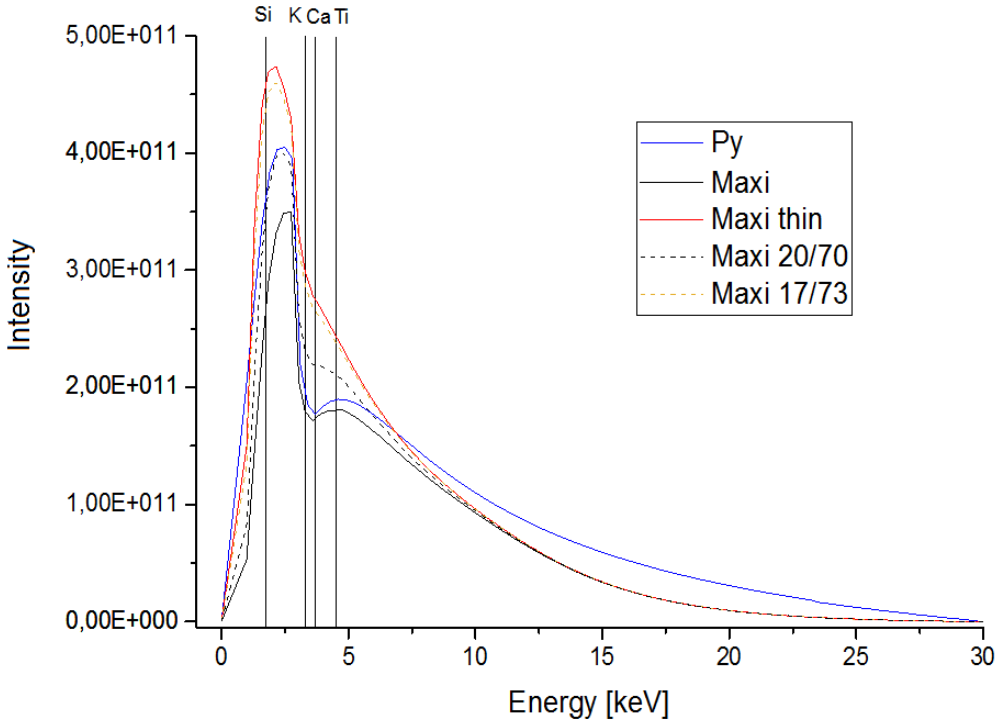

Figure 34: Angular dependence and thin-anode background simulation.

On the one hand, deviations from normal incidence lead to a longer path of the X-ray beam within the anode (see Section 5.13). Therefore, more energy will be dissipated in the anode and more atoms will be influenced by the beam. On the other hand, the beam is weakened by every layer of the anode material (see model in Section 5.7), which explains why the background is so strong in the low-energy region. In thin anodes, the increase in background radiation is owed to the fact that more bremsstrahlung, which is predominantly generated in deep layers of the irradiated specimen, will be able to escape towards the detector.

The above figure also demonstrates that the local minimum of the continuous spectrum at approximately 3 keV, which is owed to the emission of characteristic anode radiation following the absorption of bremsstrahlung at this energy, is much higher for reduced anode thickness. This behavior would explain why elements like K, Ca and Ti cannot be measured correctly with the thick-anode model currently applied.

With regard to the angle of incidence, the 17/73 setting seems to match the thin-anode behavior more closely than the 20/70 setting applicable to the Tracor tube.

13.3 Simulation by BGXRF-Part

BGXRF-Part simulates the tube spectrum on which quantitative analysis is based. The results of the continuum simulation for both wide-field setups are displayed in Figure 35, with the inset displaying the region around the Rh absorption edge (i.e. the energy range from 20 to 30 keV) in greater detail. In the simulation, the tube current was 1 mA and the tube voltage was 40 kV, as these were the settings for most measurements (see Sections 15 and 16).

Since the Tracor signal was much weaker than the count numbers obtained with the transmission tube, it was rescaled for reasons of comparability of the two spectra. On the whole, Figure 35 illustrates why the calculations based on the Tracor spectrometer do not hold for the Maxi setup. Beside the differences in intensity, the second maximum is reached sooner by the Maxi tube at approximately 5.5 keV, while it is at about 8 keV in the Tracor spectrum. The two curves intersect at approximately 6.5 keV, which is near the Kα energy of iron. This is one possible explanation for the fact that elements below iron could not be quantified correctly with the current settings.

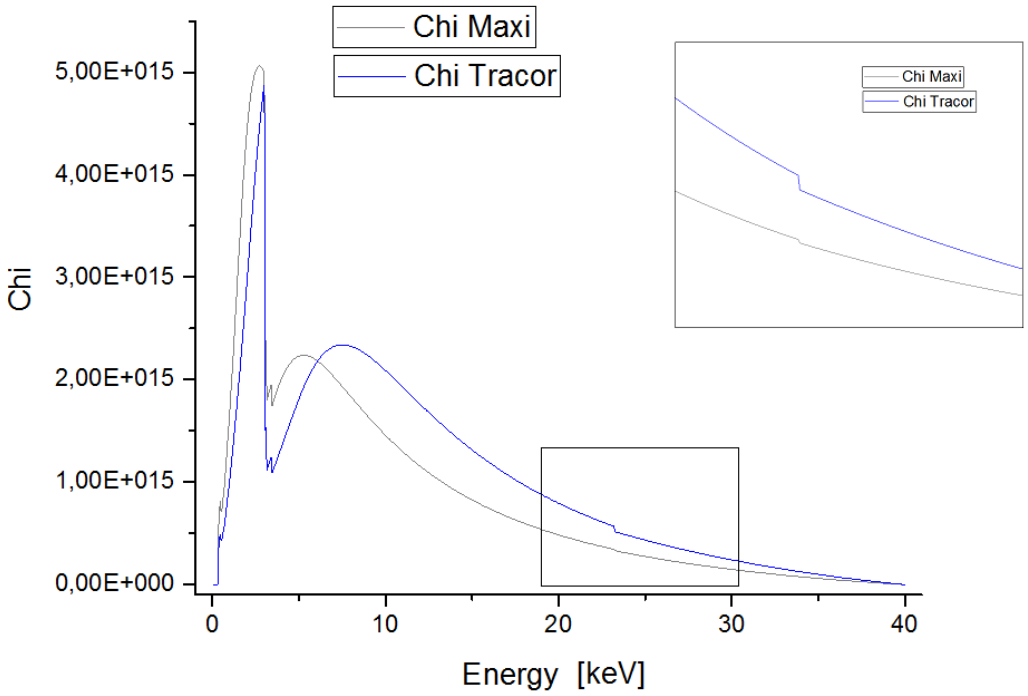

Figure 35: Maxi and Tracor continua as simulated by BGXRF-Part.

Furthermore, the rhodium absorption edge at 23 keV is much more pronounced for the Tracor setup. There are two reasons for this. First, there is the small take-off angle of only 6 degrees, which will lead to stronger absorption. The effect of small take-off angles on the spectral distribution has previously been described by [19], [18] and [52]. In a nutshell, a small take-off angle means that the generated fluorescence has to cover a longer distance within the sample and will hence be more strongly attenuated than for a large take-off angle.

Second, the anode is much thicker for the Tracor setup, causing higher absorption within the anode as described above in the context of generation depth. Low energies may therefore be misrepresented in the simulation of the Maxi tube.

Another factor influencing the absorption edge is the applied tube voltage, which increases not only fluorescence intensity but also absorption and even alters the shape of the tube spectrum.

Yet, above 20 kV, the applied tube voltage shapes the high-energy region of the spectrum only, while the low-energy peaks remain largely unchanged (cf. [3]).

13.4 Simulation by Approximation

To find further differences between the side-window and the transmission tube spectra, the continuous radiation background was fitted with several functions. The fitting parameters were then compared to investigate the cause of the spectral deviations between the two tubes.

13.4.1 Fit Function 1

According to [8], X-ray tube spectra can be approximated by the following function:

$$N(\lambda) \propto (\frac{\lambda}{\lambda_0} - 1)^{q'} \cdot \frac{1}{\lambda^2} \cdot exp(-Q'\mu_{A,\lambda})exp(-\mu_{Be,\lambda}\rho_{Be}d), \tag{39}$$

where λ is the X-ray wavelength,
λ_0 is the minimum wavelength given by the Duane–Hunt Law,
Q' and q' are fitting parameters,
$\mu_{Be,\lambda}$ is the mass attenuation coefficient of beryllium,
$\rho_{Be,\lambda}$ is the mass density of beryllium,
d is the thickness of the beryllium window and
$\mu_{A,\lambda}$ is the mass attenuation coefficient in the target.

Since wavelength and energy are inversely proportional (cf. [8]), this equation can easily be rewritten as follows:

$$N(E) \propto (\frac{E_0}{E} - 1)^q \cdot E^2 \cdot exp(-Q\mu_{A,E})exp(-\mu_{Be,E}\rho_{Be}d), \tag{40}$$

where E is the X-ray energy, Q and q are fitting parameters and
E_0 is the maximum energy (i.e. the tube voltage).

The first term in the above equation is a modification of Kramers' Law; the second term represents anode self-absorption, and the third term describes X-ray absorption by the window.

The mass attenuation coefficients for Rh and Be required for the calculation of the absorption values were taken from the NIST data base (cf. [40], [23]).

The dependence of the fit function on q_{diff} is shown in Figure 36. The peak height increases with increasing values of q, while the high-energy part of the spectrum remains roughly the same.

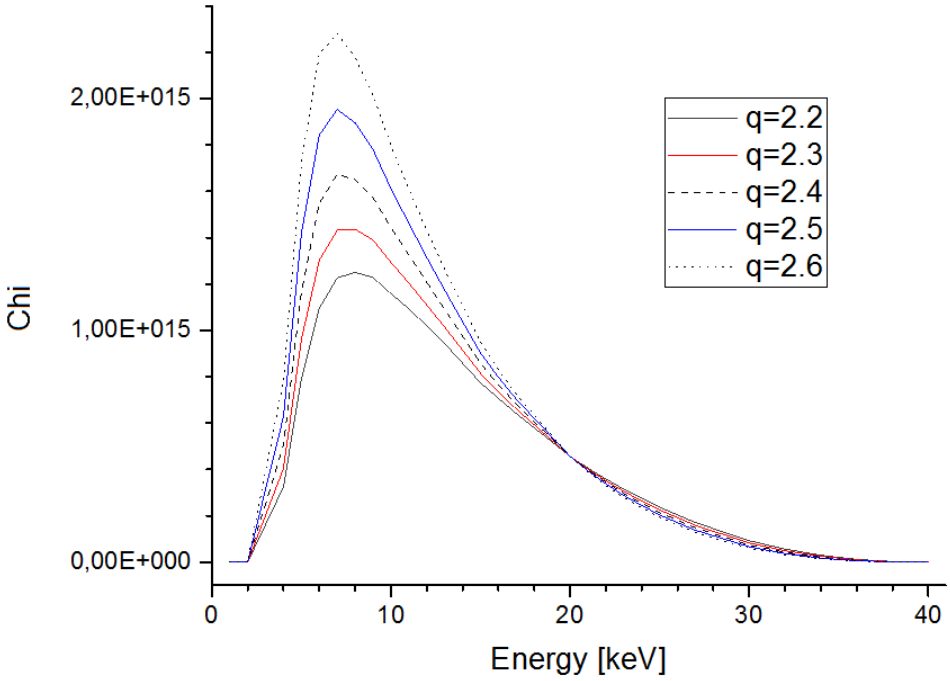

Figure 36: Tracor fit function for various values of q.

Before fitting, the main peak in the low-energy range of the continuum had to be removed as the low-energy region was too complex to be represented by the given function. Therefore, the following analysis is valid for energies above 3 keV only. Furthermore, the function was modified by an additional fit parameter, the multiplicative constant c.

The results of the fitting procedure and the initial parameters for the Tracor and Maxi tubes are listet in Tables 14 and 15, respectively. Figure 37 shows the graphical representation of the Tracor spectrum calculated by BGXRF-Part and the corresponding fit function. The Maxi fit function is displayed in Figure 38.

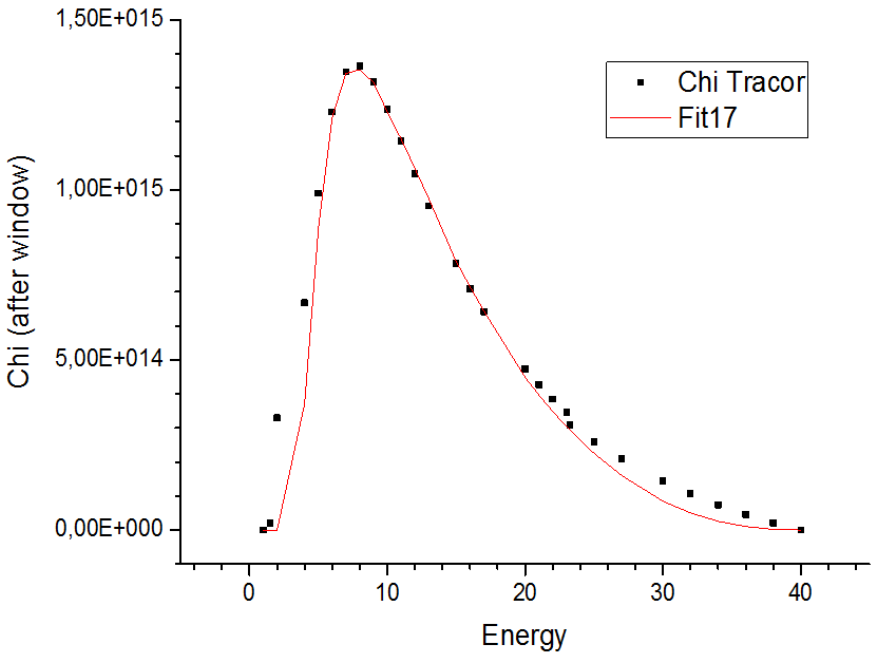

Figure 37: Fit curve (red) and measurement points for the Tracor setup.

	initial	fit
q	1.8	2.27
Q'	5E-7	1E-7
c	1E12	1.2E12

Table 14: Fitting parameters for the Tracor tube.

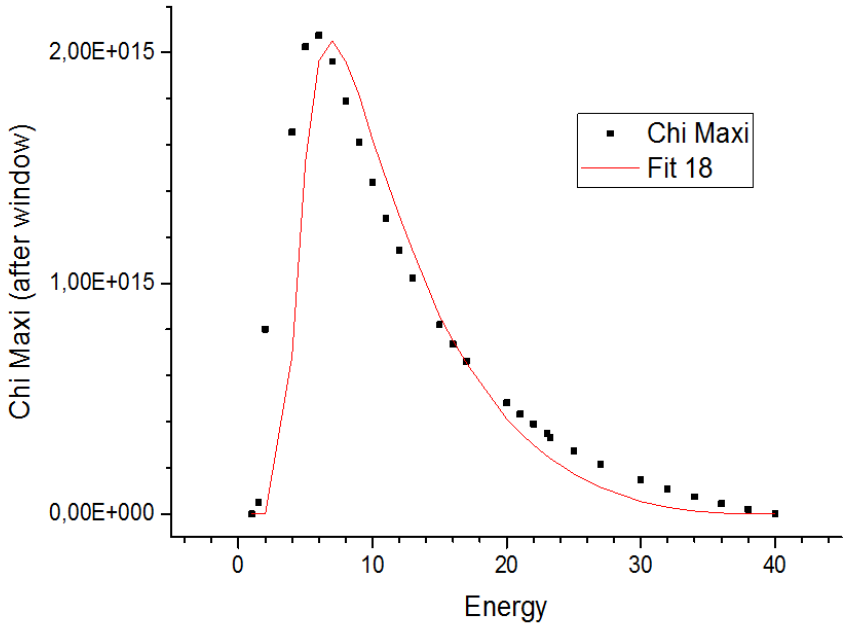

Figure 38: Fit curve (red) and measurement points for the Maxi setup.

	initial	fit
q	2.7	2.6
Q'	5E-4	1E-6
c	9E11	1.1E12

Table 15: Fitting parameters for the Maxi tube.

As the fit for the Maxi tube did not match the simulation as closely as intended, it was repeated to optimize the results. To this aim, the spectrum was split into two energy ranges, namely from 1 keV to 12 keV and from 12 keV to 40 keV. The results are displayed in Figure 39 and Table 16. *high E* and *low E* refer to the fits in the high-energy and low-energy regions.

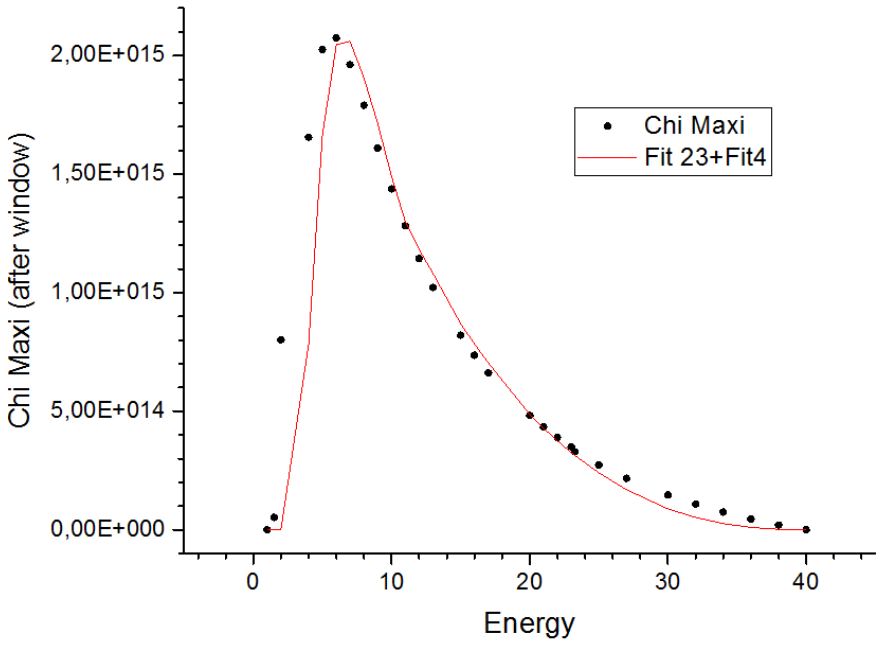

Figure 39: Fit curve (red) and measurement points for the Maxi setup (two fits combined).

	low E initial	low E fit	high E initial	high E fit
q	2.8	2.8	2.6	2.3
Q'	1E-6	5E-9	5E-6	1E-7
c	7E11	8E11	7E11	1.3E12

Table 16: Fitting parameters (combination of two fits) for the Maxi tube.

The above graphs are proof of the validity of the functions as stipulated by Broll (cf. [8]). The resulting fit parameters show that the Maxi and the Tracor tube functions are rather similar for high energies but differ greatly from each other in the low-energy region. "Q" is much higher for the Maxi spectrum, indicating a much steeper curve.

However, it is worth mentioning that the fit functions match the calculated spectrum only in the energy range from 5 to 25 keV. While the Tracor fit function is well-suited to calculate the spectrum for energies below 25 keV, it deviates from the true function above this value. The fit function for the transmission tube deviates from the the simulated spectrum in both the low and the high-energy ranges. In addition, its maximum is shifted as compared to the simulation data.

13.4.2 Fit Function 2

In a next step, the fit function was simplified to reduce computational effort and eliminate the mass attenuation coefficient from the equation, as this parameter is empirically obtained and cannot be an input in the filter function as provided by the BGXRF-Part software. Absorption within the anode material was approximated by a constant. This simplification is valid if one considers that

$$exp(-\alpha x) \approx 1 - \alpha := c', x \longrightarrow 0 \tag{41}$$

Thus, the fit function becomes

$$N(E) \propto c' \cdot (\frac{E_0}{E} - 1)^{q'} \cdot E^2 \cdot exp(-\mu_{Be,E} \cdot \rho_{Be} d). \tag{42}$$

The above approximation can be justified if one considers that for the Maxi setup, the anode is as thin as 1 μm.

Despite the resulting simplification, the second fitting process should corroborate the results of the first fitting process, as the parameters q and c should change only slightly. Again, the fit function for the Maxi setup was not as close to the measured data as for the Tracor setup, which is why the function was split into a low-energy (up to 12 keV) and a high-energy part (from 12 keV onwards). The parameters thereby obtained are presented in Tables 17 and 18.

	initial	fit
q'	2.5	2.3
c'	9E11	1.2E12

Table 17: Fitting parameters for the Tracor tube using Eq. 42.

	low E initial	low E fit	high E initial	high E fit
q'	2.9	2.9	2.3	2.3
c'	7E11	7.12E11	1E12	1.24E12

Table 18: Fitting parameters (combination of two fits) for the Maxi tube using Eq. 42.

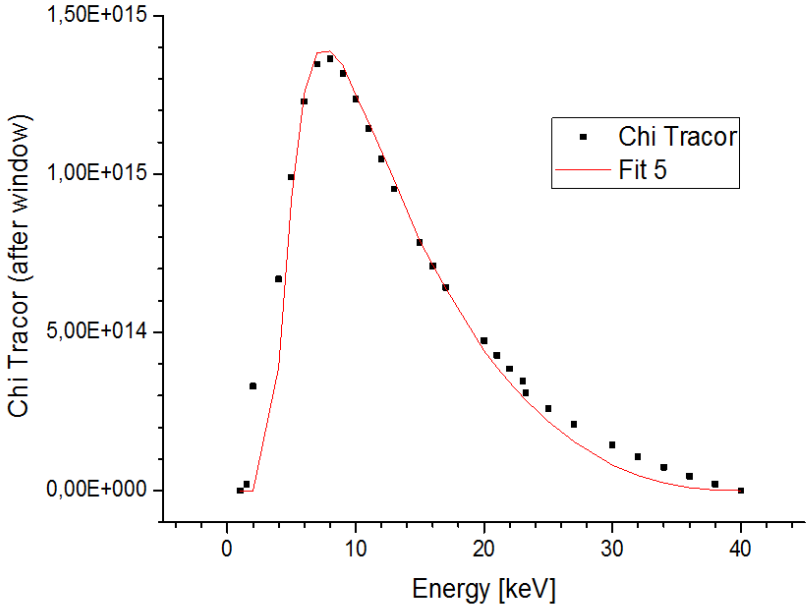

Figure 40: Fit (red) and measurement points for the Tracor setup using Eq. 42.

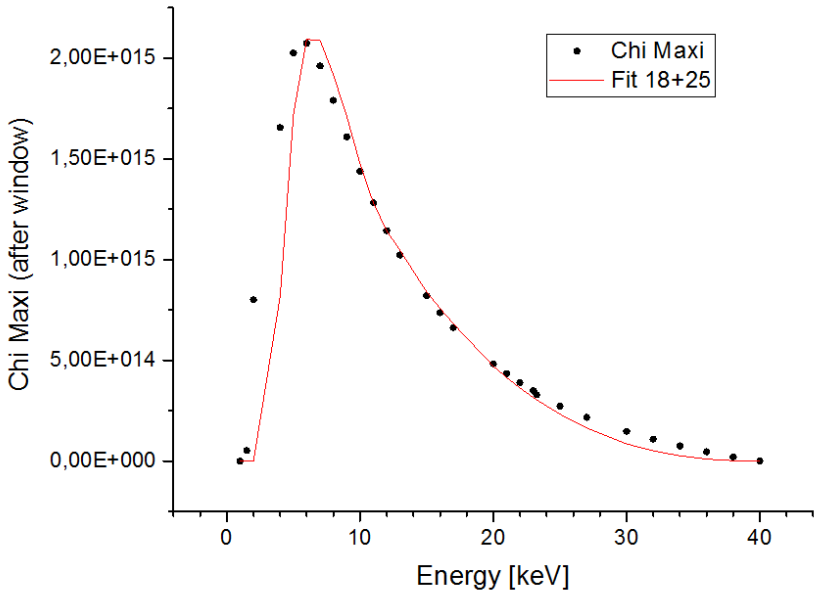

Figure 41: Fit (red) and measured Maxi spectrum using Eq. 42 (two fits combined).

Indeed, fit curves were found that matched the simulation by BGXRF-Part. Unfortunately, the role of absorption by the anode and thus anode thickness cannot be deduced from the above results. For energies above 5 keV, the mere shape of the continuum seems to be largely independent of anode self-absorption.

It stands to reason that the exponential functions in equation 40 can be approximated by simpler energy-dependent exponential or polynomial functions for high energies because they affect mainly the lower part of the spectrum. For energies below 5 keV, a different approach is needed to reflect the thin-anode behavior of the transmission tube.

14 Tube-Spectrum Correction Using Mathematical Functions

Generally speaking, the idea is to apply a corrective function f_{corr} to a spectrum measured with a certain tube to counteract unwanted absorption or enhancement effects and thereby improve quantification. For example, the corrective function can be applied as follows:

$$N_{orig} \cdot f_{corr} = N_{corr} \tag{43}$$

or

$$N_{orig} + f_{corr} = N_{corr}. \tag{44}$$

where N_{orig} is the original spectrum and N_{corr} is the corrected spectrum.

As the filters embedded in BGXRF-Part are limited to multiplicative operations only, the procedure according to Equation 43 will be used exclusively here.

The test functions were fitted to the measured spectra using Origin Pro 2016. This software package employs the Levenberg-Marquardt algorithm, a least-squares algorithm.

As previously found by P. Wobrauschek (cf. [25]), the corrective software BGXRF-Part, which was used in the experiments described herein, works well for the wide-field setup and for elements from Cu onward if a corrective source filter of $y = x^2$ is applied. (Here, the x axis represents the energy scale and the y axis is the intensity.) However, this correction fails for lines below Cu-Kα.

This thesis tries to explain the reason why the correction is applicable in the medium-energy range but fails in other regions of the spectrum. In addition, it aims to find a correction that improves quantification in the lower part of the spectrum.

One has to bear in mind that BGXRF-Part was developed to analyze fluorescence excited by the Tracor setup, which uses a rhodium anode, but whose geometry differs greatly from the Maxi setup. For this reason, deviations caused by the differences in the tube spectra are likely to produce fundamentally different results.

Moreover, the different detectors used to record the spectra might be responsible for the poor quantitative results obtained with the Maxi setup, as detector efficiency has a strong influence on the measured intensity.

Based on these considerations, the following steps were taken to correct the fundamental

parameter model of the Maxi tube.

First, the effect of the E^2 correction was investigated to find out why it improved quantification for energies from 8 to 20 keV.

Second, the measured spectra and the detector-neutral spectra of both wide-field setups were approximated using fit functions to find a suitable mathematical function that can undo the spectral changes introduced by the detector.

Last, the concentration of elements was recalculated using the corrective factors and functions obtained in the aforementioned process steps to find the correction best suitable for quantitative elemental analysis. This also included anode-thickness correction by utilizing higher angles of incidence and detection in the calculation of intensity.

14.1 Effect of E^2 Correction on the Measured Spectrum

Quantitative evaluation had proven more accurate for elements between Cu and Sn if the spectrum was multiplied with E^2 as empirically found by P. Wobrauschek. To find out why, the E^2-corrected spectrum was normalized to the maximum of the detector-neutral spectrum (see Section 12). The original tube spectrum was measured by scattering on a perspex disc with a diameter of 30 mm and a thickness of 3 mm at°an incident angle of 45° and an emission angle of 45°as explained in Section 12.

The results are displayed in Figure 42, in which the black line shows the measured spectrum, the grey line shows the detector-neutral spectrum and the red line shows the spectrum multiplied by E^2.

Figure 42 indicates that the E^2 correction (i.e. multiplication of the measured spectrum by E^2) is well-suited to correct the spectrum from 15 keV onwards. However, it clearly fails to represent the lower part of the spectrum – even worse, it is practically zero for elements below iron. For this reason, elements whose ionization edges are in the lower part of the spectrum (i.e. below approximately 10 keV) cannot be quantified correctly or will not be detected at all if the E^2 correction is used.

On the other hand, the original spectrum overlaps with the detector-neutral spectrum in the region from 3 to 10 keV and will thus provide accurate concentrations for light elements. It is, however, too low for energies between 10 and 15 keV. Therefore, applying the correction to energies above 15 keV would leave these elements underrepresented. Moreover, it would lead to an artificial edge in the spectrum.

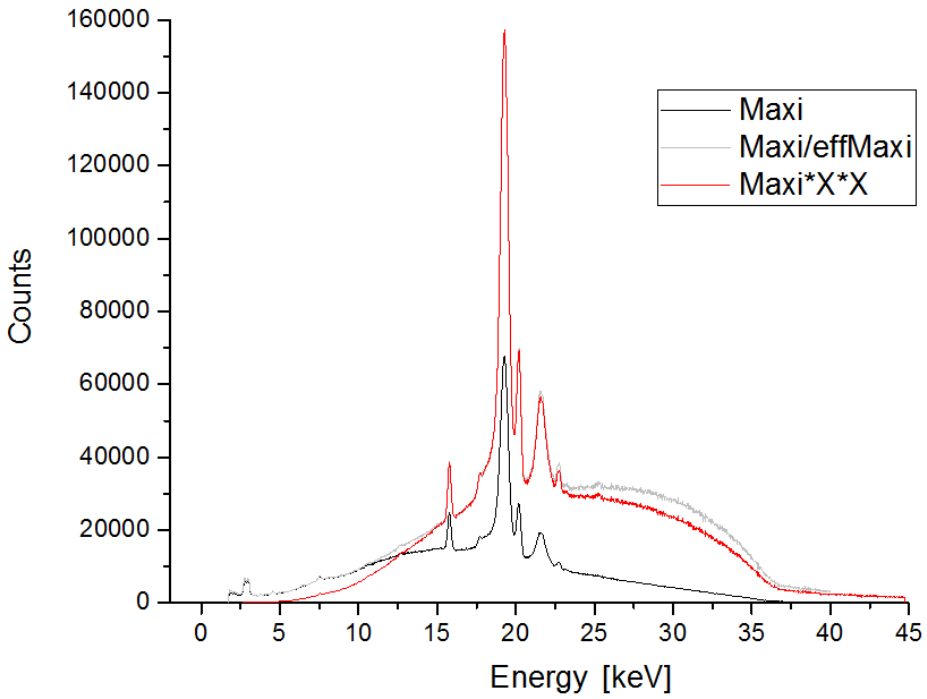

Figure 42: Maxi: measured spectrum (black), detector-neutral spectrum (grey) and normalized corrected spectrum (red).

In conclusion, one needs to find a corrective function that leaves the lowest part of the measured spectrum unchanged, increases the spectrum in the range from 10 keV to 15 keV and neatly fits in with the spectrum as corrected by E^2 from 15 keV onward.

14.2 Correction of BGXRF-Part Simulation

14.2.1 Correction for Detector Efficiency

a) E^2 Correction

In analogy to the previous subsection, the simulation curve by BGXRF-Part was divided by the detector efficiency to obtain the detector-neutral tube spectrum. Then, the E^2 correction was applied to the simulation data to see in how far the corrected spectrum would match the detector-neutral spectrum. The simulation, the corrected simulation and the detector-neutral simulation are displayed in Figure 43.

Again, the E^2 correction seems to work quite well for higher energies. Yet, the effect

on the low-energy spectrum is even more devastating than for the measured spectrum. The two large peaks are eliminated, and instead of reaching its maximum, the curve approaches zero at around 5 keV.

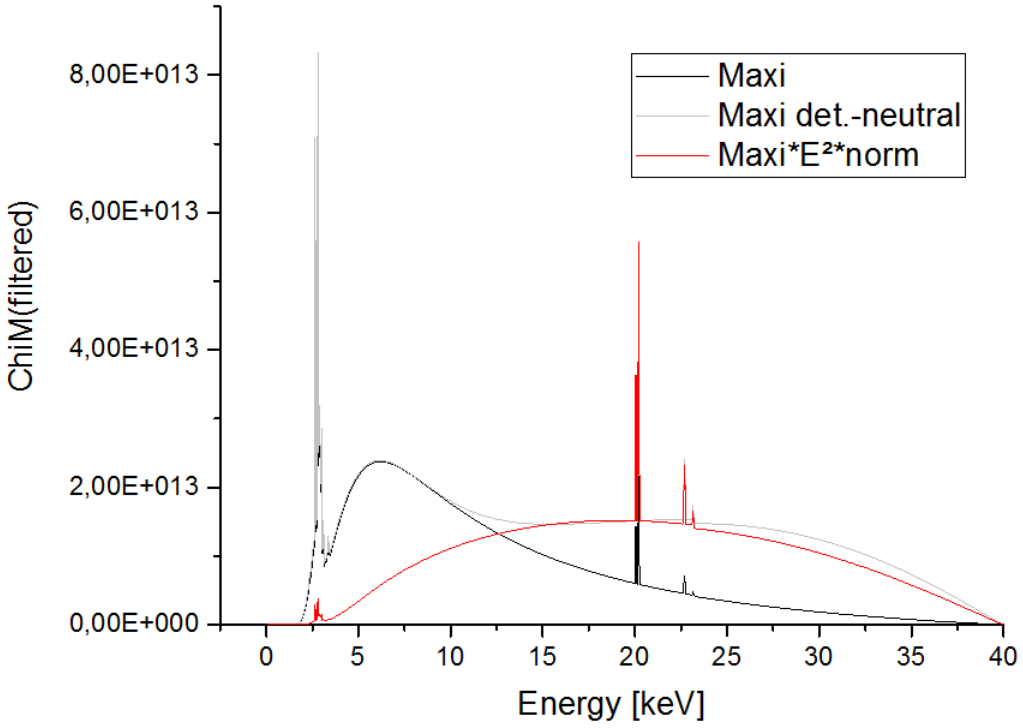

Figure 43: Simulation: uncorrected (black), detector-corrected (grey), E²-corrected (red).

b) Additional Corrections

In another attempt to correct the spectrum, the quotient of the spectral values as simulated by BGXRF-Part with respect to the detector-neutral simulation was examined to find an appropriate function to correct for the detector. As the low-energy region does not need correction and the high-energy region can be corrected by the E^2 function, the idea was to look at the spectrum between 10 and 15 keV only and then combine the original simulation and the two corrections.

The following fit functions were tried and tested:

$$N(E) = c'' \cdot E^2 \cdot exp(p'' \cdot E), \tag{45}$$

$$N(E) = A + B \cdot E + C \cdot E^2, \tag{46}$$

$$N(E) = A + B \cdot E + C \cdot E^2 + D \cdot E^3. \tag{47}$$

Figure 44 demonstrates that both the second-order (Equation 46) and he third-order (Equation 27) polynomials reflect the original data accurately in the medium-energy region. The most suitable linking point was at 9.4 keV, where the jump between the original function and the parabolic fit was smallest.

Table 19 illustrates the coefficients of the parabolic function as given in Equation 46.

A	B	C
2.13938	-0.24139	0.01296

Table 19: Parabolic fit for the medium-energy region.

The corrected spectrum consists of the following parts:

From 0 to 9.35 keV	original function
From 9.4 to 15.4 keV	original function · parabolic fit
From 15.45 keV onward	original function · E² $\cdot norm$

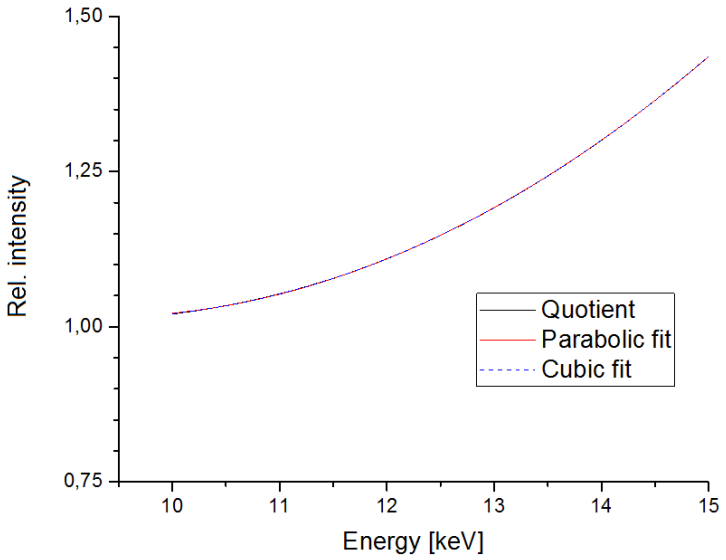

Figure 44: Quotient of uncorrected and detector-neutral simulation (black), cubic fit (red) and parabolic fit (blue).

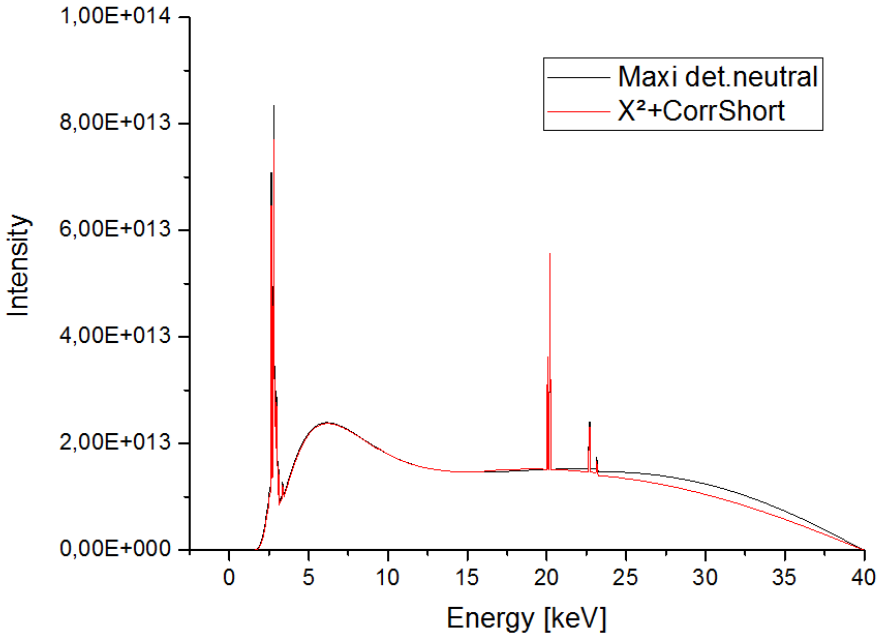

Figure 45: Fit-corrected simulation (red) and detector-neutral simulation (black).

When the two spectral corrections are combined (see Figure 45), the jumps between the polynomial correction and the original function and between the polynomial function and the E^2 correction are negligible. However, the E^2 correction still diverges from the detector-neutral function, and the normalization factor is not ideal because it will change with the tube voltage. To find a better solution and to avoid at least one of the jumps in the first place, an attempt was made to find a function that would cover the entire spectrum at least from 5 keV onward.

c) Polynomial correction

In order to avoid having two jumps as explained above, and to normalize the E^2 function to the maximum of the bremsstrahlung background, polynomial functions were tested for their suitability as corrective functions. A fifth-order polynomial and a cubic function were found to adequately match the detector-neutral function. The two fits and the detector-neutral spectrum are compared in Figure 46. The fit parameters are presented in Tables 20 and 21.

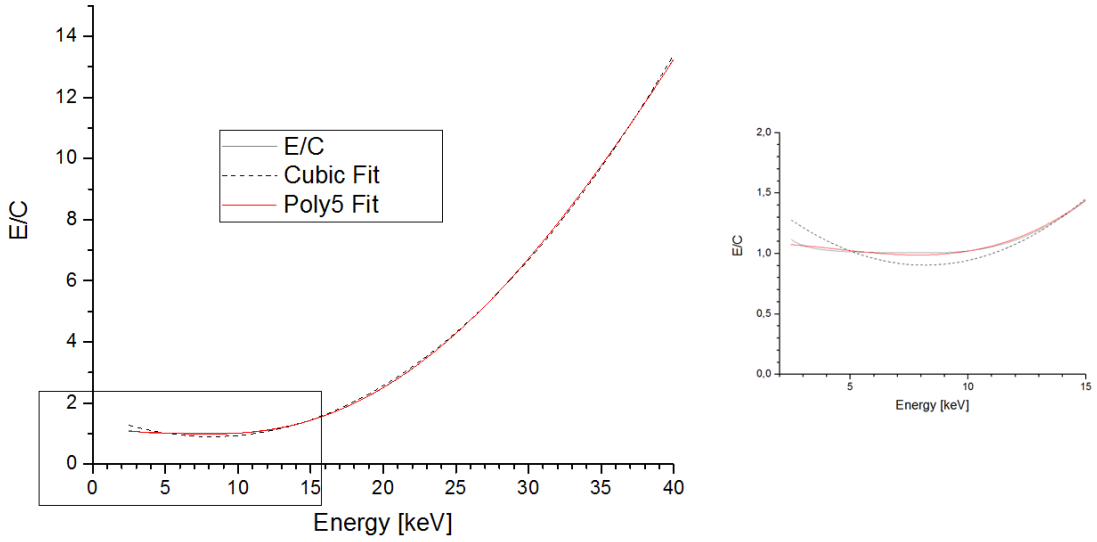

Figure 46: 5th order polynomial fit (red), cubic fit (dashed) and difference between detector-neutral and original simulation (black).

A	B	C	D	E	F
1.06438	0.02461	-0.01098	9.65553E-4	-1.68972E-5	1.00016E-7

Table 20: 5th order polynomial fit.

A	B	C	D
2.05975	-0.24673	0.01387	-1.61207E-5

Table 21: Cubic fit.

While both fits are well-suited to correct the spectrum from 15 keV onward, the cubic fit increases the intensity for lower energies as shown in the inset to Figure 46. As regards quantification, a certain number of measured counts will produce a lower concentration result if the primary spectrum is increased, which is – in this case – an undesired effect. Based on the jump between the corrected and the original spectral area, it was decided to use the 5th-order polynomial function from 3 keV onward. The corrected spectrum, which is presented in Figure 47, therefore consists of the following parts:

From 0 to 3 keV	original function
From 3 keV	original function · polynomial fit

Again, the jump between the two functions is negligible, but now the high-energy region matches the detector-neutral curve, which can barely be distinguished from the corrected spectrum. The low-energy region follows the original data, meaning that the corrective function is approximately 1 in this area.

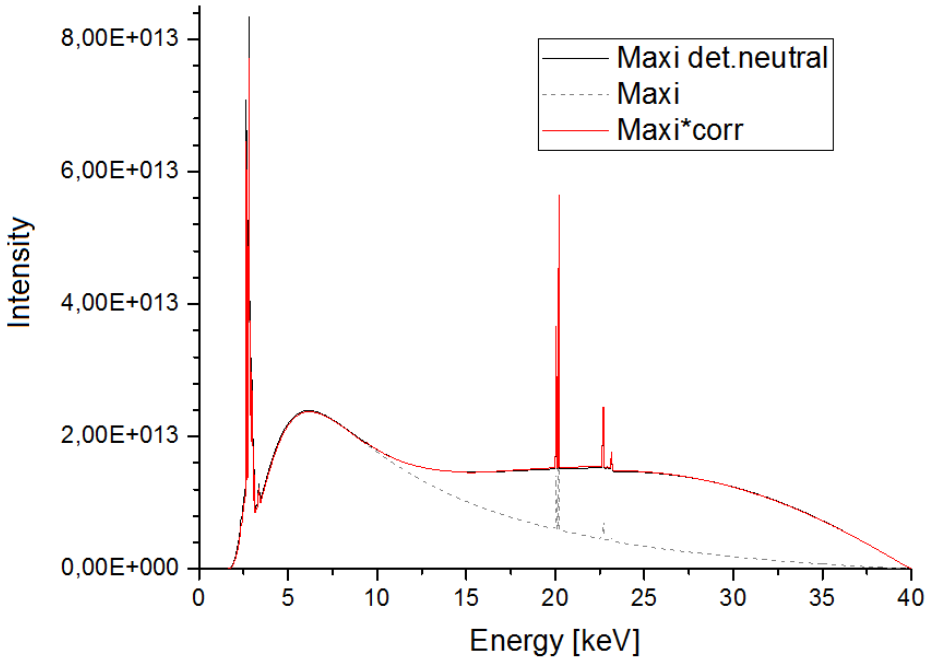

Figure 47: Corrected spectrum (red), detector-neutral simulation (black), uncorrected simulation (dashed grey).

14.2.2 Correction for Anode Thickness

As mentioned before, the anode of the transmission tube has a thickness of only 1 μm and is hence much thinner than the anode employed in the side-window tube. The thin-anode behavior is a plausible reason for poor quantification results and should be compensated for.

Based on the simulation described in Section 13.2, the α and β angles were adjusted to simulate a longer path of the electron beam within the sample and thereby correct for the lower thickness. To find out whether the corrections were accurate, the sample measurements were quantified with BGXRF-Part using the filter function and the angular correction. Indeed, the change in angles yielded slightly better quantitative results, which are presented in the next Section.

15 Measurements Using the Spectral Correction

The samples were re-evaluated using the corrective functions found during the process outlined in the previous section. For quantitative evaluation, the fit as presented on page 69 was used exclusively (original function for low energies; polynomial fit for energies above 3 keV). As the correction is a purely mathematical one, remeasuring the samples was not necessary. In addition, several standards were analyzed to substantiate the effectiveness of the applied corrections and find possible areas in which they required further improvement.

To include the effect of the ultra-thin anode, the α and β angles were first set to 20 and 70° ("angle 1") and then to 17 and 73° ("angle 2"; see Section 13.2, especially Figure 34 on the angle dependence of the tube spectrum). Just as for the confocal measurements, quantitative evaluation was performed in both AXIL and PyMCA for better robustness. The expected and calculated percentages as well as the relative errors are presented in Tables 22 to 25 for the bronzes and in Tables 26 to 53 for the other standards.

15.1 Bronze Samples

Each bronze sample was measured at three different points to yield more robust results. The tube voltage and current were set to 40 kV and 20 μA, respectively. The dead time was between 13.5 and 17.1 % for all measurements, and the duration of measurement was 200 s. In AXIL, the selected background model was 8th order bremsstrahlung, whereas the linear polynomial continuum of 5th order was selected in PyMCA. In all cases, the Cu, Ag and Sn K series were used for quantification. As an example, Figure 48 displays the spectrum of Sample A.

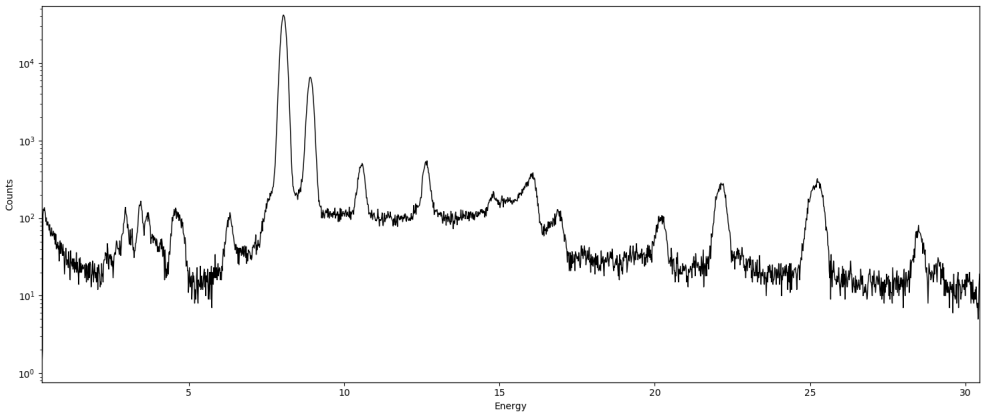

Figure 48: Spectrum of Sample A.

Sections 15.1.1. to 15.1.4 will now present and discuss the results of quantitative analysis.

15.1.1 Sample A

		Angle1				Angle2			
		AXIL		PyMCA		AXIL		PyMCA	
Element	Expected	Mean	E_{rel}	Mean	E_{rel}	Mean	E_{rel}	Mean	E_{rel}
Cu	90	88.09	2	89.36	0.7	88.19	2	89.45	0.6
Ag	2	2.44	22	2.18	9	2.42	21	2.16	8
Sn	4	5.01	25	4.58	15	4.97	24	4.53	13
Pb	4	4.45	11	3.88	3	4.43	11	3.86	4

Table 22: Analysis of sample A with angular correction

According to these data, the best result was achieved with PyMCA and corrective angle 2. All in all, the differences owed to the angle correction are rather weak for sample A, with the results improving slightly if angle 2 is used. When fitting is performed with AXIL, the error is highest for Sn; using PyMCA, the results for both Ag and Pb are slightly off.

15.1.2 Sample B

		Angle1				Angle2			
		AXIL		PyMCA		AXIL		PyMCA	
Element	Expected	Mean	E_{rel}	Mean	E_{rel}	Mean	E_{rel}	Mean	E_{rel}
Cu	84	82.52	2	84.21	0.3	82.66	2	84.33	0.4
Ag	1	1.02	2	0.94	6	1.01	1	0.94	6
Sn	10	11.24	12	10.14	1.5	11.12	11	10.03	0.3
Pb	5	5.23	5	4.72	6	5.21	4	4.69	6

Table 23: Analysis of sample B

The quantitative results for sample B confirm the findings derived from the analysis of sample A. Again, the combination of PyMCA fitting and angle correction 2 provides the most accurate concentration results. In AXIL, the error is largest for Sn, while in PyMCA, the error is highest for Pb.

15.1.3 Sample C

		Angle1				Angle2			
		AXIL		PyMCA		AXIL		PyMCA	
Element	Expected	Mean	E_{rel}	Mean	E_{rel}	Mean	E_{rel}	Mean	E_{rel}
Cu	79.5	78.88	1	80.97	2	79.03	1	81.12	2
Ag	0.5	0.55	10	0.495	1	0.54	8	0.49	2
Sn	8	9.20	15	8.36	4.5	9.10	14	8.27	3
Pb	12	11.37	5	10.18	15	11.32	6	10.13	16

Table 24: Analysis of sample C

The best result for sample C was achieved with AXIL and angular correction 2. As in Sample B, the error is highest for Sn in AXIL and for Pb in PyMCA.

15.1.4 Summary of Results

The above results provide proof of principle that the ultra-thin anode behavior can be simulated – at least for the energy range of bronze metals – by the suggested angular correction. As expected, the values improve for both corrections, although slightly more so when the 17/73 setting is applied. To provide further evidence for this finding, the mean error was calculated for all the samples together. As Table 25 suggests, the error is indeed smaller for the use of angle correction 2.

	Angle 1		Angle 2	
Element	AXIL	PyMCA	AXIL	PyMCA
Cu	2	1	2	1
Ag	11	5	10	5
Sn	17	7	16	5
Pb	7	8	7	9

Table 25: Bronze measurements, mean error.

The fact that the differences in the results are rather weak underlines the assumption that the thin anode mainly affects the low-energy region of the spectrum. Further tests are needed to substantiate the effectiveness of the angular correction for low-energy lines.

A similar conclusion can be derived for the use of PyMCA instead of AXIL. Although PyMCA fitting yielded more accurate concentrations for samples A and B, this was not the case for sample C. Once again, the bronze components cover only a small part of the spectrum, which is why one should not leap to the conclusion that PyMCA is more accurate than AXIL.

15.2 Pure Aluminum

A piece of pure aluminum was irradiated using a tube voltage of 20 kV and a tube current of 20 μA. The measurement time was 200 s. A total of six measurements were made, three thereof in air and three in a helium environment. The dead time was only 1 %.

As aluminum emits radiation at a very low energy which will be absorbed in the air path, a helium flush system was installed before measurement. In BGXRF-Part, this helium path was simulated by a vacuum environment using a mathematical filter. Quantitative analysis was performed with angle setting 2. The background was 8th order bremsstrahlung in AXIL and a linear polynomial continuum of 7th order in PyMCA.

The results (see Tables 26) imply that the aluminum has several impurities of a very low concentration.

Element	Mean AXIL	Mean PyMCA
Al	99.54	99.65
Fe	0.38	0.32
Cu	0.02	0.003
Zn	0.05	0.035

Table 26: Analysis of pure Al with He Flush

15.3 Standard No. 1171

NIST Standard no. 1171 is a steel standard that contains a large variety of metals including silicon. Such low-Z elements can be measured only if the sample area is flushed with helium to avoid absorption by air constituents (see 15.2).

The tube current was set to 40 kV and the current to 20 μA. The duration of measurement was 200 s, with a dead time of 6.8 %.

Three sets of data (Meas1, Meas2, Meas3) were collected to eliminate possible errors and bias. The relative error was then calculated with respect to the mean value. Background fitting was carried out in both AXIL and PyMCA using the 9th-order orthogonal polynomial background and the 7th-order linear polynomial background, respectively. In BGXRF-Part, the helium environment was again approximated by a vacuum environment (see 15.2). The thin anode was simulated by angular correction 2.

The spectrum of standard no. 1171 is displayed in Figure 49.

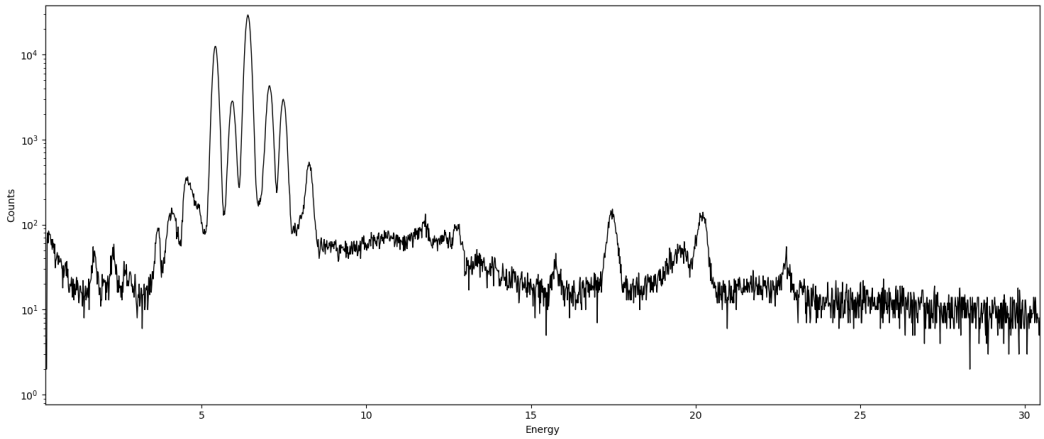

Figure 49: Spectrum of standard no. 1171.

In general, the results are acceptable except for the titanium value. However, if one considers that the sample is primarily composed of iron, the error can be explained by the broad Kα iron escape peak at 4.7 keV, which strongly overlaps with the traces of Ti in the sample (Ti Kα is at 4.5 keV). The Fe escape peak also affects the quantification of Mn, whose Kα peak is on the low-energy side of the Fe escape peak.

Furthermore, it is important to note that Standard No. 1171 contains traces of cobalt (Co) and carbon (C). However, the large Fe peak overlaps with the Co K-α peak at 6.9 keV, preventing the detection of Co in the sample. Due to strong absorption of low-energy lines by the beryllium window (see Section 3.8), carbon cannot be detected either.

Both AXIL and PyMCA could not fully split the trace elements from the large iron escape peak. While AXIL could not correctly determine the concentration of Ti, PyMCA failed to represent the Mn peak.

		AXIL		PyMCA	
Element	Expected	Mean	E_{rel}	Mean	E_{rel}
Si	0.54	0.42	22	0.43	20
Ti	0.35	0.82	134	0.56	60
Cr	17.5	19.51	11	17.44	0.3
Mn	1.81	2.43	34	4.21	132
Ni	11.18	10.57	6	9.18	18
Mo	0.17	0.16	6	0.14	18

Table 27: Analysis of Standard No. 1171

15.4 Standard No. 621

This glass standard contains a large number of light trace elements and was therefore irradiated for a longer duration of 500 s. Again, measurements were performed in helium to better detect low-energy lines. The tube voltage and current settings were 40 kV and 20 μA, respectively. The dead time was 3.9 %. The spectrum of standard no. 621 is illustrated in Figure 50. Since Na2O, Al2O3 and MgO could not be detected, they were

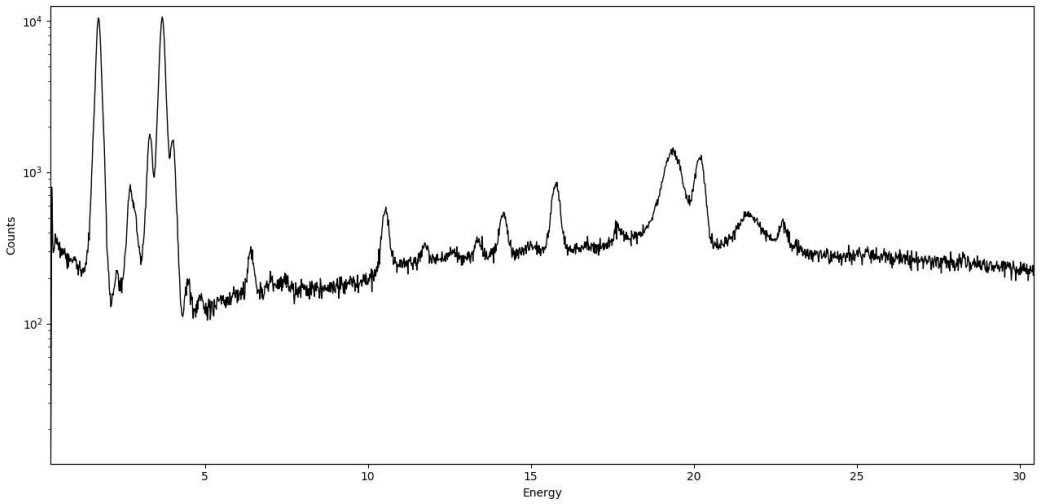

Figure 50: Spectrum of standard no. 621.

manually added to the list of elements in BGXRF-Part. By the same token, Zr was added, as this is the collimator material and will interfere with the Zr contained in the sample.

For background fitting, orthogonal polynomials of 5th order were selected. Like for the previous samples, three different sites were exposed to X-rays for reasons of statistical robustness. Although the Kα lines of Ca (at 3.69 keV), Ti (at 4.51 keV) and K (at 3.31 keV) are fairly close, the resolution of the detector, which is approximately 170 eV, should be sufficient to distinguish between these elements.

There is, however, a strong overlap of the Ti K lines with barium, which is detected by its L lines, leading to severe underrepresentation of Ba. In addition, the potassium Kα line at 3.3 keV is very close to the sum peak of the intense silicon Kα line, leading to overestimation of potassium.

To assess whether the thin-anode simulation holds true for low energies, too, both angular corrections (20/70 and 17/73) were applied. The calculated concentrations are presented in Table 28.

		Angle 1		Angle 2		Angle 2, He		Necker	
Element	Expected	Mean	E_{rel}	Mean	E_{rel}	Mean	E_{rel}	Mean	E_{rel}
Na2O	12.74	-	-	-	-	-	-	-	-
Al2O3	2.76	-	-	-	-	-	-	-	-
MgO	0.27	-	-	-	-	-	-	-	-
Zr	0.007	-	-	-	-	-	-	-	-
SiO2	71.13	59.73	16	60.61	15	68.07	4	67.28	5
K2O	2.01	3.94	96	3.84	91	2.75	38	3.42	41
SO3	0.13	0.093	28	0.094	28	0.12	8	0.11	15
CaO	10.71	20.20	89	19.44	82	13.15	23	20.59	92
TiO2	0.014	0.057	307	0.053	279	0.031	121	-	-
Fe2O3	0.04	0.08	100	0.072	80	0.042	5	0.15	275
CuO	0.003	0.002	33	0.002	33	0.001	67	-	-
As2O3	0.03	0.039	30	0.034	13	0.023	23	-	-
BaO	0.12	0.067	44	0.062	48	0.04	67	0.22	83

Table 28: Analysis of Standard no. 621 using AXIL

As expected, angle 2 yields better results in the analysis of the glass standard, because the X-ray lines of its constituents mostly lie in the low-energy range, which is strongly affected by the incidence angle of the tube beam.

Aside from the overlaps of Ba and Ti as well as K and the Si sum peak (see above), the values for K2O, CaO and Fe2O3 were still too high and required further investigation.

The answer to the problem lies in Figure 51, which shows that the vacuum approximation is incorrect. The blue line represents the tube spectrum in a helium atmosphere, while the black line is the tube spectrum in vacuum. The low-energy range is particularly affected by the He filter, because the characteristic L lines of the rhodium anode are diminished considerably and are available for excitation to a much lesser extent. For this reason, absorption in helium was included into the simulation.

Indeed, correcting for helium did the trick, and the error of the main elements was acceptable, especially in comparison to the results obtained by Necker (cf. [39]) in a previous experiment with the Tracor spectrace 5000. The large error for CuO can be explained by its low concentration, which will introduce a high statistical error.

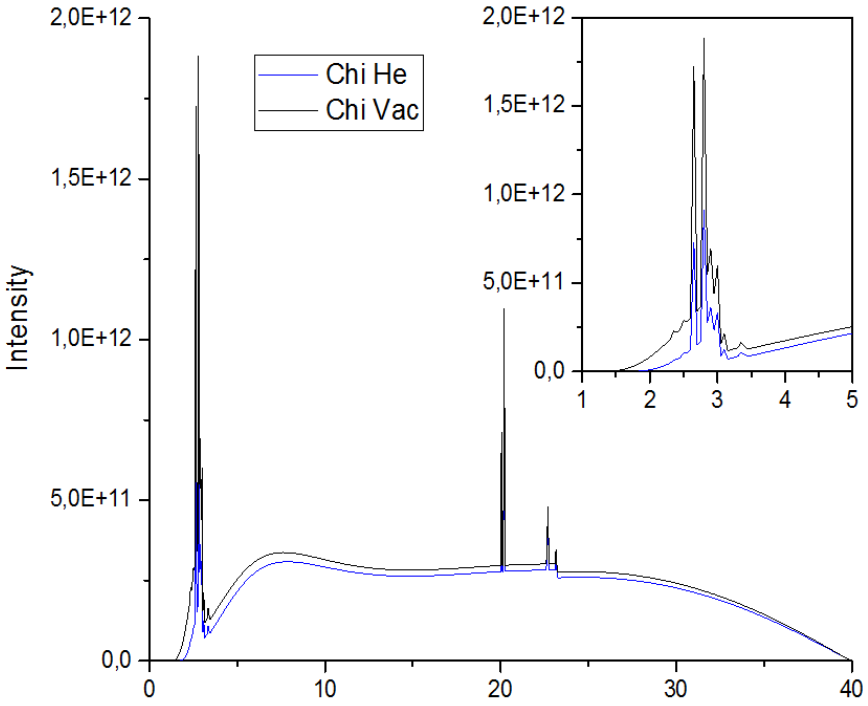

Figure 51: Simulated spectrum with and without the He filter.

15.5 10-Eurocent Coin

The 10-Eurocent coin has a well-known composition and is hence equivalent to an international measurement standard. The measurements had a duration of 200 s and were performed in a helium environment. The tube voltage and current settings were 40 kV and 20 μA, respectively. The dead time was between 18.7 and 19.6 %. Again, the coin was measured at three different sites to make sure that the obtained concentrations were not random.

The thin-anode behavior was once more simulated by angle setting 2. Like for Standard no. 621, the helium environment was first approximated by the vacuum filter (see Table 29) and then compared to the helium filter (see Table 30) to substantiate the validity of the helium correction. Quantitative analysis was based on the K lines of the constituents. The spectrum of the coin is depicted in Figure 52.

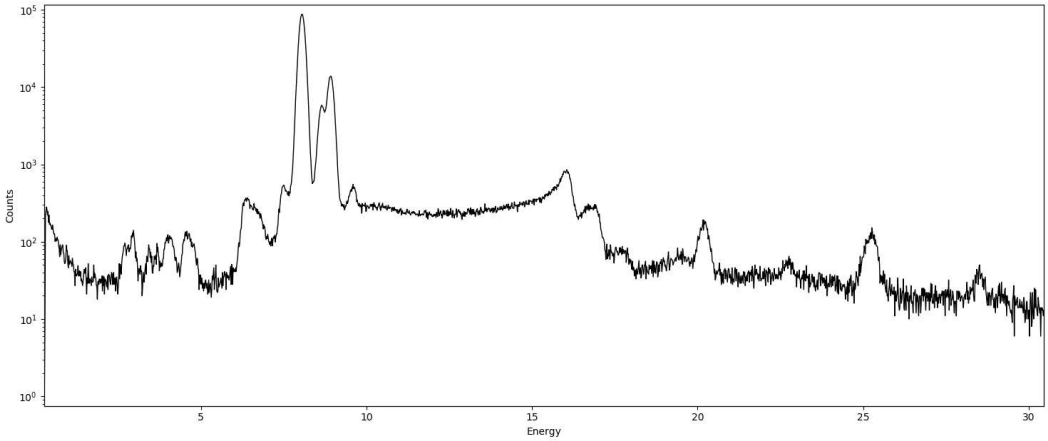

Figure 52: Spectrum of the 10-Eurocent coin.

The data below are proof of the validity of the He correction, which yields excellent results in combination with AXIL. As regards the incorrect quantification of Sn in the data obtained with PyMCA, the error is caused by the poor fit, which overestimates Sn and underestimates Al and Cu. The fit could not be improved in several fitting attempts. Therefore, Figures 53 and 54 show the results for AXIL only.

		AXIL		PyMCA	
Element	Expected	Mean	E_{rel}	Mean	E_{rel}
Al	5	2.50	50	2.01	60
Cu	89	91.48	3	89.32	0.4
Zn	5	4.25	15	3.95	21
Sn	1	1.77	77	4.72	372

Table 29: Analysis of 10 €ct coin using the vacuum approximation

		AXIL		PyMCA	
Element	Expected	Mean	E_{rel}	Mean	E_{rel}
Al	5	5.05	1	3.75	25
Cu	89	89.7	1	87.54	2
Zn	5	4.35	13	3.87	23
Sn	1	0.93	7	4.84	384

Table 30: Analysis of 10 €ct coin using the He correction

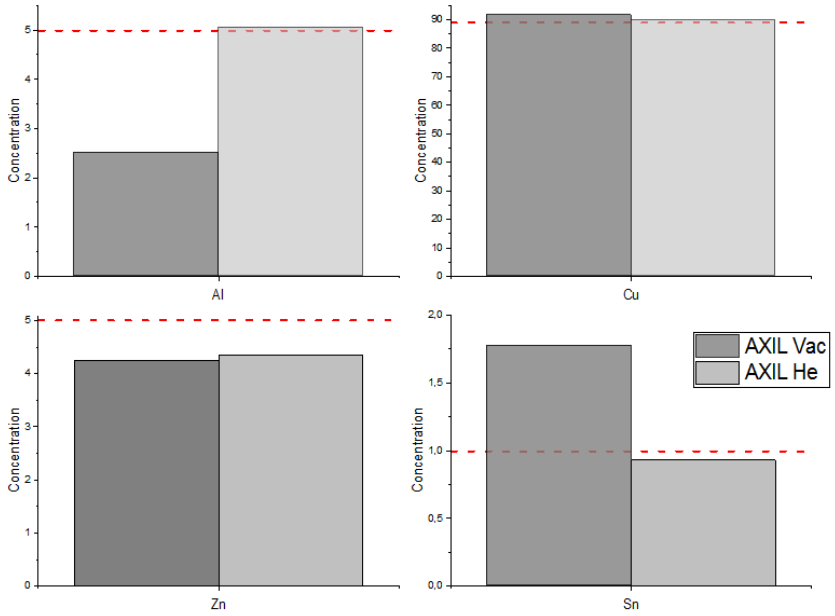

Figure 53: Comparison of vacuum and He correction for 10-€ct coin, fitting in AXIL.

In Figure 53, the dark grey columns represent the vacuum filter correction, the light grey columns the helium filter correction. The red dashed line indicates the expected value. Figure 54 presents the relative errors for the vacuum and helium corrections. For the purpose of illustration, the helium correction data were slightly shifted to the left.

As evident from the graphical representation of the data, the error is much higher for low concentrations, which illustrates the importance of statistical fluctuations. Moreover, the inability to find a fit function in PyMCA demonstrates the sensitivity of the quantification process to the fitting result and therefore to both human error and the underlying software.

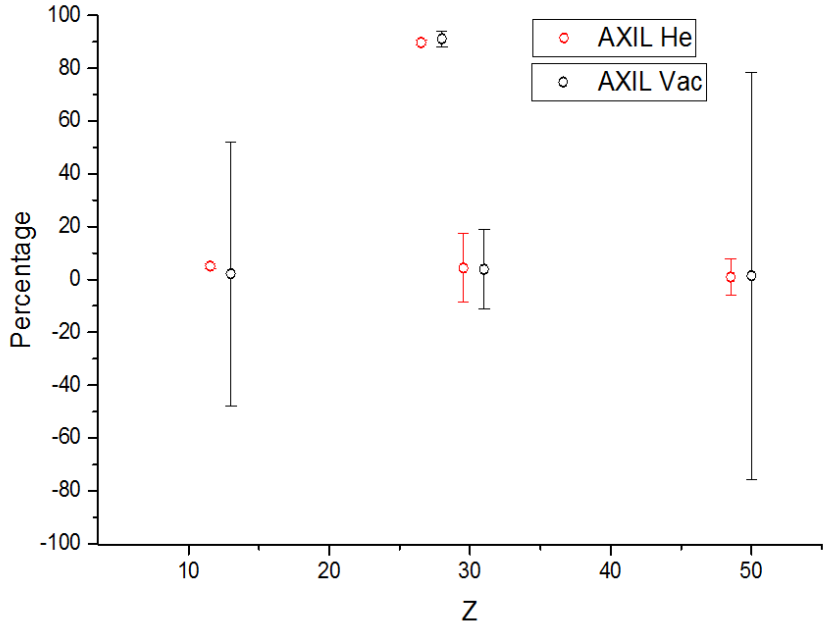

Figure 54: Comparison of vacuum and helium correction errors, fitting in AXIL.

16 Measurements Using the Side-Window Tube

The Tracor Spectrace 5000 is an old but robust system. Like the Maxi transmission-tube setup, it has a rhodium tube, whose anode is, however, much thicker than in the Maxi tube. In order to be able to assess the accuracy of the quantitative evaluation carried out using the corrected Maxi spectrum, several sample spectra were recorded with the Tracor setup and evaluated with BGXRF-Part after inputting the well-tested Tracor-specific parameters.

16.1 Bronze Samples

The bronze samples were measured with the same settings as for the Maxi setup. Hence, the tube voltage and current were set to 40 kV and 20 μA, respectively. By the same token, the 1 mm collimator was inserted. The dead time was approximately 30 %; nevertheless, resolution was acceptable. Although the Tracor Spectrace is equipped with its own analysis software, AXIL and PyMCA were used to ensure comparability to the Maxi measurements.

Due to the fact that the Tracor machine measures each (round) sample at its center only, the same region had to be measured several times. For this reason, fluctuations should be of a purely statistical nature and should be very weak given that sample inhomogeneity does not play a role from a statistical point of view if the measurement site remains the same. An exemplary spectrum (Sample C) recorded with the wide-field setup is shown in Figure 55.

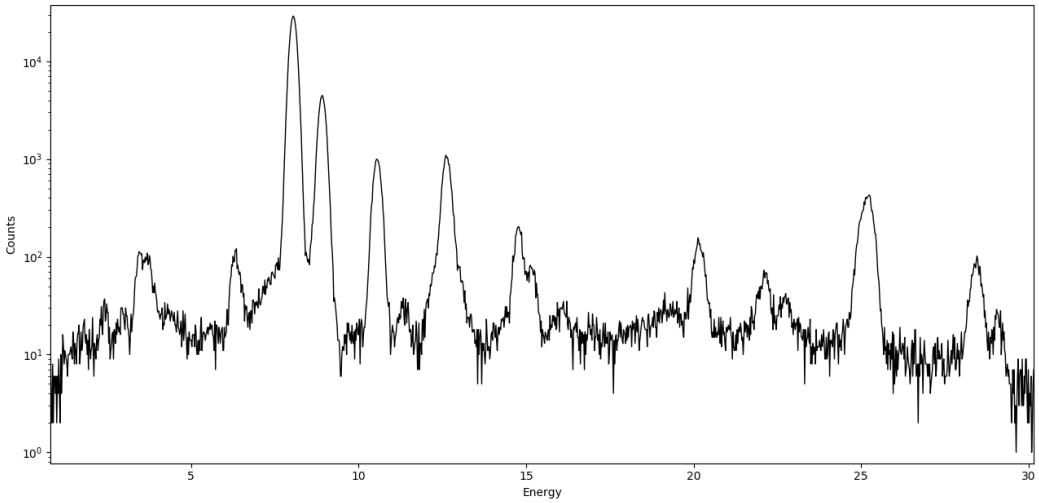

Figure 55: Spectrum of Sample C.

For fitting in AXIL, orthogonal polynomials of 7th order were selected; for PyMCA, linear polynomials of 7th order were used. The evaluation was based on K lines except for Pb, where only the L lines were available (Pb Kα = 72.8 keV cannot be excited with a tube voltage of 40 kV). The calcuated concentrations and relative errors are presented below.

		AXIL		PyMCA	
Element	Expected	Mean	E_{rel}	Mean	E_{rel}
Cu	90	86.48	4	87.05	3
Ag	2	2.78	39	2.54	27
Sn	4	5.71	43	6.12	53
Pb	4	4.86	21.5	4.29	7

Table 31: Analysis of sample A

		AXIL		PyMCA	
Element	Expected	Mean	E_{rel}	Mean	E_{rel}
Cu	84	78.74	6	80.61	4
Ag	1	1.25	25	1.2	20
Sn	10	14.13	41	12.88	29
Pb	5	5.88	18	5.31	6

Table 32: Analysis of sample B

		AXIL		PyMCA	
Element	Expected	Mean	E_{rel}	Mean	E_{rel}
Cu	79.5	74.76	6	77.27	3
Ag	0.5	0.61	22	0.54	8
Sn	8	11.00	38	9.85	23
Pb	12	13.64	14	12.33	3

Table 33: Analysis of sample C

PyMCA improves all results except for the Sn value for sample A. Yet, conclusions can be drawn only for bronzes. Whether or not PyMCA evaluation will improve the results in other regions of the spectrum cannot be predicted from these data.

17 Comparison of Wide-Field-Setup Measurements

The analyses of the Tracor and Maxi measurements of the three bronzes A, B and C will now be compared to confirm the accuracy and validity of the corrections applied to the Maxi spectrum. Each of the below Figures is a graphical representation of the cumulative results for one of the samples.

Figures 57, 59 and 61 describe the concentrations for every constituent individually. The black columns give the expected elemental concentration, while the grey columns show the corresponding result obtained with the Maxi setup and either the AXIL (dark grey) or the PyMCA (light grey) software. By the same token, the concentrations measured using the Tracor spectrometer are represented by the striped and white columns.

In contrast thereto, Figures 56, 58 and 60 compare the relative errors resulting from measurement with the Maxi and Tracor tubes and also provide some insight into the reliability of the fitting software. The x-axis displays the atomic number of the element (29 for Cu, 47 for Sn, 40 for Ag and 82 for Pb) in question; the red dots and error bars represent the PyMCA results, whereas the black data points and lines reflect the findings obtained with AXIL. For convenience, the PyMCA data were slightly shifted to the left.

17.1 Sample A

Figures 56 and 57 summarize the quantitative evaluation for the Maxi and Tracor setups. For copper, both the Maxi and the Tracor values are lower than the nominal value, whereas all measured concentrations are higher for silver, tin and lead. Overall, the Maxi analysis matches the expected results more closely, i.e. the error is much higher for the Tracor measurements. Interestingly, analysis with PyMCA is more accurate for all measurements except for the Tracor Sn value.

One can also observe that the error is generally lower for the element with the highest concentration, which can easily be explained by the fact that counting statistics approach the true value for high count numbers.

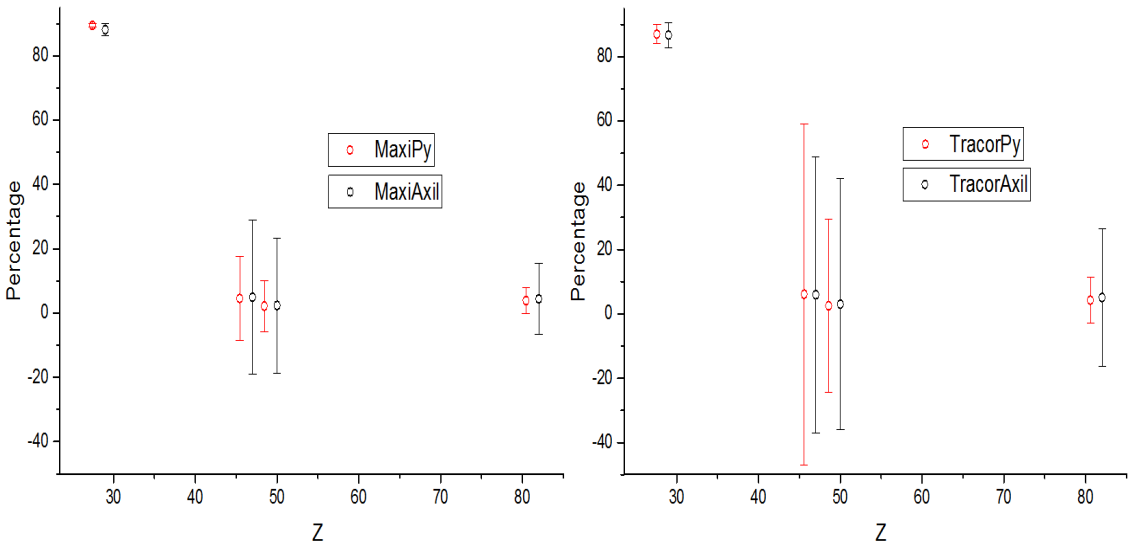

Figure 56: Sample A: comparison of errors.

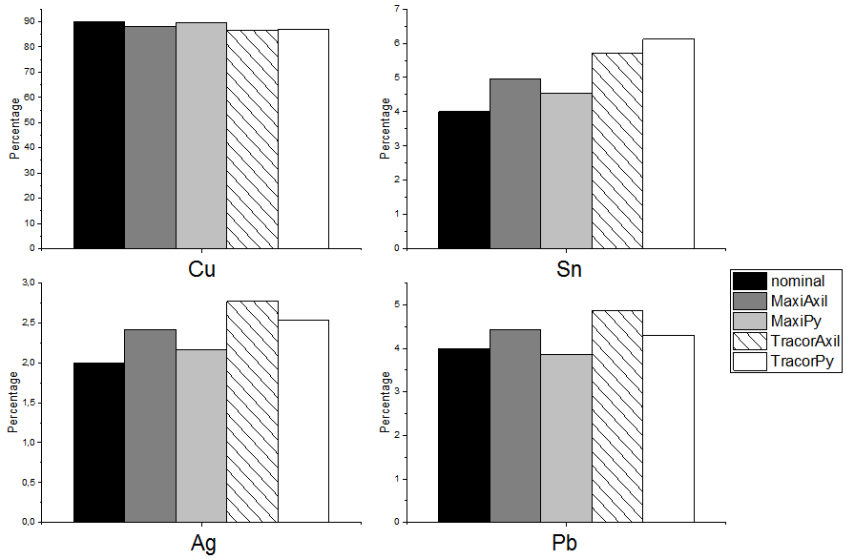

Figure 57: Sample A: comparison of quantitative analysis results.

17.2 Sample B

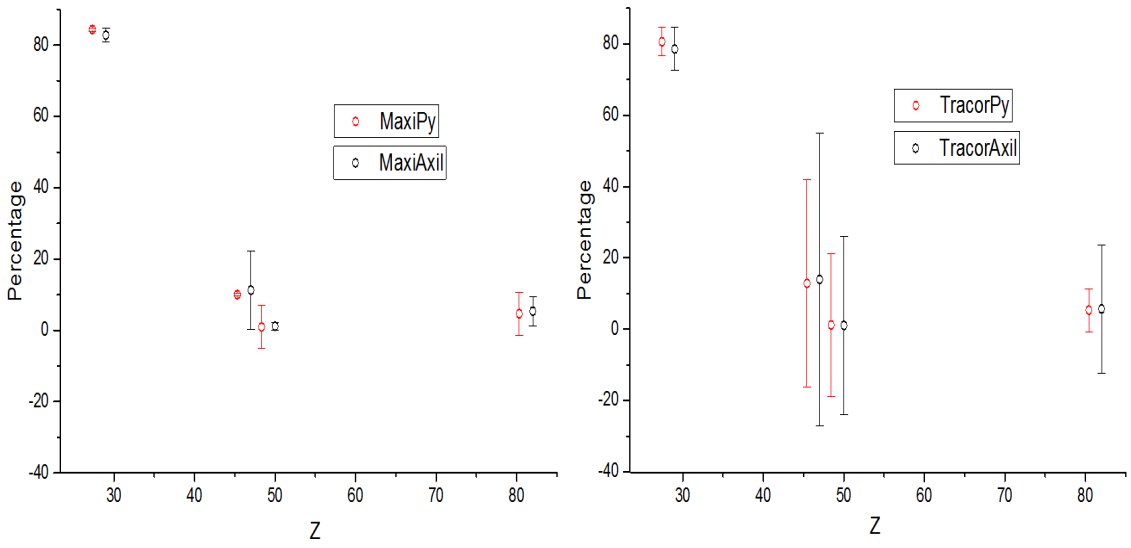

Figure 58: Sample B: comparison of errors.

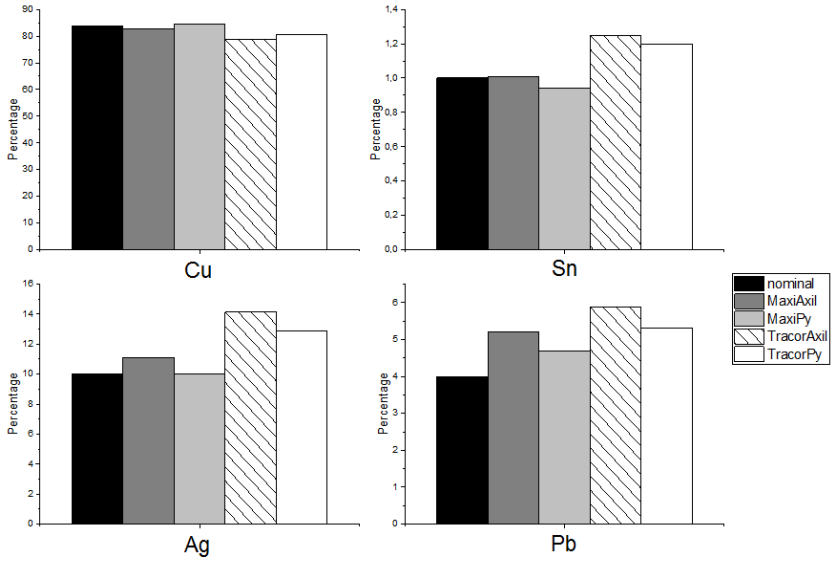

Figure 59: Sample B: comparison of quantitative analysis results.

Like in Sample A, the Maxi results are more accurate than the data recorded with the Tracor setup. The PyMCA data are more accurate for all data measured with the Tracor spectrometer, but not necessarily for quantification with Maxi. The general tendency of the Cu concentration being too low and the other concentrations being too high is also true for Sample B, and the Cu value, which is largest, is the most accurate for both setups.

17.3 Sample C

Again, analysis with PyMCA yielded more accurate values for the Tracor setup, and the error of the Maxi results is lower than the error of the Tracor results. Although the Maxi copper value obtained through PyMCA fitting is higher than the expected value, the general trend towards underestimation of Cu and overestimation of Sn, Ag and Pb can be observed.

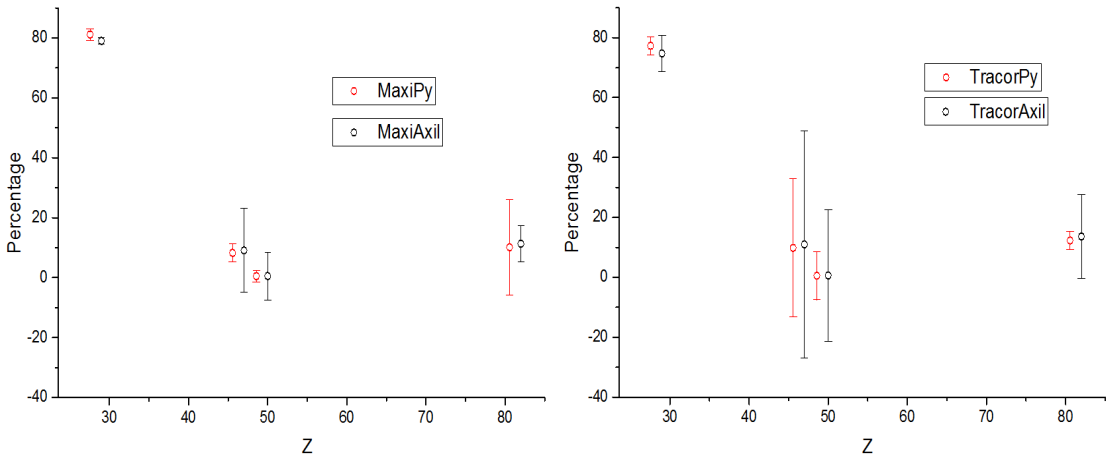

Figure 60: Sample C: comparison of errors.

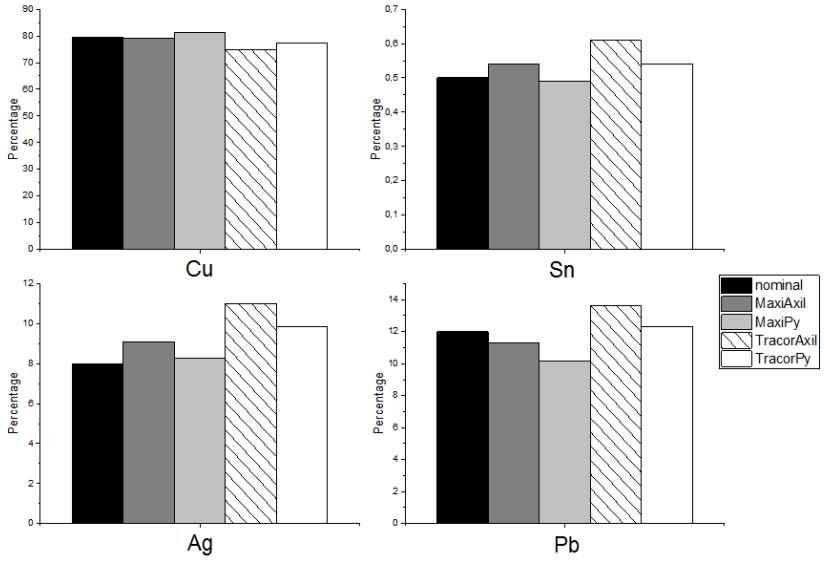

Figure 61: Sample C: comparison of quantitative analysis results.

17.4 Summary of Results

On the whole, the results of both setups correspond to the expected values. The corrected Maxi spectrum works well at least for the applied settings and even yielded more accurate results than the Tracor spectrometer for the given samples. Moreover, the results are more accurate when PyMCA is employed for spectrum fitting as evident from the mean relative error for all samples together, which is presented in Table 34.

	E_{rel} Maxi		E_{rel} Tracor	
Element	AXIL	PyMCA	AXIL	PyMCA
Cu	2	1	5	3
Ag	10	5	29	18
Sn	16	5	41	35
Pb	7	9	18	5

Table 34: Mean relative error of bronze samples

The reason for the inaccuracy observed for the Tracor setup could be that BGXRF-Part analysis was optimized for 45 kV and may therefore be slightly off at 40 kV. Another source of error lies in the fact that although three measurements were taken, the measurement site did not change. Hence, concentration variations will not level out. For the Tracor spectrometer, it is recommendable to use PyMCA to improve quantification.

18 Conclusions and Outlook

18.1 Conclusions

Side-window tubes have been extensively studied for their application in EDXRF, whereas research and literature on transmission tubes are rather scarce. For this reason, the present thesis provides important insights into the spectral characteristics of this tube type.

This thesis has achieved the following research objectives: to analyze possible reasons for the incorrect calculation of elemental concentrations measured with a rhodium-anode transmission tube; to find a corrective function to better reflect its spectral distribution; to test the corrected spectrum by means of reference standard materials; to extend the experimental setup in such a way as to correctly quantify light elements; and to compare two software packages for data evaluation.

The first step consisted in identifying the parameters that were responsible for the deviations of quantitative results obtained with the transmission tube from known concentrations. After ruling out the collimator and incorrect geometrical input parameters as possible causes of the problem, several sample spectra were recorded with the setup under test. The quantitative results were then compared to the concentrations measured with a monochromatic molybdenum beam.

The data obtained from the monochromatic confocal setup were inconclusive due to high relative errors (up to 45 or 98 percent depending on the software utilized). Two main reasons come to mind that may have caused these results: first, the air path may have prevented the correct detection of low-Z elements, and second, the capillary optics may have cut off part of the spectrum.

The next step was to compare the primary spectrum of the transmission tube to that of a reference side-window tube. The most critical parameter turned out to be detector efficiency. While the detector of the side-window setup has only little influence on the shape and intensity of the spectrum, the transmission-tube detector weakens the signal in the high-energy range, leading to drastic changes in the spectrum.

Subsequently, several simulations were carried out to better understand the behavior of the transmission anode. It was found that the maximum depth of fluorescence generation in rhodium is much larger than the thickness of the thin anode, implying reduced anode self-absorption. For this reason, the low-energy continuum is much higher for thin anodes as compared to thick anodes. This was corroborated by an experiment in which an increase in anode thickness was simulated by mathematically altering the electron inci-

dence angle, which only resulted in minor changes to the calculated metal concentrations in the medium to high spectral regions.

The above findings were exploited to determine a corrective function that would eliminate the detrimental effect of the detector and better reflect the thin-anode behavior of the test setup. Reduced detector efficiency was corrected by a polynomial function calculated by a least-squares fitting algorithm, whereas the thin-anode behavior was simulated by the above-mentioned angle correction. The corrections were then scrutinized for their validity by extensive experimental analysis. The tested specimen were bronzes of varying composition, a steel standard, a 10-Eurocent coin and a glass standard.

Background fitting was performed with two software packages, AXIL and PyMCA, to determine which program was better suited for quantification of the tested samples and to avoid fitting errors.

The corrected transmission-tube spectrum provided excellent quantitative results. For the bronze standards, the transmission tube even yielded more accurate results than the well-established side-window spectrometer, with measurement errors of 2 to 16 % for fitting with AXIL and 1 to 9 % for PyMCA as compared to the side-window tube results of 5 to 41 % for AXIL and 3 to 35 % for analysis with PyMCA. These data also imply that PyMCA may be better suited for the bronze energy range than AXIL.

In search of an explanation for the high error rate observed for the side-window setup, one should know that analysis was optimized for a tube voltage of 45 kV and may therefore be slightly off at 40 kV. Another source of error lies in the fact that although three measurements were taken, the measurement site did not change. Hence, local concentration variations will be directly reflected in the calculated concentrations.

As a last step, a helium flush system was installed before the spectra of the steel standard, the 10-Eurocent coin and the glass standard were recorded. The range of detectable elements was thereby successfully extended to light elements like Si and Al.

The results for the steel standard were compromised by the large Kα iron escape peak, which had considerable overlaps with the trace elements of Ti and Mn. All other elements showed errors between 6 and 22 % when fitting was performed in AXIL, and 1 to 20 % when PyMCA was used. Again, these results suggest that it may be advantageous to use PyMCA instead of AXIL for background fitting.

The error margin for the elements of the 10-Eurocent coin was reduced from a maximum relative error of 77 % to values between 1 and 13 % for analysis with AXIL. This standard could not be quantified correctly in PyMCA due to fitting problems.

Quantification of the glass standard (SRM 621) showed particular improvement under the helium environment. Despite the incorrect quantification of Ba, Ti and K, which is owed to overlaps between Ba and Ti and K and the Si sum peak, the errors were lower than for a previous analysis carried out by [39] with the evacuated side-window setup. The previously high error rates between 5 and 92 % could be reduced to an error of 4 to 38 % when measurement was performed with the transmission tube instead of the side-window spectrometer.

Detector efficiency and anode thickness have proven to be critical parameters that should not be underestimated and may be the reason for severe errors in quantification. Furthermore, air or helium paths between the tube and the sample and the sample and the detector should be measured and simulated carefully in order to avoid quantification errors. Sample quality and positioning may also play a role, and even the model itself may have limitations or may be suitable for specific anode parameters only.

18.2 Outlook

Despite the excellent results obtained by means of mathematical spectral correction, the above modifications are limited to tube voltages of approximately 40 kV. As the tube spectrum changes with the tube voltage, the correction process should be repeated for other voltage settings.

In addition, the steel standard and the 10-Eurocent coin could not be measured with the Tracor tube under a helium environment due to time constraints. It would be interesting to see if the conclusions drawn for the bronze samples can be extended to other metals.

Ultimately, the spectrum and thus the measurement results will always depend on the tube, the detector and the geometry of a given setup, which will make it very difficult to apply corrections valid for one specific setup to another tube. Although analogous corrections could be made to improve the quantification of samples for other tube and detector settings, extensive investigations will be needed to determine the root cause of spectral differences between different setups.

References

[1] Alfeld, M. *Was verrät die Röntgenfluoreszenzanalyse?* https://www.weltderphysik.de/gebiet/teilchen/licht/synchrotronstrahlung/roentgenfluoreszenzanalyse/roentgenfluoreszenzanalyse. (last access: 10.11.2019).

[2] Allinger, P. *High Power Polarized vs. Low Power Direct EDXRF.* Master's Thesis: TU Wien, 2015.

[3] Amptek. *Mini-X2 X-Ray Tube Output Spectra.* https://www.amptek.com/products/x-ray-sources/mini-x2-ray-tube#Output-Spectra. (last access: 21.09.2019).

[4] Atominstitut. *Micro-XRF.* https://ati.tuwien.ac.at/forschungsbereiche/strahlenphysik/forschung/ roentgenphysik/employedmethods. (last access: 07.06.2019).

[5] Attix, F. H. *Introduction to Radiological Physics and Radiation Dosimetry.* Weinheim: Wiley-VCH, 1986.

[6] Beckhoff, B., Kanngießer, B, Langhoff, N., Wedell, R. and Wolff, H. (eds.) *Handbook of Practical X-Ray Fluorescence Analysis.* Berlin/Heidelberg: Springer, 2006.

[7] Birkbeck College, University of London. *X-Ray Filters.* http://pd.chem.ucl.ac.uk/pdnn/inst1/filters.htm. (last access: 05.06.2019).

[8] Broll, N. and deChateaubourg, P. "Spectral distribution from end window X-ray tubes". In: *Advances in X-Ray Analysis* 41 (1999), pp. 393–402.

[9] Brouwer, P. *Theory of XRF.* https://www.chem.bg.ac.rs/ grzetic/predavanja/Nedestruktivna%20hemijska%20analiza%20-%20odabrana%20poglavlja/XRF/Literature/PANanalytical%20XRF%20theory.pdf. (last access: 27.10.2019).

[10] Cherry, S. R., Sorenson, J. A. and Phelps, M. E. *Physics in Nuclear Medicine (4th edition).* Philadelphia: Saunders, 2012.

[11] Christofides, S., Dance, D. R., Maidment, A. D., McLean, I. D. and Ng, K.-H. *Diagnostic Radiology Physics. A Handbook for Teachers and Students.* Vienna: IAEA, 2014.

[12] Coderre, J. *Principles of Radiation Interactions (lecture notes).* https://ocw.mit.edu/courses/nuclear-engineering/22-55j-principles-of-radiation-interactions-fall-2004/lecture-notes/ener_depo_photon.pdf. (last access: 10.11.2019).

[13] Demtröder, W. *Experimentalphysik 3 (4th edition).* Berlin/Heidelberg: Springer, 2010.

[14] deVries, J. L. and Vrebos, B. A. R. *Quantification of Infinitely Thick Specimens by XRF Analysis. In: Markovicz, A. A. & Van Grieken, R. E. (eds.), Handbook of X-Ray Spectrometry (2nd edition), 341 ff.* New York/Basel: Marcel Dekker, 2002.

[15] Fischer Technology Inc. *Collimating Polycapillary*. https://www.fischer-technology.com/ en/united-states/products/high-precision-capillary-optics-for-beam-shaping-of-x-rays/x-ray-optics-to-guide-and-shape-x-radiation/parallelises-and-collimates-divergent-radiation/. (last access: 12.06.2019).

[16] Gallhofer, D. and Lottermoser, B. "The Influence of Spectral Interferences on Critical Element Determination with Portable X-Ray Fluorescence (pXRF)". In: *Minerals* 8 (2018), pp. 320–336.

[17] Ghassemi, A. *Fundamentale Parameter der quantitativen Röntgenanalytik - das Röntgenröhrenspektrum*. Doctoral Thesis: TU Wien, 2003.

[18] Goergl, R., Wobrauschek, P., Kregsamer, P., Streli, C. "Measurement of the Spectral Distribution of a Diffraction X-Ray Tube with a Solid-State Detector". In: *X-Ray Spectrometry* 21 (1992).

[19] Goergl, R., Wobrauschek, P., Streli, C., Aiginger, H. and Benedikt, M. "Experimental X-Ray Tube Spectra". In: *Trace and Microprobe Techniques* 14 (1996).

[20] Großmayer, B. *Softwarepaket zur quantitativen Röntgenfluoreszenzanalyse mittels fundamentaler Parameter unter Verwendung von Röntgenoptiken*. Master's Thesis: TU Wien, 2009.

[21] Haschke, M. *Laboratory Micro-X-Ray Fluorescence Spectroscopy: Instrumentation and Applications*. Cham/Heidelberg/New York: Springer, 2014.

[22] He, F. and Van Espen, P. J. "General Approach for Quantitative Energy Dispersive X-ray Fluorescence Analysis Based on Fundamental Parameters". In: *Anal. Chem.* 63 (1991).

[23] Henke, B. L., Gullikson, E.M. and Davis, J. C. "X-ray interactions: photoabsorption, scattering, transmission, and reflection at E=50-30000 eV, Z=1-92." In: *Atomic Data and Nuclear Data Tables* 54(2) (1993).

[24] Henry, D. *Electron-Sample Interactions*. https://serc.carleton.edu/research_education/geochemsheets/electroninteractions.html. (last access: 7.11.2019).

[25] Holub, E. *EDXRF using an Amptec Mini-X tube*. Projektarbeit: TU Wien, 2019.

[26] IAEA Laboratories Seibersdorf. *Quantitative X Ray Analysis System. User's Manual and Guide to X Ray Fluorescence Technique*. https://www-pub.iaea.org/MTCD/publications/PDF/IAEA-CMS-21_CD_web/PDF/CMS_21.pdf. (last access: 18.11.2019).

[27] Jenkins, R. *X-Ray Fluorescence Spectrometry*. New York/Singapore/Toronto: John Wiley and Sons, 1999.

[28] Jenkins, R., Gould, R. W. and Gedcke, D. *Quantitative X-Ray Spectrometry (2nd edition)*. New York/Basel/Hong Kong: Marcel Dekker, 1995.

[29] Jenkins, R., Manne, R., Robin, R. and Senemaud, C. “Nomenclature System for X-Ray Spectroscopy”. In: *Pure and Applied Chemistry* 63(5) (1991), pp. 735–746.

[30] Kolanoski, H. and Wermes, N. *Teilchendetektoren: Grundlagen und Anwendungen.* Springer, 2016.

[31] Krieger, H. *Strahlungsquellen fuer Technik und Medizin (2nd edition).* Wiesbaden: Springer Spektrum, 2013.

[32] Krumeich, F. *Auger electrons.* https://www.microscopy.ethz.ch/auger.htm. (last access: 8.11.2019).

[33] Lépy, M. C. *Detection Efficiency.* http://www.nucleide.org/ICRM_GSWG/Training/Efficiency.pdf. (last access: 15.10.2019).

[34] Li, F. *Monte Carlo Simulation of Energy-Dispersive X-Ray Fluorescence and Applications.* Dissertation: Dissertation, North Carolina State University, 2008.

[35] Lindquvist, M. *Polycapillary X-Ray Optics for Liquid-Metal-Jet X-Ray Tubes.* Uppsala Universitetet, 2017.

[36] Markovicz, A. A. *X-Ray Physics.In: Markovicz, A. A. & Van Grieken, R. E. (eds.), Handbook of X-Ray Spectrometry (2nd edition), 341 ff.* New York/Basel: Marcel Dekker, 2002.

[37] Menesguen, Y., Dulieu, C. and Lepy, M.-C. “Advances in the Measurements of the Mass Attenuation Coefficients”. In: *X-Ray Spectrometry* (2018).

[38] Microscopy Australia. *Characteristic X-rays.* https://myscope.training/legacy/analysis/ eds/xraygeneration/characteristic/. (last access: 15.12.2019).

[39] Necker, P. *Quantitative X-ray Fluorescence Analysis of Samples with Various Matrices Using a Universal Data Evaluation Software.* Master’s Thesis: TU Wien, 2017.

[40] NIST. *X-Ray Mass Attenuation Coefficients.* https://physics.nist.gov/PhysRefData/XrayMassCoef/tab3.html. (last access: 23.05.2019).

[41] Parks, J. E. *The Compton Effect- Compton Scattering and Gamma Ray Spectroscopy.* http://www.phys.utk.edu/labs/modphys/Compton Scattering Experiment.pdf. (last access: 10.11.2019).

[42] Patterson, B. B. and Havrilla, G. J. *Three-Dimensional Elemental Imaging Using a Confocal X-Ray Fluorescence Microscope.* https://www.americanlaboratory.com/913-Technical-Articles/18833-Three-Dimensional-Elemental-Imaging-Using-a-Confocal-X-Ray-Fluorescence-Microscope/. (last access: 13.05.2019).

[43] Percuoco, R. “Plain Radiographic Imaging”. In: *Clinical Imaging* 33 (2014).

[44] Perez, R. D., Sosa, C., Sbarato, V., Leani, J., Sánchez, H. J. “Determination of X-ray excitation spectra in micro X-ray fluorescence”. In: *Spectrochimica Acta Part B* 117 (2016).

[45] Podgorsak, E. B. *Radiation Physics for Medical Physicists (2nd edition).* Berlin/ Heidelberg: Springer, 2010.

[46] Polese, C. *Instruments and Methods for XRF analysis of Materials of Cultural Interest.* Sapienza Università di Roma, 2015.

[47] Povh, B., Rith, K., Scholz, C. and Zetsche, F. (eds.) *Particles and Nuclei: An Introduction to the Physical Concepts (5th edition.* Berlin/Heidelberg: Springer, 2006.

[48] Pushie, M. J., Pickering, I. J., Korbas, M., Hackett, M. J., George, G. N. *Elemental and Chemically Specific X-ray Fluorescence Imaging of Biological Systems.* https:// pubs.acs.org/doi/pdfplus/10.1021/cr4007297. (last access: 14.12.2019).

[49] Rogers, T. H. "Intensity Radiation from Beryllium-Window X-ray Tubes". In: *Radiology* 48.6 (1947), p. 594.

[50] Scholze, F., Beckhoff, B., Kolbe, M., Krumrey, M., Müller, M. and Ulm, G. "Detector Calibration and Measurement of Fundamental Parameters for X-Ray Spectrometry". In: *Microchim Acta* 155 (2006).

[51] Shackley, M. S. (ed.) *X-Ray Fluorescence Spectrometry (XRF) in Geoarchaeology.* New York/Heidelberg/London: Springer, 2011.

[52] Shaltout, A. A. "On X-ray tube spectra, the dependence on the angular and electron energy of X-rays from the targets". In: *The European Physical Journal D* 37 (2007).

[53] Sherman, J. "The theoretical derivation of fluorescent X-ray intensities from mixtures." In: *Spectrochimica Acta* 7 (1955).

[54] Shiraiwa, T. and Fujino, N. "Theoretical calculation of fluorescent X-ray intensities in fluorescent X-ray spectrochemical analysis." In: *Japan Journal of Applied Physics* 5 (1966).

[55] Siemiginowska, A. *Statistics in X-ray Data Analysis. Presentation at the 1st School on Multiwavelegth Astronomy, Paris, 2009.* https://pulsar.sternwarte.uni-erlangen.de/ black-hole/1stschool/coursematerial/statistics_paris2009.pdf. (last access: 30.10.2019).

[56] Sitko, R. and Zawisza, B. *Quantification in X-Ray Fluorescence Spectrometry.* http:// cdn. intechweb.org/pdfs/27342.pdf. (last access: 10.11.2019).

[57] Spectrace Instruments, Inc. *Tracor Xray Spectrace 5000 Technical Manual.* 1989.

[58] Spieler, H. *Semiconductor Detector Systems.* Oxford University Press, 2005.

[59] Sun, T. *Rigid motion correction for head CT imaging.* Dissertation, KU Leuven, 2018.

[60] Thompson, A. C. (ed.) *X-Ray Data Booklet.* https://xdb.lbl.gov/xdb-new.pdf. (last access: 31.12.2019). 2009.

[61] Thomsen, V. "Basic Fundamental Parameters in X-Ray Fluorescence". In: *Spectroscopy* 22(2) (2007).

[62] Toshiyouri, C. *Fluorescence and Auger electron yields as a function of atomic number for K shell vacancies*. https://en.wikipedia.org/wiki/File:Auger_xray_wiki_in_png_format.png. (last access: 06.01.2020).

[63] Van Espen, P. *Evaluation of XRF Spectra. Presentation at the Joint ICTP-IAEA School on Novel Experimental Methodologies for Synchrotron Radiation Applications in Nanoscience and Environmental Monitoring*. http://indico.ictp.it/event/a13226/session/3/contribution/58/material/slides/0.pdf. (last access: 30.10.2019).

[64] Vaughan, D. *An introduction to Energy-Dispersive X-Ray Microanalysis*. https://www.revbase.com/tt/ sl.ashx?z=73090c66dataid=477764&ft=1. (last access: 6.11.2019).

[65] Woll, A. R., Mass, J., Bisulca, C., Huang, R., Bilderback, D. H., Gruner, S., Gao, N. "Development of Confocal X-ray Fluorescence (XRF) Microscopy at the Cornell High Energy Synchrotron Source". In: *Applied Physics A* 83 (2006).

A Standard 621

U. S. Department of Commerce
Malcolm Baldrige
Secretary

National Bureau of Standards
Ernest Ambler, Director

National Bureau of Standards

Certificate

Standard Reference Material 621

Soda-Lime Container Glass

(In cooperation with the American Society for Testing and Materials)

This Standard Reference Material is for use in checking chemical methods of analysis and for calibrating optical emission and x-ray spectrometric methods of analysis.

Constituent	Percent by weight	Uncertainty
SiO_2	71.13	0.03
Na_2O	12.74	0.05
CaO	10.71	0.05
Al_2O_3	2.76	0.04
K_2O	2.01	0.03
MgO	0.27	0.03
SO_3	0.13	0.02
BaO	0.12	0.05
Fe_2O_3	0.040	0.003
As_2O_3	0.030	0.001
TiO_2	0.014	0.003
ZrO_2	0.007	0.001

The certified values are the present best estimates of the "true" values based on the results of a cooperative analytical program. At NBS twelve statistically selected samples of the glass were tested for homogeneity by S.D. Rasberry and L. Zinger using x-ray fluorescence spectrometry. Based on their results the variations among samples are estimated to be less than the uncertainties given above.

The overall direction and coordination of the round-robin analysis leading to certification were performed by Paul Close, Chairman of ASTM Subcommittee C-14.02 on Chemical Analysis of Glass and Glass Products.

The technical and support aspects involved in the preparation, certification, and issuance of this Standard Reference Material were coordinated through the Office of Standard Reference Materials by G.W. Cleek, C.L. Stanley, and R.E. Michaelis.

Washington, D.C. 20234
January 21, 1982
(Revision of certificate
dated 3/13/75.)

George A. Uriano, Chief
Office of Standard Reference Materials

(over)

B Standard 1171

National Institute of Standards & Technology

Certificate of Analysis

Standard Reference Material® 1171

Stainless Steel (Cr 17-Ni 11-Ti 0.3)
(AISI 321)

This Standard Reference Material (SRM) is intended primarily for use in optical emission and X-ray fluorescence spectrometric methods of analysis. A unit of SRM 1171 is an annealed solid disk approximately 31 mm × 19 mm.

Certified Values: Certified values for constituents in SRM 1171 are provided in Table 1. All values are reported as mass fractions [1]. The uncertainty listed with the value is an expanded uncertainty, $U = ku_c$, based on a 95 % confidence level [2] and is calculated according to the method in the ISO/JCGM Guide [3]. A NIST certified value is a value for which NIST has the highest confidence in its accuracy in that all known or suspected sources of bias have been investigated or taken into account [4]. A certified value is the present best estimate of the "true" value based on the results of analyses performed at NIST and collaborating laboratories. Test methods used to determine these elements are identified in the appendix and the accompanying key.

Reference Values: A reference value for cobalt is listed in Table 2. Reference values are non-certified values that are the present best estimates of the true values; however, the values do not meet the NIST criteria for certification and are provided with associated uncertainties that may not include all components of uncertainty [4]. The uncertainty listed with the value is an expanded uncertainty based on a 95 % confidence level [4] and is calculated according to the method in the ISO/JCGM Guide [3].

Information Values: Information values are provided for additional constituents in Table 3. An information value is considered to be a value that will be of interest to the SRM user, but insufficient information is available to assess the uncertainty associated with the value. They are intended to provide additional information on the matrix.

Expiration of Certification: The certification of **SRM 1171** is valid indefinitely, within the measurement uncertainty specified, provided the SRM is handled and stored in accordance with the instructions given in this certificate (see "Instructions for Use"). Periodic recertification of this SRM is not required. The certification is nullified if the SRM is damaged, contaminated, or otherwise modified.

Maintenance of SRM Certification: NIST will monitor this SRM over the period of its certification. If substantive technical changes occur that affect the certification, NIST will notify the purchaser. Registration (see attached sheet or register online) will facilitate notification.

Overall direction and coordination of the technical measurements leading to the certification were performed by O. Menis and J.I. Shultz. Homogeneity testing was performed S.D. Rasberry, J. McKay, and B.F. Scribner of NIST.

Review and revision of value assignments was performed by J.R. Sieber and W.R. Kelly of the NIST Chemical Sciences Division.

Statistical consultation for this SRM was provided by D.D. Leber of the NIST Statistical Engineering Division.

Support aspects involved in the issuance of this SRM were coordinated through the NIST Office of Reference Materials.

Carlos A. Gonzalez, Chief
Chemical Sciences Division

Gaithersburg, MD 20899
Certificate Issue Date: 25 June 2014
Certificate Revision History on Page 3

Robert. L Watters, Jr., Director
Office of Reference Materials

Analyses for certification were performed by the following: NIST: R.K. Bell, T.A. Rush, T.C. Rains, and S.A. Wicks; Armco Steel Corporation, Baltimore, MD: R.L. LeRoy and L.V. Beauchamp; and Carpenter Technology Corporation, Research and Development Center, Reading, PA: J.O. Strauss.

INSTRUCTIONS FOR USE

The test surface is the side opposite to the surface labeled with the SRM number and the diamond-shaped NBS logo. The entire thickness of the unit is certified. Each packaged disk has been prepared by finishing the test surface using a milling machine. The user must determine the correct surface preparation procedure for each analytical technique. The user is cautioned to use care when either resurfacing the disk or performing additional polishing as these processes may contaminate the surface. The material should be stored in its original container in a cool, dry location. This material was tested using both solid disks and chips prepared from the same material. The certified values are considered to be representative of the overall average composition of the material.

PREPARATION AND, ANALYSIS[1]

The material for this standard was prepared at the Duquesne Works, U.S. Steel Corporation, Pittsburgh, PA. A portion from a selected slab was cropped at the top and bottom, and the center longitudinal 1/3 of the remaining section was cut out and discarded. The remaining cores were processed to the final size by hot rolling, annealing, and centerless grinding by Carpenter Technology Corporation, Reading, PA.

Homogeneity testing was performed using X-ray fluorescence spectrometry. Certification analyses were performed using the methods provided in the appendix.

Table 1. Certified Values for SRM 1171 Stainless Steel (Cr 17-Ni 11-Ti 0.3)

Constituent	Mass Fraction (%)	Expanded Uncertainty (Mass Fraction, %)	Coverage Factor, *k*
C	0.067	0.010	12.7
Cr	17.50	0.15	3.2
Cu	0.1205	0.0057	12.7
Mn	1.81	0.16	12.7
Mo	0.167	0.040	12.7
Ni	11.18	0.21	12.7
Si	0.536	0.011	12.7
Ti	0.346	0.057	12.7

Table 2. Reference Values for SRM 1171 Stainless Steel (Cr 17-Ni 11-Ti 0.3)

Constituent	Mass Fraction (%)	Expanded Uncertainty (Mass Fraction, %)	Coverage Factor, *k*
Co	0.097	0.079	12.7

[1] Certain commercial equipment, instruments or materials are identified in this certificate to adequately specify the experimental procedure. Such identification does not imply recommendation or endorsement by the National Institute of Standards and Technology, nor does it imply that the materials or equipment identified are necessarily the best available for the purpose.